REVIEW

Check for updates

Two-dimensional MXenes for electrochemical energy storage applications

Pragati A. Shinde, [ID] † Amar M. Patil,† Suchan Lee,† Euigeol Jung and Seong Chan Jun [ID] *

Since the discovery of $Ti_3C_2T_x$ in early 2011, a newly emerging family of post-graphene two-dimensional transition metal carbides and nitrides (MXenes) has been rigorously investigated due to their high electrical conductivity and various stunning properties. MXenes have attracted significant research interest worldwide and have demonstrated promising potential in energy storage applications owing to their layered structure, superior hydrophilicity, metallic nature, high charge carrier mobility, tunable bandgap, and rich surface chemistry. To completely exploit their potential beyond the existing boundaries, unique functional nanostructures, monolayers, multilayer compounds, nanoparticles, and composites have been prepared through functionalization, hybridization, intercalation, *etc.* MXenes have shown novel and tunable properties, easy processing, and superior electrochemical performance, which make them potential candidates for application in electrochemical energy storage. Herein, we present a forward-looking review of MXene-based materials with their synthesis protocol, fundamental properties, and state-of-the-art electrochemical activity and performance in supercapacitors and rechargeable batteries. Finally, we discuss the challenges that must be addressed for future research, which will deepen the basic understanding of MXenes and their derivatives to promote further advancements in burgeoning energy storage technologies.

1. Introduction

Owing to the depletion of fossil fuels and the environmental problems caused by their utilization, one of the foremost scientific and social responsibilities facing researchers worldwide is to develop sustainable energy resources for upcoming generations. The International Energy Agency reports that worldwide energy demands will increase from 18 TW in 2014 to 24 TW in 2040.[1] This rapid progress in energy utilization along with multiple environmental issues has compelled the development of green and sustainable energy storage and conversion devices to ease the complete dependence on fossil fuels. Energy storage devices perform a core role in flexible wearable gadgets and modern electronic equipment.[2] As representative green and cost-effective electrochemical energy storage devices, supercapacitors (SCs) and rechargeable batteries have received significant interest worldwide for the sustainable development of modern electronics and hybrid electric vehicles.[3–5] High energy density, cyclic durability, and charge/discharge rates of batteries are not always complementary. Alternatively, SCs store charges at the electrode/electrolyte interface through the physical accumulation of ions for electrochemical double-layer capacitors (EDLCs) and through fast and reversible faradaic reactions for pseudocapacitors.[6–8] These mechanisms provide a high charge/discharge rate; however, they unavoidably limit the feasible energy density of SCs. Hybrid nanomaterials obtained with EDLCs and pseudo-capacitive charge storage mechanisms are in high demand for both batteries and SCs.[9,10] Electrode materials, as the heart of energy storage devices, play a vital role in achieving superior electrochemical performance.

From the discovery of graphene and graphene oxide, two-dimensional (2D) materials with thicknesses of a few atomic layers have attracted considerable research attention owing to their unique and multiple fascinating properties, which do not exist in their ordinary bulk form.[11] Currently, a large number of post-graphene 2D materials, including boron nitride, transition metal dichalcogenides (TMDs), transition metal oxides (TMOs), black phosphorous (BP), silicane, and germanene, have been successfully synthesized with significant advancements in their synthesis techniques.[12,13] Among them, a newly emerging popular family of 2D transition metal carbides (TMCs) and transition metal nitrides (TMNs), which are also known as "MXenes," have been developed. MXenes exhibit a structure that combines two or more layers of transition metal (M) atoms crammed into a honeycomb-like 2D lattice; these layers are twinned by carbon or N layers (X) that occupy the adjacent octahedral sites between M layers.[14–16]

Nano-Electro-Mechanical Device Laboratory School of Mechanical Engineering, Yonsei University Seoul, 120-749, South Korea. E-mail: scj@yonsei.ac.kr

† These authors contributed equally to this work as first author.

This journal is © The Royal Society of Chemistry 2022

J. Mater. Chem. A, 2022, **10**, 1105–1149 | **1105**

Generally, MXenes are created by the etching of A layers from the layered ternary carbides/nitrides (MAX) phases, which can be represented as $M_{n+1}AX_n$ (M represents transition metals such as Ti, Mo, Nb, and V; X is carbon or N, and $n = 1, 2, 3$; A is a group IIIA or IVA element).[17–19] The layered hexagonal structures of MAX phases contain $M_{n+1}AX_n$ units and A layers, which are alternately stacked. As the M–A bond in MAX is more chemically active than the M–X bond, A layers can be chemically etched without breaking the M–X bonds, which results in weakly bonded $M_{n+1}X_n$ layers that can be easily detached after ultrasonication.[20] Therefore, the obtained 2D materials, known as MXenes without A layers from the parent MAX phase, possess a 2D nature similar to that of graphene.[21,22] Moreover, during the etching process, the $M_{n+1}X_n$ units are sheltered by surface functional groups. Therefore, the chemical formula of MXenes is represented as $M_{n+1}X_nT_x$ (where T_x indicates the surface functional group –O, –OH, or –F).

MXenes have been widely investigated and exhibit various similarities to graphene. First, graphene and MXene can be prepared using a "top-down" exfoliation method from the parent graphite or a MAX material. This exfoliation facilitates the development of large-scale ultrathin 2D nanomaterials having thicknesses of a single atom or few atomic layers. Second, graphene and MXene materials show high conductivity and high specific surface area, which are useful for several applications in the field of energy storage and conversion.[23,24] Third, graphene and MXene can be modified to tune the morphology, crystalline structure, and surface properties for specific applications.[25,26] Furthermore, with heteroatom doping and surface modifications, the microstructure of graphene and MXene materials can be further modified to achieve superior performance. These similarities provide promising perspectives for MXene-based materials for energy storage applications. The unique properties and various surface chemistries of MXenes exhibit several fascinating thermal, electronic, magnetic, and electrochemical properties. Additionally, solid solutions on both the M and X sides with multiple single (O, Cl, S, F, *etc.*) or mixed (O, OH, or F) surface terminations result in a large family of 2D materials. Moreover, the 2D morphology and layered structures of MXenes and their combination with other materials enable the development of different materials with impressive properties that complement each other. The mechanically strong, environmentally stable, and highly conductive MXenes demonstrate their foremost influence on flexible, wearable, and self-powered electronic devices. The use of MXenes with other 2D materials to form heterostructures and devices with improved electrochemical performance is conceivably the most promising prospect.

The current review provides an overview of the experimental and theoretical studies related to MXenes and their derivatives. A forward-looking review of the synthesis protocols and fundamental properties such as electronic, thermal, optical, and mechanical properties is presented, which highlights the considerable potential of MXenes in energy storage applications, including SCs and rechargeable batteries. We conclude present review with a description of the difficulties to be expected in further investigations in the field of most exciting 2D materials.

2. MXene synthesis approaches

2.1 Synthesis of MXenes by top-down approaches

Since the first discovery of 2D MXenes in 2011, an increasing number of attempts have been made for the development of new methods for MXene synthesis, investigation of novel characteristics, and advanced applications of MXenes.[14] MXenes are often produced by selective etching of certain atomic layers from matching layered precursors such as ternary layered ceramic material (MAX) phases.[27] The composition of the MAX phase varies as the "*n*" value changes from 1 to 4 and the number of "M" layers changes from to 2 to 4, as expressed by the general formula $M_{n+1}AX_n$ (Fig. 1a). Typically, these are divided in two to three types as "M" changes from 2 to 4, which can be represented as 211, 312, 413, respectively.[28] More than 130 distinct compositions exist in the MAX-phase family, with the bulk of them crystallizing in the $P6_3/mmc$ space group.[29] The MAX structure consists of MX_6 octahedra, interconnected with "A" layers. In the subsequent steps, approximately 30 MXenes are generated by etching Al from MAX phases, which are typically easy to handle and store (Fig. 1b).[14,30] The MAX phases show various structures as "M" changes from $M_{1.33}$ to M_4. The synthesized MXenes are in the form of $M_{1.33}XT_X$, M_2XT_X, $M_3X_2T_X$, and $M_4X_3T_X$, depending on the MAX phase. MXenes are synthesized through different methods such as the etching of "A" group using HF, HCl + LiF, HCl + (Na, K, or NH_4F), $ZnCl_2$, NH_4HF_2, H_2O_2 + HF, or through electrochemical etching in HCl, hydrothermal synthesis using NaOH, electrochemical etching using NH_4Cl/tetramethylammonium hydroxide (TMAOH).[31–37] MXenes are most often produced using MAX phases, although certain layered materials, such as 211-structured Mo_2Ga_2C, can also be utilized. Furthermore, several layered solid materials such $(MC)_n(Al, Si)_4C_3$ and $(MC)_nAl_3C_2$ are etched to remove (Al, Si)$_4C_4$ and Al_3C_3 to synthesize $Hf_3C_2T_Z$ and $Zr_3C_2T_Z$ MXenes, respectively.[38,39] Up to 2014, the MAX phases based on the "M" sites, which have a random solid solution such as the 211 phases of $(Ti_XCr_{1-X})_2AlC$[40] and $(Ti_XNb_{1-X})_2AlC$,[41] 311 phases of $(Ti_{1/2}V_{1/2})_3AlC_2$, and 413 phases of $(Cr_{5/8}Ti_{3/8})_4AlC_3$[42] were investigated. Two new chemically ordered quaternary MAX phases of "out-of-plane ordered" (312 and 413) and "in-plane ordered" (211 phases) were investigated in 2014 and 2017, respectively. Some of MAX phases such as $(Mo_{2/3}Sc_{1/3})_3AlC_2$, $(Mo_{2/3}Ti_{1/3})_3AlC_2$, $(Cr_{2/3}Ti_{1/3})_3AlC_2$, and $(Mo_{1/2}Ti_{1/2})_4AlC_3$ represent an "M" elemental layer sandwiched between layers of another "M" element, such as Mo on the outside and Ti or Sc layers in the inner side.[42–45] Similarly, certain quaternary phases of $(V_{2/3}Zr_{1/3})_3AlC_2$, $(Mo_{2/3}Y_{1/3})_2AlC$, and $(W_{2/3}Sc_{1/3})_2AlC$ were discovered recently.[46,47] However, more than hundreds of stoichiometric structures are expected to be synthesized, perhaps making 2D-MXenes the biggest family of 2D materials.

Most MXenes are synthesized by employing concentrated HF treatments or *in situ* HF (HCl and LiCl salt) acid etching procedures to replace the A group with surface functional groups such as –OH, –F, and –O–.[17] However, HF is significantly

1106 | *J. Mater. Chem. A*, 2022, **10**, 1105–1149

This journal is © The Royal Society of Chemistry 2022

Fig. 1 (a) A periodic table illustrating the elements in MAX phases and MXenes, surface terminations, and intercalant cations based on experimental research, (b) schematic representation of synthesis of $Ti_3C_2T_X$ MXene by HF etching and exfoliation by sonication, (c) photographs show the washing process after etching of MAX, in which the photographs of bottom part of plastic tube after 1st washing cycle, after 8th washing cycles, $Ti_3C_2T_X$ and $Ti_3AlC_2/Ti_3C_2T_X$ slurry at the bottom part, (d) SEM image of compact layered Ti_3AlC_2-MAX powder at higher magnification, (e) SEM image of multi-layered 30F $Ti_3C_2T_X$ MXene at higher magnification, (f) SEM image of $Ti_3C_2T_X$ MXene flakes, (g) HRTEM image, (h and i) HRTEM image for bilayer $Ti_3C_2T_X$ and atomic model corresponding to HRTEM image, and (j) XRD patterns of $Ti_3C_2T_X$ and $Ti_3AlC_2/Ti_3C_2T_X$ slurry collected after washing process. (a) Is adapted with permission.[50] Copyright 2021, American Chemical Society. (b, g–i) are adapted with permission.[14] Copyright 2011, Wiley-VCH, (c–f and j) are adapted with permission.[33] Copyright 2017, American Chemical Society.

corrosive and toxic, causing material flaws and necessitating several processes to achieve final MXene sheets. Non-HF etchants (NH_4HF_2, LiF, NaF, KF, NaOH, and tetrabutylammonium hydroxide (TBAOH)) were selected to prevent undesired defects in the MXene sheets. The etching of the Ti_3AlC_2 MAX phase with NH_4HF_2 in various organic solvents showed a typical accordion-
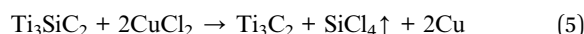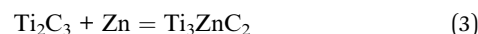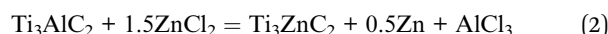
like morphology for the synthesized $Ti_3C_2T_X$ MXene. The intercalation of NH_4^{+}/organic solvent produces a significantly larger d-spacing in the obtained MXene when compared to that obtained using NH_4HF_2 aqueous solution.[35] According to certain research, water is another key factor in the deterioration of $Ti_3C_2T_X$ MXene. Consequently, water-free MXene synthesis techniques can be used to avoid degradation.[48] It is also worth noting that, when MXene exfoliated in propylene carbonate was utilized to make the anode of a Na-ion battery (SIB), the capacity of the battery electrolyte was approximately doubled in comparison to an MXene etched in water. According to Li et al.,[36] by using hydrothermal treatment and NaOH, it is possible to synthesize $Ti_3C_2T_X$ MXene from the Ti_3AlC_2 MAX phase. A layer of Al is attacked by –OH ions, leading to the production of $Al(OH)_4^{-}$, a compound that can be dissolved by an alkali solution, and the Ti atoms are terminated with OH or O. Ma et al.[49] developed Mo_2C and Mo_2N MXenes from metal precursor $MoCl_5$ using the urea glass method. Alhabeb et al.[33] reported the guidelines for the synthesis of MXenes under various etching conditions, and the detailed results are presented (Fig. 1c–f, j). After the etching process, the multiple layers of the obtained $M_{n+1}X_nT_X$ are held together through hydrogen and/or van der Waals bonds (Fig. 1g–i).[14] The in situ generation of HF from a mixture of NaF/LiF and HCl, which is simply called as clay method, was developed by Ghidiu et al.,[17] which generated superior quality MXene sheets than other etching methods. Similarly, the selective etching of the Si elemental layer was first successfully performed from the MAX phase of Ti_3SiC_2.[38] The reaction during etching of the Al process is as shown below.

$$M_{n+1}AlX_n + 3HF \rightarrow M_{n+1}X_n + AlF_3 + 1.5H_2 \quad (1)$$
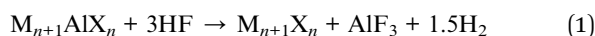
After the etching process of MAX phases, the resulting multilayers of MXenes must be washed with water several times to remove the etching by-products such as AlF_3.[14,33] If the MXene multilayers are synthesized using etchants excluding HCl + LiF, then the multilayers can be exfoliated directly by sonication; however, the total yield is low.[14,33] The resulting MXene sheets are generally bigger in size and have fewer nanometer-sized defects, which is significant for various uses. For applications requiring electrical conductivity, large flake materials with minimal defects are more suitable. A high yield is possible using liquid exfoliation with the intercalation of molecules to obtain colloidal solutions. The interlayer interactions between MXene multilayers can be weakened by the insertion of appropriate molecules that swell in the interlayer space. Certain polar organic molecules, such as dimethyl sulfoxide (DMSO), were used to exfoliate the MXenes of $Ti_3C_2T_X$ and $(Mo_{2/3}Ti_{1/3})_3C_2T_X$.[44,51] However, other than these two MAX phases, DMSO is unsuitable for the exfoliation of MXenes. Some MXenes of $(Mo_{2/3}Ti_{1/3})_3C_2T_Z$, $(Mo_{1/2}Ti_{1/2})_4C_3T_Z$, $Ti_4N_3T_Z$, Mo_2CT_Z, Nb_2CT_X, and Ti_3CNT_Z can be exfoliated by the intercalation of TBAOH.[52–56] Furthermore, the V_2CT_Z MXene can be exfoliated by choline hydroxide, TBAOH, and n-butylamine.[53] However, the etching of MAX phases using the LiF and HCl method itself creates exfoliation of MXenes by intercalation of Li^{+} in the layers

of MXenes, creating larger d-spacing.[33] Kamysbayev et al.[57] synthesized bromine-terminated MXenes of Ti_2CBr_2 and $Ti_3C_2Br_2$ using $CdBr_2$ in its molten state. This study revealed the efficacy of a molten salt-based method in modifying the surface chemistry of MXenes through exchange and elimination processes.[57,58]

Moreover, the Lewis acidic etching method was employed to synthesize MXenes with improved electrochemical performance.[59–61] The direct redox coupling between the cation of the Lewis acid molten salt and "A" elements in the MAX phase provides an effective number of MXenes. A cubic phase of TiC_x ($x \approx 0.5$) was induced from the topotactic transformation of Ti_2AlC using molten salt of LiF at 900 °C for 2 h in air, which included significant amounts of O and F.[62] Li et al. devised a method to synthesize Zn-based MAX phases and Cl-terminated MXenes (Ti_3C_2Cl and Ti_2CCl_2) via a replacement reaction between the MAX phase and the transition metal halides ($ZnCl_2$); Al from the MAX phase was replaced with a transition metal element (Zn) (Ti_3ZnC_2) (reactions 2–4).[63] Recently, Li et al.[59] revealed a new method for synthesizing Ti_3C_2 MXene that relies on the direct reaction between $CuCl_2$-molten-salt cationic species and "A" elements from the Ti_3SiC_2 MAX phase (reactions 5 and 6). The derived MXene demonstrated better electrochemical performance in nonaqueous electrolytes, with greater Li^{+} storage capacity and rate performance. Lu et al.[61] applied scanning transmission electron microscopy (STEM) and first-principles calculations to investigate new terminations that have a large MXene functionalization space, and the Cl terminations were stable up to 750 °C. When compared to the chloride-based molten salt etching method, Urbankowski et al.[55] utilized molten fluoride salts to selectively etch Al from a Ti_4AlN_3 powder precursor at temperatures of 550 °C in the presence of an inert gas to create 2D $Ti_4N_3T_X$ MXene. A variety of MXenes were synthesized from corresponding MAX phases, including Ti_3ZnC_2, Ti_3ZnC_2, Ti_3AlCN, Ti_3AlC_2, Ta_2AlC, and Ti_3ZnC_2.[63] Li et al. conducted a comprehensive research using Lewis acid molten salts such as $FeCl_2$, AgCl, $NiCl_2$, and $CuCl_2$. The findings show that the redox potential is a critical element in determining the viability of a replacement process. Thus, by employing the correct Lewis acid molten salts, additional A-site elements in MAX phases may also be eliminated by utilizing this molten salt etch technique.[63,64]

$$Ti_3AlC_2 + 1.5ZnCl_2 = Ti_3ZnC_2 + 0.5Zn + AlCl_3 \quad (2)$$

$$Ti_2C_3 + Zn = Ti_3ZnC_2 \quad (3)$$

$$Ti_3ZnC_2 + ZnCl_2 = Ti_3C_2Cl_2 + 2Zn \quad (4)$$

$$Ti_3SiC_2 + 2CuCl_2 \rightarrow Ti_3C_2 + SiCl_4\uparrow + 2Cu \quad (5)$$

$$Ti_3C_2 + CuCl_2 \rightarrow Ti_3C_2Cl_2 + Cu \quad (6)$$

However, the process of etching in the MAX phase using molten salts still shows significant limitations. Fluoride and other contaminants are difficult to eliminate completely. Most molten salt etching methods rely on atmospheric protection,

1108 | *J. Mater. Chem. A*, 2022, **10**, 1105–1149

This journal is © The Royal Society of Chemistry 2022

temperature control, and temperature monitoring. Most production techniques rely on water as the primary solvent, and fluoride-based chemicals such as etchants produce poisonous gases and numerous –OH groups on MXene surfaces. However, the etching process using different agents directly affects the surface morphology, structural defects, and surface groups of MXenes.

2.2 Synthesis of MXenes through bottom-up approaches

MXenes are also synthesized *via* bottom-up techniques such as plasma-enhanced pulsed laser deposition (PEPLD), chemical vapor deposition (CVD), and template methods.[65–67] When compared to the MXenes produced by the top-down methods, the benefit of these techniques, especially the CVD process is that it gives high crystallinity. These methods can synthesize stoichiometric TMCs and TMNs such as WC, TaC, TaN, and MoN; however, selective etching techniques are unable to synthesize these phases.[68–70] Using the CVD technique, Xu *et al.*[71] first reported the development of high-area 2D ultrathin Mo_2C MXene superconducting crystals on a Cu/Mo bilayer substrate. The crystals had a thickness of a few nanometers, a size of over 100 µm, and were stable under ambient conditions. It also showed 2D superconducting transition characteristics and significant anisotropy in the direction of the magnetic
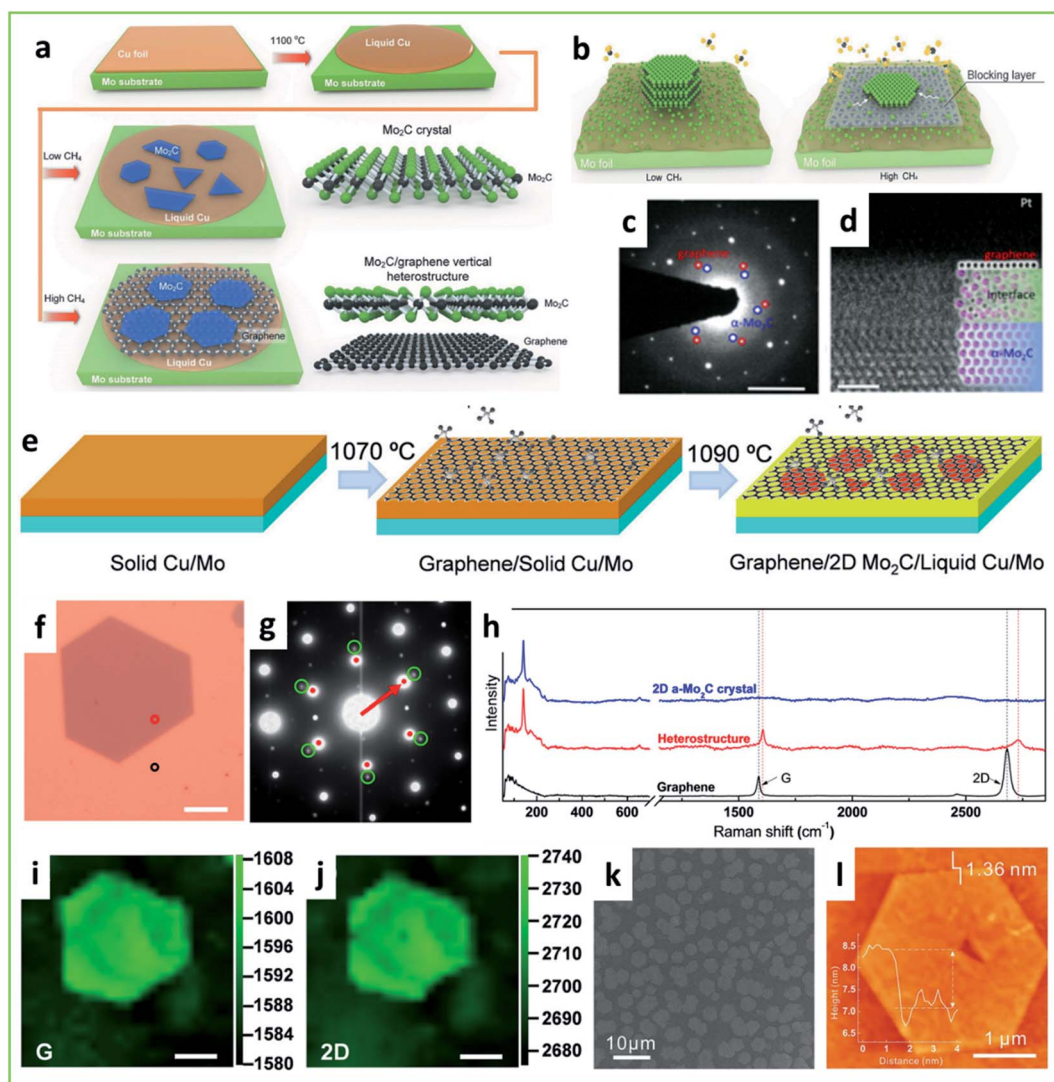

Fig. 2 (a) Schematic illustration of CVD growth of Mo_2C crystals; (b) schematic for growth of Mo_2C and Mo_2C/graphene structures under low and high CH_4 gas flow concentrations; (c) SAED pattern of hexagonal α-Mo_2C/graphene heterostructure (scale bar is 1 µm), (d) HAAF–STEM images of interfaces; (e) schematic for direct growth of α-Mo_2C/graphene heterostructure through two-step CVD; (f) optical image of α-Mo_2C/ graphene heterostructure showing compressed graphene; (g) SAED pattern of 2D α-Mo_2C region; (h) Raman spectra of pure α-Mo_2C, graphene and α-Mo_2C/graphene heterostructure for the images shown in (f) (red circle indicates heterostructure); (i and j) G and 2D peak position mappings of a α-Mo_2C/graphene heterostructure grown using CVD method (scale bar is 5 µm); (k) SEM image of WC single crystal embedded in graphene; and (l) AFM image of WC single crystal and thickness analysis. (a and b) Are adapted with permission.[74] Copyright 2017, Wiley–VCH, (c and d) is adapted with permission.[78] Copyright 2018, American Physical Society, (e–j) are adapted with permission.[76] Copyright 2017, American Chemical Society, and (k and l) adapted with permission.[68] Copyright 2017, Elsevier.

This journal is © The Royal Society of Chemistry 2022

J. Mater. Chem. A, 2022, **10**, 1105–1149 | **1109**

field; however, the superconducting property was solely dependent on the thickness of the Mo_2C crystals. Nevertheless, the thickness of these crystals was determined entirely by the rate of CH_4 flow; for ultrathin Mo_2C, a low CH_4 concentration was essential. The 2D α-Mo_2C crystal has an orthorhombic structure; moreover, it was composed of hexagonal-closed-packed Mo atom and interstitial carbon atoms at half the octahedra.[72] These crystals were in different shapes and sizes, predominantly dodecagons, nonagons, octagons, hexagons, rectangles, and triangles with lateral sizes of ∼10 μm and thicknesses of 3–20 nm. The octagonal ultrathin crystal of α-Mo_2C had a size of ∼100 μm and a thickness of 10 nm. The optical images of hexagonal α-Mo_2C crystals showed thicknesses of 6.7, 87.2, and 11.2 nm; after they were transferred on to a SiO_2/Si substrate, different colors were observed based on the thickness. The lattice parameter "a" was calculated from the convergent-beam electron diffraction pattern and it was measured as 4.77 Å based on $r^2 + (\lambda^{-1} - a^{-1})^2 = \lambda^{-2}$, where λ and r are the wavelength and radius of the first-order Laue ring with values of 0.00251 nm and 40.83 nm^{-1}, respectively.[73] The Mo atoms were closely packed with hexagonal arrangement in the α-Mo_2C crystal structure and it was verified through atomic-level high-angle annular dark field (HAADF)-STEM and bright-field (BF)-STEM analyses.

Previous studies have reported the direct development of MXene/graphene heterostructures.[66,68,74–78] Two distinct CVD techniques have been described for the production of MXene/graphene heterostructures: one- and two-step methods.[66,74] To synthesize heterostructures, Deng et al.[66] used a one-step CVD method in which Mo_2C/graphene was deposited in a horizontal quartz tube with hydrogen and CH_4 to generate carbon on a Cu/Mo substrate through CH_4 decomposition (Fig. 2a). According to Geng et al.,[74] a greater concentration of CH_4 gas flow rate promotes the production of graphene layers. Surface-segregated Mo could scavenge the carbon surface at lower concentrations of CH_4, resulting in the formation of Mo_2C. The Mo_2C thickness was substantially reduced at higher concentrations of CH_4 because the graphene layers acted as a blocking layer (Fig. 2b). Another research also reported graphene/Mo_2C hetero-structures (Fig. 2c and d).[66,74] This structure demonstrates a translational staking scheme, with transition defects created mostly by strained channels in the nanometer range, indicating certain limits in the structure.

Other researchers have described two-step CVD methods for graphene/Mo_2C heterostructures, in which a Mo layer is placed beneath the graphene. At a furnace temperature of 1070 °C, a Cu/Mo substrate was first coated with graphene layers in hydrogen/Ar atmosphere, followed by the insertion of CH_4 gas, which aided in the deposition of the heterostructure. In the second stage, the graphene-deposited Cu/Mo was heated above the melting point of Cu (1090 °C) while maintaining other deposition conditions to develop α-Mo_2C crystals below the graphene layer on the surface of the liquid Cu/Mo substrate (Fig. 2e–h).[76] Conversely, the CVD technique was used by Zeng et al.[68] to synthesize an in-plane 2D graphene/TMC (WC/graphene) heterostructure. To ensure the co-segregation of carbon and W atoms, Ga was used because it is a metal with

a low melting point. It was determined that Ga–W was implanted with a single crystal of WC embedded in graphene (Fig. 2k and l). Scanning electron microscopy (SEM) measurements show that the thickness of the single-crystal water-cooled crystal is 1.4 nm; atomic force microscopy (AFM) measurements indicate a measurement of 1.36 nm. According to the aforementioned findings, the two-step CVD technique produces 2D heterostructures of TMC/graphene with fewer flaws than a one-step CVD process.

Previous studies used magnetron sputtering to synthesize TMCs.[35,79–83] By employing DC magnetron sputtering in an Ar environment at 4.8 mbar, Halim et al.[35] could deposit Ti_3AlC_2 thin films using three metal targets, including Ti (75 nm), Al (50 nm), and carbon (75 nm). However, Ti_3C_2 films were produced by the successful etching of Ti_3AlC_2 with 50% concentrated HF and 1 M NH_4HF_2. With DC magnetron sputtering, they first created 15–60 nm thick Ti_3AlC_2 films on sapphire (0001) substrates, and then chemically etched the Al with either HF or NH_4HF_2. A Sc-based MXene was produced by Chen et al.[79] by utilizing dual-target magnetron sputtering with a base pressure of 6×10^{-4} mTorr. However, after deposition once a sample is placed in open air, the –O– groups interact on the surface to form –O– terminated MXenes, which exhibit Sc_2C, Sc_2Co_x, and scandium oxide peaks. Liu et al.[80] developed (Mo_2C)/fluorine mica saturable absorber system using magnetron sputtering under 6.8×10^{-4} Pa to maintain the purity of Mo_2C. Following this work, Li et al.[81] prepared a microfiber-based few-layer Nb_2CNb_2C saturable absorber (thickness of ∼10 nm for 15 layers). They developed microfibers using flame brush technology, which had a diameter of 18.03 μm, on which Nb_2CNb_2C was consistently attached on the cone region of the microfiber. Wang et al.[82] used a radio frequency magnetron sputtering technique for the deposition of Mo_2C thin films on a silver mirror substrate.

Owing to their higher yields, template methods are preferred for the synthesis of MXenes when compared to other CVD methods.[67,70,84] In template methods, the TMCs/TMNs are synthesized by carbonization or nitridation of the used template of TMOs. All the properties of the synthesized MXenes are strictly dependent on the TMOs used. Joshi et al.[70] synthesized large-area vertically oriented 2D δ-MoN using a MoO_3 template, which was synthesized by the CVD method using a hot filament (Fig. 3). Xiao et al.[67] also used the same template (hexagonal oxides) to synthesize 2D MoN by heating in NH_3 and predicted the synthesis of 2D W_2N and V_2N. They developed a salt-templated high-yield strategy for synthesizing 2D MXenes. Furthermore, Jia et al.[84] used MoO_2 nanosheets as a template and dicyandiamide as a carbon and N source to synthesize 2D N-doped Mo_2C. The PEPLD method combines the advantages of both plasma-enhanced CVD and pulsed laser deposition (PLD) techniques into a single approach. Zhang et al.[65] reported the deposition of single-crystalline Mo_2C ultrathin super-conducting films by the PEPLD method. The plasma was generated by a modified PLD system with a high-voltage electrode at the inlet of CH_4, which ionized the gas (DC voltage of 500 V was applied). The deposited film had a smooth wide-area surface with a roughness of 0.3 nm, and the thickness profiles
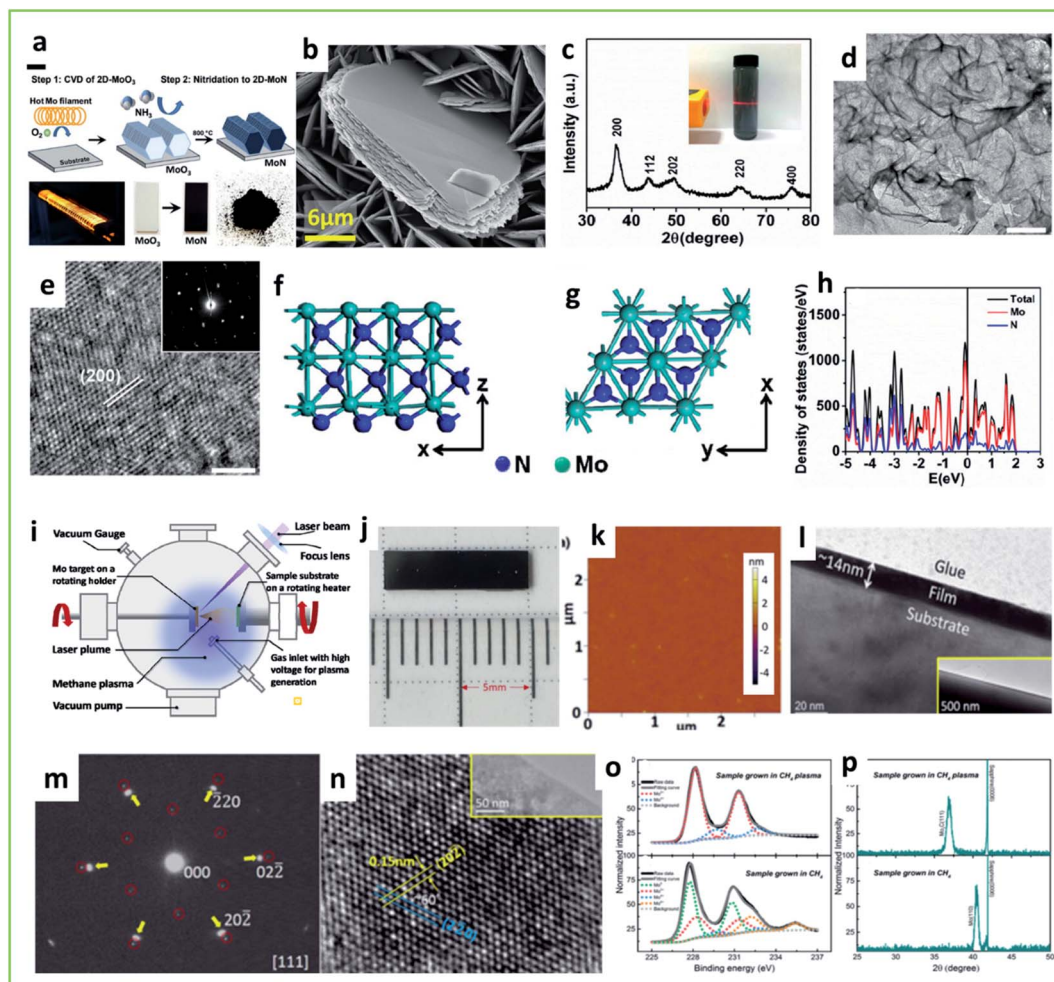
1110 | *J. Mater. Chem. A*, 2022, **10**, 1105–1149

This journal is © The Royal Society of Chemistry 2022

Fig. 3 Synthesis of 2D MoN: (a) schematic illustration of two-step method; (b) SEM image of δ-MoN on fluorine-doped tin oxide; (c) XRD pattern of MoN powder and inset showing Tyndall effect of the colloidal solution of MoN; (d) low-magnification transmission electron microscopy (TEM) images of MoN nanosheets; (e) HRTEM image of 2D MoN indicating single-crystalline hexagonal structure, inset shows SAED pattern of hexagonal structure of MoN; (f and g) side and top views of the atomic structure of 2D MoN structure; (h) density of states (DOS) model of 2D MoN (bandgaps are absent in the plot, indicating the metallic characteristics of MoN); (i) schematic figure for plasma-enhanced pulsed laser deposition system; (j) dimensions of the Mo_2C film grown on sapphire; (k) AFM image of large-area Mo_2C thin film grown on sapphire substrate; (l) cross-sectional TEM image; (m) SAED pattern of overlapped area includes substrate as well as grown Mo_2C thin film (yellow arrows indicate the film and red circles indicate the substrate); (n) HRTEM image of Mo_2C (inset shows low-magnified TEM image); (o and p) X-ray photoelectron spectroscopy and XRD analysis of Mo_2C samples. (a and b) Are adapted with permission.[70] Copyright 2017, American chemical Society. (c–h) Are adapted with permission.[67] Copyright 2017, American Chemical Society. (i–p) Are adapted with permission.[65] Copyright 2017, American Physical Society.

of the substrate and deposited film were examined using transmission electron microscopy (TEM), revealing a thickness of ∼14 nm. Growth in CH_4 plasma exhibited Mo^{2+} states with Mo_2C, although some amount of Mo^{4+} also existed, which reveals that there are certain defects in Mo_2C.[65,85]

Importantly, the size, shape, and thickness of the crystals could be adjusted by altering the experimental deposition conditions, with the nucleation density and lateral size increasing with increasing temperature and time, respectively. Although numerous methods for fabricating various types of MXenes have been discovered, the investigated approaches still exhibit significant drawbacks, such as increased pollution, higher costs, poorer yields, high impurity levels, hazardous ingredients, and poor stability. Thus, high-quality MXenes must

be synthesized in ways that are both cost effective and scalable. Environmentally friendly etchants and cheap raw materials should be prioritized to achieve these aims. The fabrication time and yield should also be considered; consequently, the focus should be on quick and easy methods for obtaining high yields. Only a few reports are available on the energy storage applications of MXenes, which are generally prepared using bottom-up methods. This may be owing to the lack of surface terminations and the compact 2D unexfoliated stacking structure of the MXenes. According to Joshi et al.,[70] MoN is synthesized through hot-filament vapor deposition of 2D nanosheets of MoO_3 and then transformed to δ-MoN. The resulting 2D layers of δ-MoN have a steady battery capacity of 320 mA h g^{-1} for Li^+ storage, with a cycle life of more than 200 cycles without

deterioration or structural alteration. Xiao et al.[67] used 2D MoN in SC applications and reported a volumetric capacitance of 928 F cm^3 in a H_2SO_4 electrolyte. The hydrophilic restacked 2D MoN sheet exhibited an outstanding rate performance.

It is important to understand the advantages and disadvantages of both methods for MXene synthesis, i.e., the top-down and bottom-up methods. Each of the different methods for MXene synthesis exhibit certain advantages and limitations, as discussed subsequently.

HF etching. This technique is considerably efficient and suitable for the synthesis of a wide range of MXene compounds. This technique also allows for simultaneous intercalation during etching. However, HF is hazardous in nature; it creates –F-terminated MXenes, which have a detrimental impact on application performance; moreover, it necessitates additional cleaning processes to eliminate in situ generated HF.[86–88]

Alkali etching. It is feasible to remove the –F terminals from MXenes, and the method is safe owing to the absence of fluorine. However, the mechanism of the organic base (TMAOH) reaction remains unclear. When using inorganic bases, harsh reaction conditions are required.[58,89]

Electrochemical etching. To a certain extent, this technique has control over the surface terminations, and it is safer owing to fluorine-free synthesis. However, electrochemical processes require an expensive experimental setup. Limiting the production of by-products during the reaction necessitates precise control over the applied bias.[90]

Molten salt etching. Lewis acidic salts are efficient in the production of MXenes from MAX phases, including Zn, Ga, and Si. However, it requires harsh experimental conditions, and the products will be –F terminated.[63]

CVD. This method produces ultrathin, high-quality MXenes while allowing morphological control. However, this is a time-consuming and low-yield procedure.[73]

PEPLD. It is feasible to control the crystal structure using this process; however, the procedure is energy intensive and the working mechanism is unclear.[65]

Template-assisted method. Controlling surface terminations is feasible using this method. However, the template for this procedure is limited, and it is an energy-intensive operation.[84]

3.   Properties of MXenes

MXenes can be distinguished from other 2D materials, such as graphene, owing to their unique properties. Their inherent structural features and excellent performance in different applications may be tuned through their composition, surface functionalization, morphology, and crystal structure. $Ti_3C_2T_x$ MXene shows superior electrical conductivity owing to its metal-like features and the three layers of metal (Ti) atoms, which are alternately embedded between carbon layers.
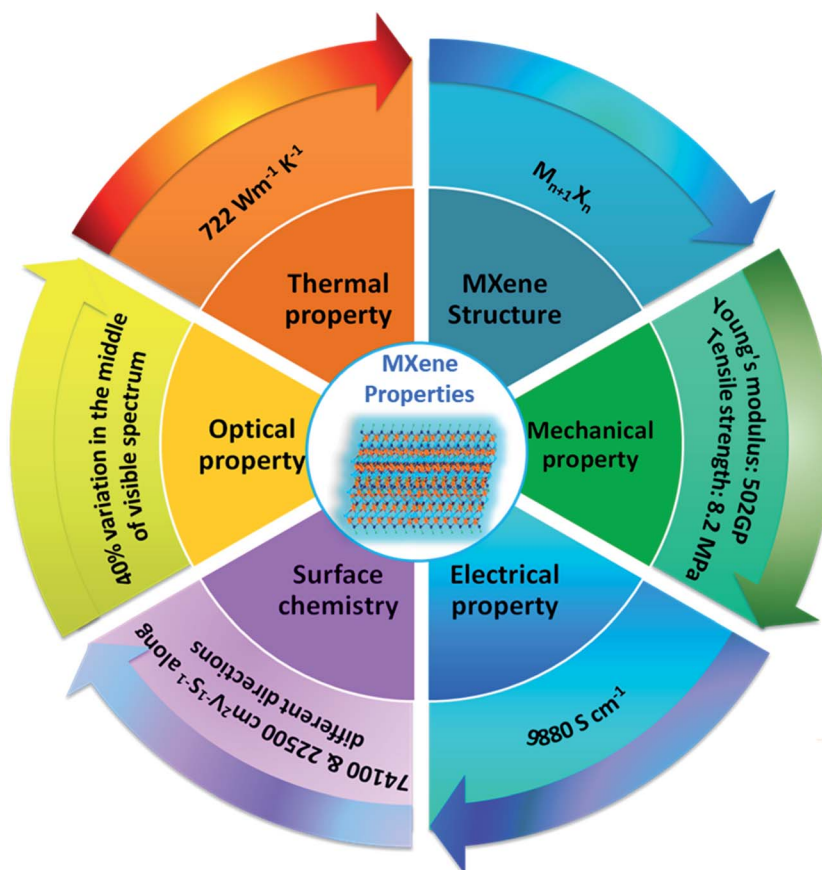

Fig. 4   Schematic diagram of the properties of MXenes.

Theoretical and computational investigations have demonstrated that the number of metal atomic layers affects the physical, chemical, electrical, and mechanical characteristics of MXenes. MXenes have a variety of basic characteristics, which is explored in this section. A diagram illustrating the characteristics of MXenes that are discussed in this study is shown in Fig. 4.

3.1 Surface chemistries

Density functional theory (DFT) of MXenes demonstrates that, MXenes are fully terminated with functional groups, and a greater negative energy indicates a strong connection between surface termination groups and transition metals.[91] The MXenes synthesized by etching the MAX phases in aqueous fluoride-containing acids offer negative terminal hydrophilic functional groups such as −OH, −F, and −O−. Certain reports also confirmed that the surface terminal groups of −Cl and −S demonstrated a large energy.[92] Yang et al.[37] reported the fluoride-free synthesis of Ti_3C_2 through the anodic corrosion of Ti_3AlC_2 in a binary aqueous electrolyte. There are three

possibilities for functional group attachments on transition metal: (i) on top of the transition metals, (ii) between the hollow sites in the top metal, and (iii) in the hollow sites in the stacked layers of X atoms.[93] The bond lengths of Ti−H, Ti−O, and Ti−F were determined to be 0.97, 1.9, and 2.1 Å, respectively; however, the largest adsorption energy of 7.7 eV was observed for the −O− termination, followed by the −F, −OH, −Cl, and −H terminations.[94,95] Although excessive efforts were expended for different synthesis processes and various theoretical calculations were used to synthesize MXenes without terminations, it is difficult to synthesize them without terminations.[95] Some techniques such as X-ray photoelectron spectroscopy, nuclear magnetic resonance (NMR) spectroscopy, Raman spectroscopy, surface acoustic probing, and neutron scattering were implemented to focus on the surface terminations of MXenes.[96–98]

Surface terminations are exhibited in three possible ways: single bonding with one metal atom, symmetrical dual bonding with two metal atoms, and mirror-like symmetrical boding with the central metal layer. Based on the simulation results of high-resolution STEM and HRTEM images, Wang et al.[99] concluded that the −O− terminations were attached to the top sites of the

Fig. 5 (a) Typical cases of stacked $Ti_3C_2T_2$ or V_2CT_2 multilayers with mixed terminations and an AB-stacking arrangement, (b) atomic-resolution high-angle annular dark-field (HAADF) image of $Ti_3C_2Br_2$, and (c) energy-dispersive X-ray elemental analysis (line scan) of $Ti_3C_2Br_2$ MXene sheets. (a) Is adapted with permission.[88] Copyright 2018, Royal Society of Chemistry. (b and c) Adapted with permission.[104] Copyright 2020, American Association for the Advancement of Science (AAAS).

MXenes such as $M_2'M''C_2$ (where M' is Mo, W and M'' is Ti, Zr, Hf) showed topological insulator-like properties.[107] To determine the bandgap responses of the monolayer of Sc_2CO_2 in the electric field (E-field), the band structures were tested in an E-field (Fig. 6b–d). These results show a change in the indirect bandgap energy of 1.830 eV under negative and positive E-fields.[108] Similarly, the electronic conductivity of MXenes changes with defects. MXenes can also be classified into metallic, semi-metallic, and semiconducting forms depending on their electrical conductivity.[109] The electrochemical energy conversion and storage characteristics of MXenes are altered as their electrical conductivity varies with surface terminations. Electrical conductivity is critical for MXene energy storage applications such as SCs and batteries.[87] The most researched $Ti_3C_2T_X$ MXene has a greater electrical conductivity than other 2D metal hydroxides and sulfides; moreover, electrical conductivity is predominantly influenced by surface morphology and surface terminations. For example, delaminated $Ti_3C_2T_x$ flakes with certain defects have a conductivity of 9880 S cm^{-1}, whereas graphene has a conductivity of 6000 S cm^{-1} and extremely defective HF-treated $Ti_3C_2T_x$ powders have a conductivity of 1000 S cm^{-1}.[110] Currently, the electronic properties of Ti_2CT_X, $Ti_3C_2T_X$, $TiNbCT_X$, Ti_3CNT_X, Mo_2CT_X, $Mo_2TiC_2T_X$, $Ta_4C_3T_X$, and $Mo_2Ti_2C_3T_X$ have been investigated.[31,35,54,56,111] Based on the optimized crystal structures, $Ti_3C_2(OH)_2$ MXene was investigated by considering the valence electron density. Xu et al.[73] reported the superconducting characteristics of ultrathin α-Mo_2C crystals. This work reported the temperature-dependent resistance of 7.5 nm thick α-Mo_2C sheets in different magnetic fields along with an excitation current of 1 μA. The zero-field resistance begins to decline around 3.3 K and drops to zero at 2.76 K, indicating the commencement of superconductivity, according to this study. The existence of interlayer decoupled electronic structure in few-layer and bulk Sc_2CCl_2 investigated by varying band gaps of 0.796–0.84 eV (PBE level)/1.63–1.672 eV (HSE06) (Fig. 6e).[112] Furthermore, Jeon et al.[113] reported the carburization of MoS_2 forms an automatically the heterojunction of Mo_2C/MoS_2 and its proved that the lateral contact shows lower contact resistance compared with the vertical one (Ti/MoS_2) (Fig. 6f).

3.3 Optical properties

The nonlinear (nonlinear refractive index, saturable absorption) as well as linear optical properties of MXenes are predominantly reliant on the electronic properties, including energy bandgap, direct and indirect bandgaps, and certain dielectric (ε) or refractive index (η) factors. The optical properties of the medium can be expressed using the dielectric function, i.e., $\varepsilon(\omega) = \varepsilon_1(\omega) + i\, \varepsilon_2(\omega)$, where ω is optical frequency and ε_1 and ε_2 are the real and imaginary parts, respectively. Commonly, the imaginary part is calculated by summation along with empty states by referring to the following equations.[114]

$$\varepsilon_2(\omega) = \frac{4\Pi^2 e^2}{\Omega m^2 \omega^2} \sum_{knn'\sigma} \left\langle kn\sigma | pi | kn'\sigma \right\rangle$$

$$\times \left\langle kn'\sigma | pi | kn\sigma \right\rangle kkn \left(1 - f_{kn'} \right) \delta\left(ekn' - ekn - h^-\omega \right) \quad (7)$$

Fig. 7 (a) Imaginary parts of dielectric constants of Ti_2CO_2, $ZrCO_2$ and Hf_2CO_2 (a–c) optical absorbance spectra for few-layers and for bulk, and (b) Sc_2CCl_2 for light in the Z direction and polarization in the in-plane direction, (a) is adapted with permission.[116] Copyright 2016, Royal Society of Chemistry, and (b) is adapted with permission.[112] Copyright 2018, American Chemical Society.
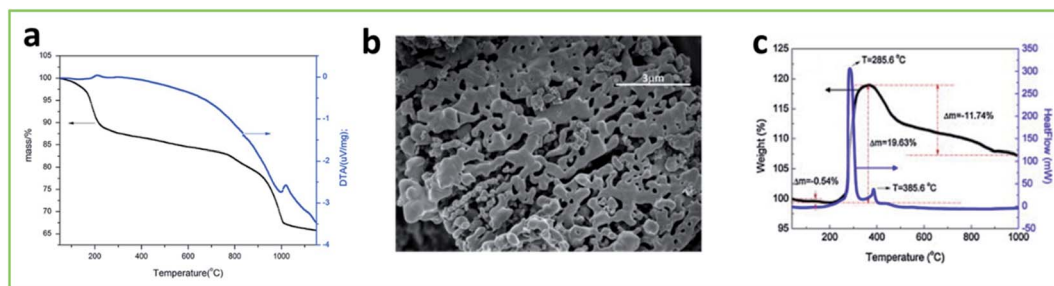
This journal is © The Royal Society of Chemistry 2022

J. Mater. Chem. A, 2022, 10, 1105–1149 | 1115

Fig. 8 (a) TG–DTA curves of Ti_3C_2 (room temperature to 1200 °C in Ar atmosphere), (b) SEM image of $Ti_3C_2T =$ after thermal treatment at 1000 °C in oxygen atmosphere, and (c) TG and DSC curves of MXene in oxygen atmosphere. (a) Is adapted with permission.[124] Copyright 2016, Elsevier, (b and c) are adapted with permission.[125] Copyright 2015, Elsevier.

here, e, Ω, m, f_{kn}, and $\langle kn\sigma \rangle$ are the electron charge, crystal volume, mass, Fermi distribution, and crystal wave function, respectively. The real part of the function can be calculated using the imaginary part by applying Kramers–Kronig transformation.[115] Then, based on the dielectric function, the absorption/gain coefficient, reflectivity, and refractivity can be predicted using standard optical relationships. Lashgari *et al.*[114] reported the optical properties of pristine Ti_2C, Ti_3C_2, Ti_2N, and T_3N_2 using random-phase approximation. As the above-mentioned materials show metallic properties, they do not show the optical bandgap for the imaginary part of the dielectric function. It was reported that the surface termination of –O– and pristine MXenes show higher absorption coefficients than the –F and –OH terminations (Fig. 7a). These changes in the optical properties with changes in the terminations of the MXenes perform an important role in tuning the optical properties with terminations. The –O–functionalized MXenes of Ti_2CO_2, Zr_2CO_2, and Hf_2CO_2 showed visible-light absorption with a large area of $\varepsilon_2(\omega)$ curves. The absorption coefficients of Ti_2CO_2 were higher than those of Zr_2CO_2 and $HfCO_2$.[116] Satheeshkumar *et al.*[117] reported the absorption properties of Ag, Au, and Pd@MXene nanosheets (Fig. 8c). The colloids of MXenes with Ag, Au, and Pd exhibit high absorption in the ultraviolet region (225–325 nm); these absorption properties correspond to the bandgap energy of the oxidized MXenes. Zhou *et al.*[112] analyzed the absorbance spectra of Sc_2CCl using GW + PRA/BSE to determine the light absorbance and quasi-particle bandgap (Fig. 7b). The measured absorbed photon flux values of 7.80, 4.51, and 1.32 mA cm^{-2} for 3, 2, and 1L, respectively, signify the light-harvesting capacity of the material.

3.4 Mechanical properties

Because of their composition, surface functional groups, and number of atomic layers, MXenes have a high Young's modulus of 400–1000 GPa, which is significantly higher than that of their conventional MAX phases. MXenes with surface terminations are mechanically more flexible than pristine MXenes. Lipatov *et al.*[118] investigated the elastic properties of 2D $Ti_3C_2T_X$ MXene monolayers and bilayers accompanied by the tip of an atomic force microscope to track the force–displacement curves. The Young's modulus of a monolayer of $Ti_3C_2T_X$ was observed to be

0.33 TPa.[118] The calculated value of the Young's modulus is considerably near the expected value of the intrinsic in-plane value for a freestanding $Ti_3C_2T_X$ monolayer. Because of the shrinkage and stretching of Ti–C bonds, Ti_3C_2 could maintain strains of 18 and 17% under uniaxial tension, while it showed 9.5% strain under biaxial tension along the *x*- and *y*-axes, respectively.[119] With surface terminations, these values become 28, 26.5, and 20%, respectively, owing to strong covalent bonds. In conclusion, surface terminations are the primary factors that alter the elastic stiffness of $Ti_3C_2T_x$ nanosheets. The mechanical parameters of $Ti_3C_2T_X$ can be improved by using polymers such as chitosan and polyethylene. With the introduction of chitosan, the tensile strength of samples can be expanded up to 8.2–43.5 MPa.[120] Ling *et al.*[121] reported that $Ti_3C_2T_X$/polyvinyl alcohol (PVA) composite demonstrated good electric conductivity and mechanical properties. The delaminated monolayer MXene possesses good mechanical flexibility.[122] Measuring the Young's modulus of vacuum-filtrated delaminated MXene solution is relatively simple; however, it is difficult to measure the Young's modulus for mono/bilayers. Recently, Xu *et al.*[123] investigated the tensile and electrochemical performance of MXene/carbon nanotube (CNT) films. The MXene film showed the lowest elongation and strength before an increase in the CNT content, with a continual increase in strength and a drop in elongation following an initial increase with the increase in CNT. They reported approximately 19–51.4 MPa tensile strength for MXene and MXene/CNT, with an elongation of 0.24–0.73%. They observed that the sample with 40.9 MPa strength and 0.73% elongation had better electrochemical performance, with a specific capacitance of 423.4 F g^{-1} and charge transfer resistance of 0.091 Ω.

3.5 Thermal properties

The thermal stabilities of the solution and thin-film MXenes are important factors for the longer lifetime of MXenes. It was observed that the thermal stability of the MXenes strictly depends on the chemical composition, surface terminations, and surrounding conditions.[119] However, Wang *et al.*[124] reported that $Ti_3C_2T_X$ MXenes are thermally stable up to 500 °C, whereas Ti_3C_2 hexagonal crystals are stable at 800 °C under Ar atmosphere. The thermogravimetry/differential thermal analysis curves of 2D Ti_3C_2 nanosheets from room temperature to

1200 °C in an Ar atmosphere are shown in Fig. 8a. Weight loss was observed in all three stages. The weight loss observed in the third stage at temperatures ranging from 800 to 1200 °C was due to the removal of surface terminations such as –F, –O–. However, in an O atmosphere, the $Ti_3C_2T_X$ MXenes oxidize to form anatase TiO_2 at 200 °C, while they are completely oxidized at 1000 °C to form rutile TiO_2 (Fig. 8b and c).[125] Furthermore, the thermal properties of the MXenes are dependent on the lateral size of the nanosheets. The thermal stability of the Hf_2CO_2 is 86.25 W m^{-1} K^{-1} for 5 μm flakes, whereas it is 131.2 W m^{-1} K^{-1} for 100 μm.[110,126] Kong et al.[127] investigated the improvement in the electrochemical performance of Ti_3C_2 MXene for Li-ion batteries (LIBs) through the vacuum calcination. The surface Ti_3C_2 MXene was stable up to 429.9 °C, whereas rutile TiO_2 is the oxidation product at 1200 °C. They investigated Ti_3C_2 MXene with a higher capacity of 12.4 mA h g^{-1} at 1C and superior rate performance after vacuum calcination at 400 °C. However, the dense microstructure of the TiC_x formed after calcination at 1000 °C showed the worst electrochemical performance.

# 4 State-of-the-art achievements of MXenes in electrochemical energy storage

Globally, the regular consumption of fossil fuels has resulted in greenhouse effects and climate change. Thus, countries over worldwide are focusing on the progression of sustainable energy storage to ease the dependence on fossil fuels. The development of trustworthy and environment friendly energy storage devices is crucial for a sustainable society. SCs and rechargeable batteries are becoming a significantly important part of our daily lives because of their high energy and power densities for powering various electronic gadgets, hybrid electric vehicles, and many miniaturized devices.[128–130] As we know that the performance of energy storage devices depends primarily on active electrode materials, electrode materials must possess reversible redox reactions, numerous surface-active sites, easy access to electrolyte ions, long-term stability, and good electrical conductivity.[131] Since the previous decade, most of the energy storage devices have employed carbon-based materials as they show excellent electrochemical performance and superior mechanical strength. Other 2D materials such as TMDs, black phosphorene, and silicane also demonstrate superior energy storage performance because of their high specific surface area and short diffusion pathways.[132] The 2D materials possess one atomic layer thickness, numerous electroactive sites, and superior mechanical properties, which fulfill the requirements of typical energy storage devices.[133] Moreover, newly existing MXenes display large intrinsic specific surface areas, superior electrical conductivity, good mechanical strength, and they are significantly promising candidates for energy storage devices such as SCs and rechargeable batteries.[134] In this section, we outline current research advances on MXenes and their derivatives for SCs and rechargeable batteries. As active electrode materials, MXenes

have good application prospects and are considered as leading contenders in the energy storage field.

4.1 MXenes and their derivatives for supercapacitors

SCs have attracted significant research interest owing to their fascinating features such as high-power density, fast charge/discharge rates, and long-term stability. According to the energy storage mechanism, SCs can be classified into two major categories: EDLCs and pseudocapacitors.[135] EDLCs store energy *via* the physical adsorption of electrolyte ions at the interface without faradaic reactions.[136] Consequently, EDLCs have a relatively long cycling life and the energy storage process is highly reversible. When compared to EDLCs, pseudocapacitors store energy through the transfer of charge between the surface of the electrode and the electrolyte, thereby involving reversible redox reactions.[137] Therefore, pseudocapacitors exhibit higher capacitance and energy density than EDLCs as the redox reactions occur both on the surface of electrodes and in their bulk. However, pseudocapacitors often suffer from inferior rate capability and sluggish cycling stability owing to the kinetics of regular redox reactions. To overcome these issues, hybrid SCs, with a combination of both faradaic and non-faradaic mechanisms of charge storage, have been proposed to provide high energy density without surrendering other features such as power density and cycling stability. MXenes with open tunnels can be instinctively intercalated by metal ions and organic molecules. These promising features of MXenes with their hydrophilic surfaces make them active materials for high-performance SCs. The porosity, interlayer spacing, and surface functional groups significantly influence the performance of MXene-based electrodes in SCs. The large interlayer spacing of MXene assists the easy intercalation of metal ions or organic molecules. Among the MXene family, $Ti_3C_2T_x$ has been widely employed for SCs owing to its eminent etching conditions and the detailed theoretical and experimental aspects of its energy storage performance.

The restacking of $Ti_3C_2T_x$ MXene nanoflakes was significantly reduced, and layered $Ti_3C_2T_x$ films were prepared by Xu et al.[138] using a modified electrophoretic deposition method (Fig. 9a). The periodic 2D interlayer structure of $Ti_3C_2T_x$ significantly improved ion and electron transportation (Fig. 9b–j). Cation intercalation into $Ti_3C_2T_x$ in an alkaline electrolyte is generally recognized as an electrochemical redox reaction on the surface, which depends on the change in the oxidation state of Ti.

$$Ti_3C_2O_x(OH)_yF_z + \delta e^- + \delta K^+ \rightarrow K_\delta Ti_3C_2O_x(OH)_yF_z \quad (8)$$
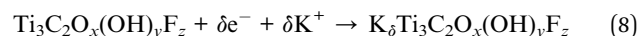
The H$^+$ cations formed after the dispersion of $Ti_3C_2T_x$ nanoflakes into an iodoacetone solution were intercalated into the $Ti_3C_2T_x$ layers. A maximum specific capacitance of 140 F g^{-1} at 5 mV s^{-1} was obtained for the sample with 1.2 mg mass loading and 78.5% charge was maintained at a scan rate of 50 mV s^{-1}. The gravimetric capacitance of MXene-based materials is still low; therefore, researchers are attempting to enhance the capacitance by increasing the number of surface-
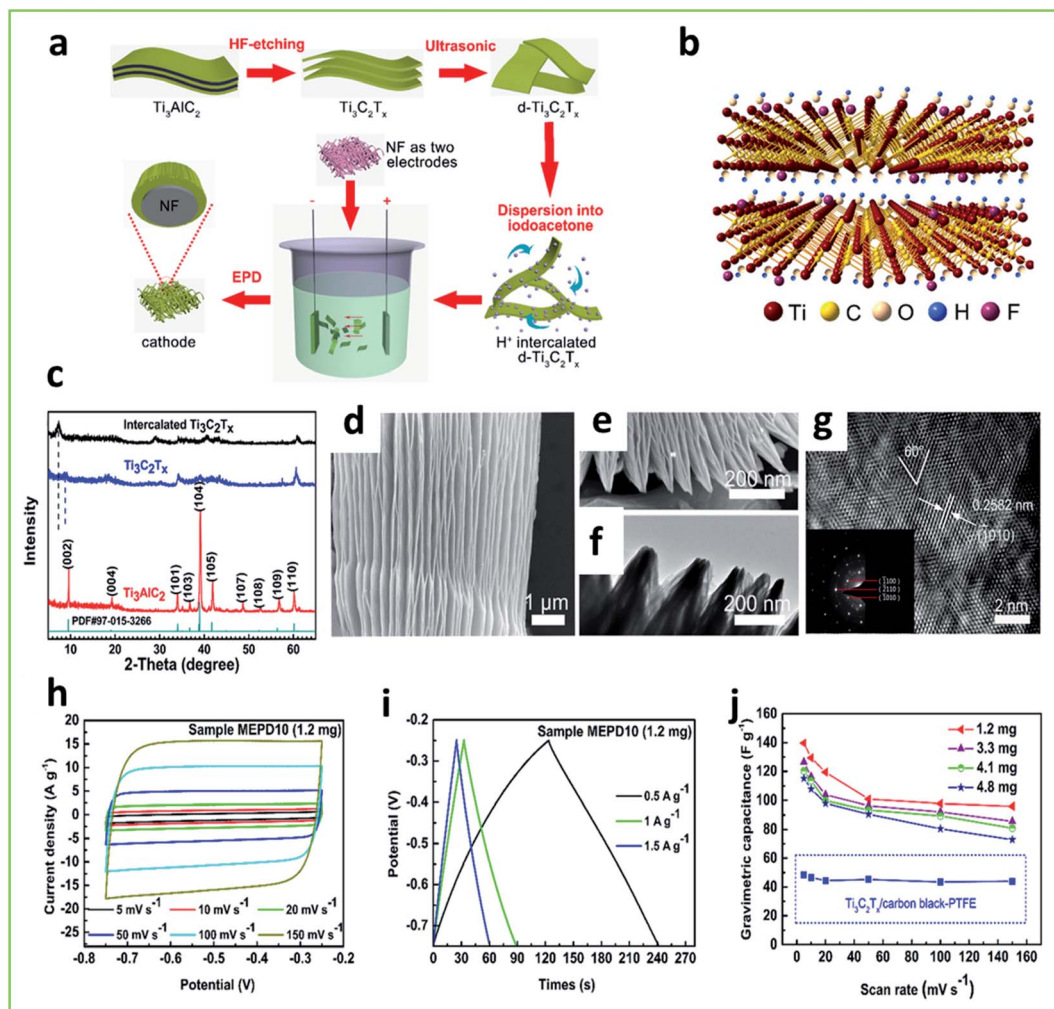
This journal is © The Royal Society of Chemistry 2022

J. Mater. Chem. A, 2022, 10, 1105–1149 | 1117

Fig. 9 (a) Schematic protocol for the synthesis of $Ti_3C_2T_x$-based electrode; (b) molecular structure model of single-layer d-$Ti_3C_2T_x$; (c) XRD patterns; (d–g) SEM and TEM images of $Ti_3C_2T_x$ nanoflakes; (h) cyclic voltammetry (CV) curves at different scan rates; (i) galvanostatic charge/discharge (GCD) curves at different current densities; (j) gravimetric capacitances of the prepared four different d-$Ti_3C_2T_x$ films and the $Ti_3C_2T_x$/carbon black-polytetrafluoroethylene electrodes *versus* scan rate. (a–j) Are adapted with permission.[138] Copyright 2017, Elsevier.

active sites. The energy storage performance of MXenes is strongly dependent on the surface terminal groups. The removal of surface functional groups –F and –OH affect the transportation of electrolyte ions, which decreases the energy storage capability. Till date, the highest gravimetric capacitance of 245 F g^{-1} has been reported for pristine MXene.[17] Lukatskaya *et al.*[139] reported the capacitive mechanism of $Ti_3C_2T_x$ MXene through *in situ* X-ray absorption spectroscopy. The authors determined that the pseudocapacitance of $Ti_3C_2T_x$ MXene was initiated by the surface redox reactions of Ti species. The charge transport in the SC electrode is assisted by the increase in the interlayer spacings of $Ti_3C_2T_X$ MXene.

Cation intercalation and surface modification of MXenes were reported to be effective methods for improving their performance. K-ion intercalation in $Ti_3C_2T_x$ MXene increases the interlayer spacing to 0.77 nm, where –OH/–F terminated MXene sheets have initial spacing of 0.2 nm.[141] The schematics of the synthesis procedure are shown in Fig. 10a. The X-ray diffraction (XRD) results demonstrated broadening and a shift

to lower 2θ for the (002) phases with K-ion intercalation, indicating that lattice expansion occurs along the *c*-axis (Fig. 10b). K-ion-intercalated MXenes were annealed at 400 °C in an Ar environment to remove the surface functional groups, increasing the interlayer voids from 4.8 to 7.7 AU (Fig. 10c–f). The K-ion-intercalated $Ti_3C_2T_x$ MXene showed a gravimetric capacitance of 517 F g^{-1} (Fig. 10g and h). The electrode exhibited good reversibility during the charge/discharge process and outstanding stability with 99% capacity retention over 10 000 cycles (Fig. 10i). Similarly, cation (Na^+, Mg^+, and Li^+) intercalation in delaminated d-V_2CT_x MXene was studied by Mohammadi *et al.*[142] They observed that cation intercalation is considerably significant in altering chemically unstable MXenes to highly stable electrodes to enhance the electrochemical performance of V_2CT_x. The schematic protocol for cation intercalation into diluted V_2CT_x, which results in water dispersion, is shown in Fig. 11a. The electrostatic attraction between positively charged cations and negatively charged MXenes forms multilayer V_2CT_x MXene (Fig. 11b–d). The XRD patterns
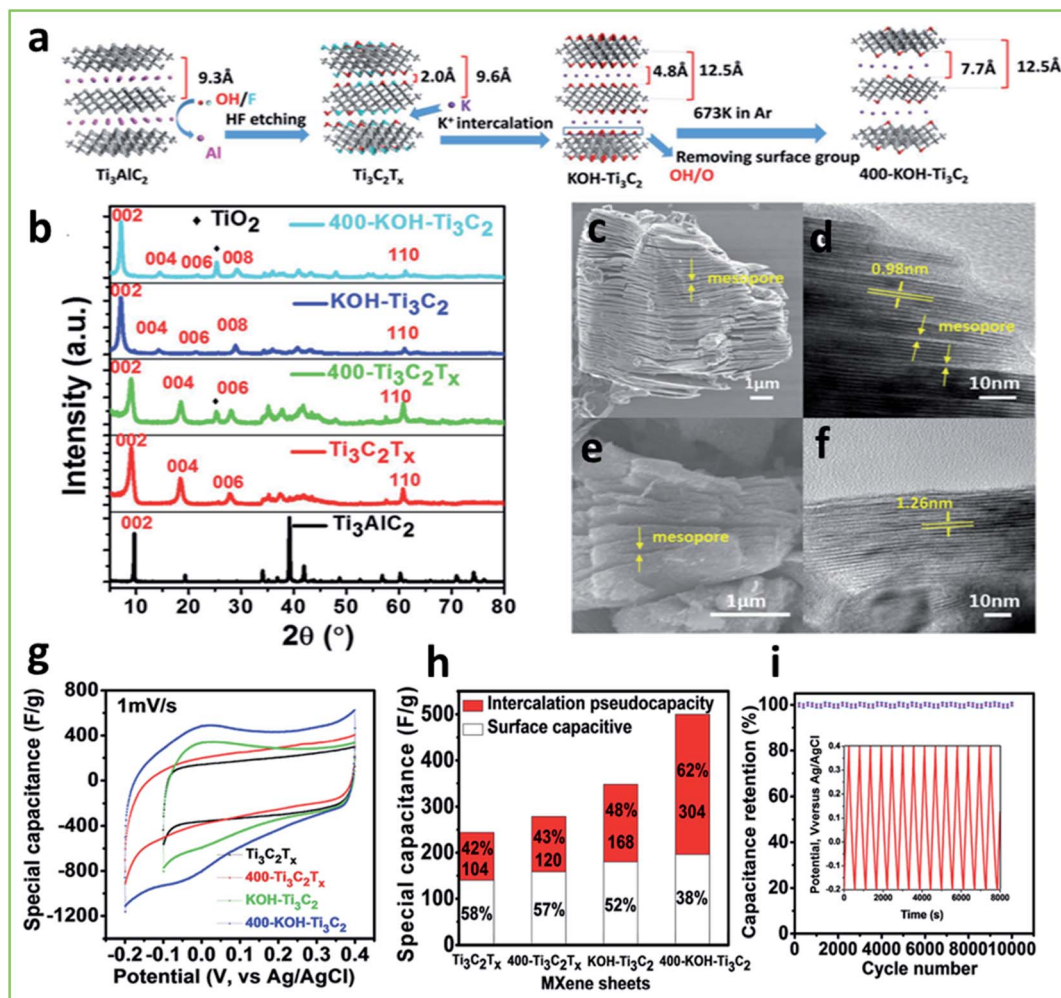
Fig. 10 (a) Schematic illustration of the synthetic process of K-ion-modified MXene; (b) XRD patterns; (c and d) SEM and TEM images of conventional $Ti_3C_2T_x$; (e and f) SEM and TEM images of K-ion-modified $Ti_3C_2T_x$ annealed at 400 °C; (g) CV curves at 1 mV s^{-1}; comparison of (h) capacitance and (i) capacitance retention with cycle number for 400-KOH-Ti_3C_2 electrode. Inset shows galvanostatic cycling data collected at 1 A g^{-1}. (a–i) Are adapted with permission.[140] Copyright 2017, WILEY-VCH.

for cation-intercalated V_2CT_x MXenes show small variations in peak positions related to the (0002) plane (Fig. 11e). When compared to all cations, Na-intercalated V_2CT_x MXenes demonstrated a larger interlayer spacing of 1.26 nm; conversely, Li-intercalated V_2CT_x MXenes showed smaller interlayer spacing. The Na-intercalated V_2CT_x MXene electrode showed a maximum specific capacitance of 285 F g^{-1} in the $ZnSO_4$ electrolyte (Fig. 11g). The electrode exhibited superior cycling stability after 10 000 cycles (without loss of capacitance), whereas the electrode retained 77% capacity retention after 1 million cycles at 100 A g^{-1} (Fig. 11h).

Similar to other 2D materials, the restacking of MXene layers during their synthesis is one of the biggest concerns that minimizes the active surface area and accessibility of electrolyte ions. To avoid restacking and improve the electrolyte ion accession, modification of the MXene layer was performed. Zhu et al.[143] developed expanded MXene and MXene foam using a hard template and pore forming method, as illustrated in Fig. 12a. Authors used MgO as a hard template to avoid the restacking of MXene layers. The XRD pattern showed the influence of the hard MgO template on the structure of exfoliated MXene, with a strong low-angle shift in the (002) peak (Fig. 12b). The XRD pattern showed a high-angle shift in the (002) peak for the MXene foam, indicating a decrease in interlayer spacing owing to the hydrolysis of H_2O molecules in the MXene layers during annealing (Fig. 12c). The MXene foam electrode showed a maximum specific capacitance of 203 F g^{-1}, while the pristine MXene and expanded MXene electrodes exhibited specific capacitances of 80 and 112 F g^{-1}, respectively. The avoidance of the restacking of MXene layers increases the utilization of the active surface area and improves the diffusion and transportation of electrolyte ions (Fig. 12f–h).

Activated carbon (AC) cloth was prepared by treating carbon cloth with potassium permanganate, which demonstrated improved specific area, O-containing functional group, hydrophilicity, and electrical conductivity. The coating of $Ti_2C_2T_x$ on such AC cloth resulted in a capacitance of 1033 mF cm^{-2} at 1 mA cm^{-2}.[144] Zhao et al.[145] reported the synthesis of a $Nb_4C_3T_x$
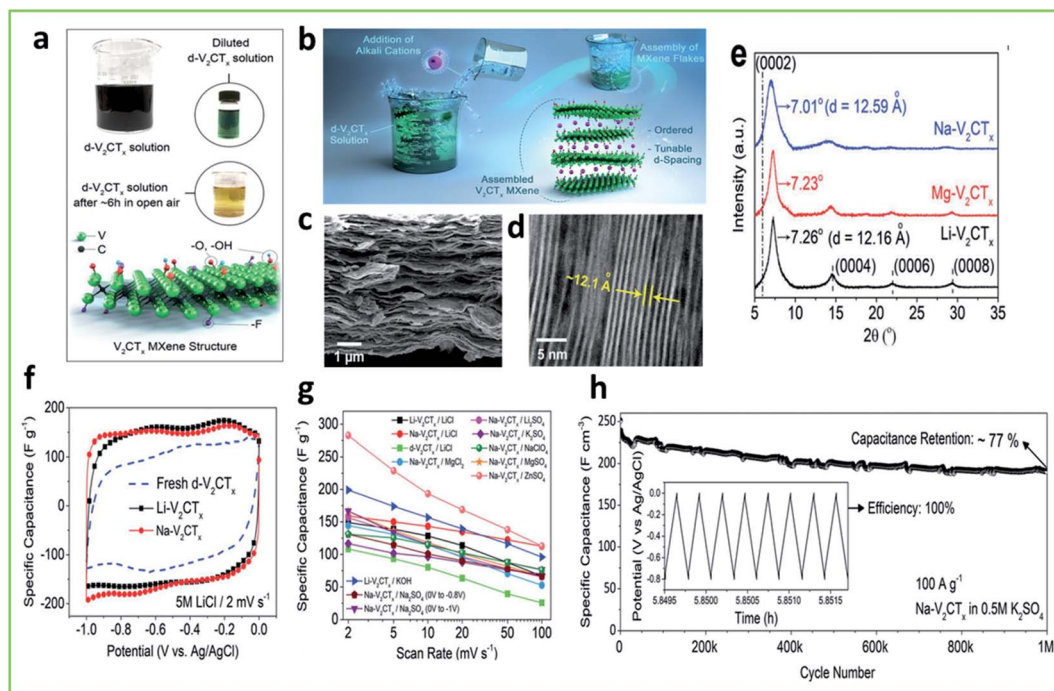
Fig. 11 (a) Digital photographs of a fresh and diluted d-V_2CT_x solution; (b) schematic illustrations for the fabrication of the ordered and highly stable V_2CT_x flakes; (c and d) SEM and TEM images of a Li–V_2CT_x film; (e) XRD patterns, (f) CV profiles of electrodes in 5 M LiCl electrolyte at 2 mV s^{-1}; (g) gravimetric capacitance *versus* scan rate; (h) stability performance of Na–V_2CT_x electrode in a K_2SO_4 electrolyte. (a–h) Adapted with permission.[142] Copyright 2019, WILEY-VCH.

nanosheet film with 1.77 nm interlayer spacing. The SC performance of the $Nb_4C_3T_x$ electrode was tested in acidic, alkaline, and neutral electrolytes. $Nb_4C_3T_x$ showed volumetric capacitances of 1,075, 687, and 506 F cm^{-3} in 1 M of H_2SO_4, KOH, and $MgSO_4$, respectively. Earlier reports showed that the incorporation of graphene nanosheets between MXene flakes is a significantly effective strategy to restrain the self-restacking of MXene flakes. Fan *et al.*[146] reported the preparation of MXene/holey graphene composite film through a filtration method followed by annealing treatment. Holey graphene impedes the agglomeration of MXene and creates a highly connective network. The composite film electrode exhibited a high volumetric capacitance of 1445 F cm^{-3}. The *in situ* growth of multiwalled carbon nanotubes (MWCNTs) on carbon-cloth-supported MXene is promising for flexible SCs.[147] The MWCNTs prevent the restacking of MXene and act as intra-particle and interparticle charge collectors. The electrode exhibited an areal capacitance of 114.58 mF cm^{-2} at a current density of 1 mA cm^{-2}. Furthermore, a $Ti_3C_2T_x$/reduced graphene oxide (rGO) composite electrode that was prepared by Zhou *et al.*[148] demonstrated a capacitance of 49 mF cm^{-2} and superior electrochemical and mechanical stability under cyclic uniaxial (300%) and biaxial (200% × 200%) strains. Yu *et al.*[149] prepared MXene-bonded AC electrodes, where AC particles were encapsulated into MXene layers to form binder-free electrodes. The MXene-bonded AC electrode achieved specific capacitance of 126 F g^{-1} at a current density of 0.1 A g^{-1}.

Owing to the outstanding metallic conductivity, hydrophilic surface, and mechanical properties of MXenes, MXene

composites with polymers enhances the mechanical and thermal properties of polymers.[150] Fu *et al.*[151] developed a facile synthesis approach to develop graphene-encapsulated Ti_2CT_X MXene@polyaniline (GMP) composite with improved electrochemical performance. The schematic protocol for the synthesis of GMP is shown in Fig. 13a. An accordion-like morphology with well-stacked nanosheets was observed for pure Ti_2CT_x MXene, whereas for Ti_2CT_X MXene@polyaniline (MP), polyaniline (PANI) granules were uniformly grown over Ti_2CT_X MXene, maintaining well-stacked nanosheets (Fig. 13b–d). For the GMP composite, chemically converted graphene (CCG) sheets covered the MP nanostructure well. Moreover, TEM images evidently proved that the composite material was composed of three different materials, *i.e.*, outer CCG sheets, central PANI, and interior accordion-like MXene, with an interlayer spacing of 1.32 nm related to the (0002) plane of MXene (Fig. 13e–g). Benefiting from the three different materials, the GMP composite provides a large surface area for electrolyte ion accession and high conductivity. The GMP electrode achieved a maximum specific capacitance of 635 F g^{-1} at a current density of 1 A g^{-1} and superior capacity retention of 97.54% over 10 000 cycles (Fig. 13h–j). Moreover, conjugated microporous polymers (CMPs) have various advantages over traditional polymers, such as low cost, high specific surface area, and three-dimensional (3D) network structure. However, the poor electrical conductivity of CMPs hinders their widespread application in various fields. Yang *et al.*[152] constructed MXene-based CMPs through covalent sandwiching of MXene between CMPs to improve the stability of MXenes and

1120 | *J. Mater. Chem. A*, 2022, **10**, 1105–1149

This journal is © The Royal Society of Chemistry 2022
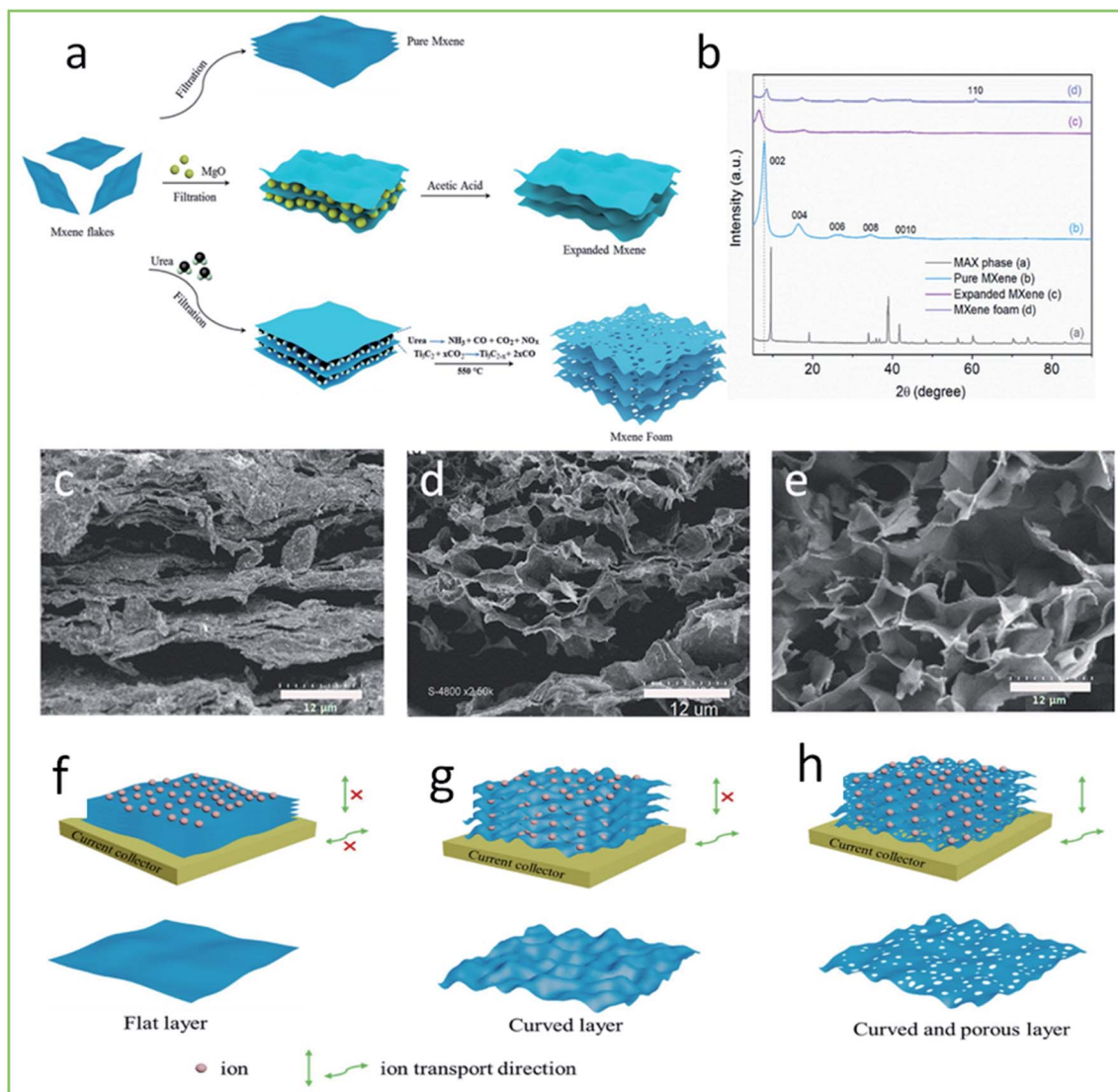
Fig. 12 Schematic of the preparation of different forms of MXene as restacked material after exfoliation (top), expanded MXene after restacking in the presence of MgO nanoparticles (middle), and MXene foam from thermal treatment in the presence of urea (bottom); (b) XRD patterns of MXenes; SEM images of (c) $Ti_3C_2T_x$-MXene, (d) expanded $Ti_3C_2T_x$-MXene, (e) and $Ti_3C_2T_x$-Mxene foam; (f–h) schematic showing ion transport in different MXene morphologies. (a–h) Adapted with permission.[143] Copyright 2020, Elsevier.

conductivity of CMPs. The MXene-CMP electrode exhibited improved structural properties and rich O-containing redox-active functional groups. Le et al.[153] reported the in situ synthesis of $Ti_3C_2T_x$@polypyrrole nanowires, which effectively prevented the aggregation of $Ti_3C_2T_x$ and enhanced the performance of SCs. The $Ti_3C_2T_x$@polypyrrole nanowires exhibited a specific capacitance that was five times higher than that of pristine $Ti_3C_2T_x$ and 100% capacity retention over 14 000 cycles. The intercalation of polypyrrole into layered $Ti_3C_2T_x$ by electrochemical polymerization enhances the capacitance of polypyrrole from 150 to 203 mF cm^{-2} and demonstrates 100% capacitance retention after 20 000 cycles.[154]

Lu et al.[155] designed Ni_2Co-LDHs@AL-Ti_3C_2-MXene sandwich-type composite. The synthesis protocol for the sandwich-type composite is shown in Fig. 14a. The surface of the Ni_2Co-LDHs@AL-Ti_3C_2MXene composite exhibited

a honeycomb-like morphology with 2D sheets covered by vertical ultrathin layers. The Ni_2Co-LDH sheets with 80 nm thickness uniformly covered the complete three-layer Ti_3C_2 MXene (Fig. 14b–d). In the XRD pattern, the shifting of the (002) peak of Al-Ti_3C_2 MXene towards a lower angle indicates an increase in the interplanar spacing. However, owing to the thick coating of Ni_2Co-LDHs over AL-Ti_3C_2-MXene, the composite material showed an absence of the (002) peak. Moreover, DFT calculations proved that the flexible interfaces lower the hydrogen adsorption energy (1.67–1.47 eV), indicating easy hydrogen desorption on the surface of Ni_2Co-LDHs facilitating redox reactions. From Ni_2Co-LDHs to Al-Ti_3C_2 MXene, 1.07 electrons were transferred per unit cell, causing movement of the Fermi level owing to the electron-rich Al-Ti_3C_2 MXene and hole-rich Ni_2Co-LDHs. An increase in the DOS of Ni_2Co-LDHs@AL-Ti_3C_2MXene than that of the pristine Ni_2Co-LDHs

This journal is © The Royal Society of Chemistry 2022

J. Mater. Chem. A, 2022, **10**, 1105–1149 | **1121**

Fig. 13 (a) Schematic protocol for the synthesis of graphene@MXene@polyaniline (GMP) composite; SEM images of (b) MXene, (c) MXene@-polyaniline, and (d) graphene@MXene@Polyaniline; (e–g) TEM images of GMP; inset of (f) shows HRTEM image of the chemically convert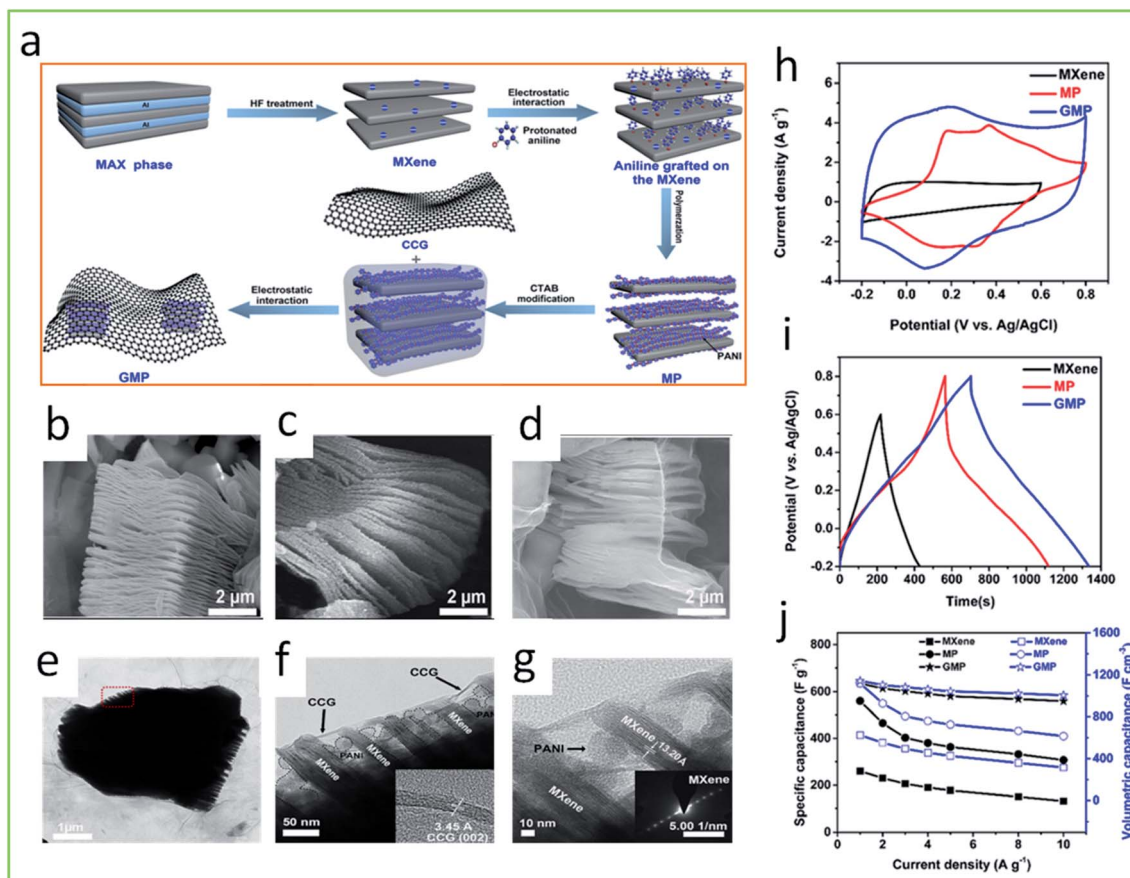ed graphene; inset of (g) shows the SAED pattern of the layered structure of MXene, (h) CV curves of MXene, MXene@polyaniline (MP), GMP at 5 mV s^{-1}; (i) GCD curves of MXene, MP, and GMP at 1 A g^{-1}; (j) specific capacitance values of the MXene, MP, and GMP at different current densities. (a–j) Are adapted with permission.[151] Copyright 2018, American Chemical Society.

surrounding the Fermi level confirmed the increased conductivity and charge transfer kinetics of the composite (Fig. 14e–h). The electrode demonstrated typical battery-type behavior with strong reversible redox reactions of Ni^{3+}/Ni^{2+} and Co^{3+}/Co^{2+} (Fig. 14i–k). The Ni_2Co-LDHs@AL-Ti_3C_2MXene electrode achieved the highest specific capacity of 227 mA h g^{-1} at a current density of 1 A g^{-1}. Furthermore, the Ni_2Co-LDHs@AL-Ti_3C_2 MXene electrode demonstrated 90% capacitance retention after 10 000 cycles, which is significantly high when compared to that of pristine Ni_2Co-LDHs (17%).

Using magneto-hydrothermal synthesis, 2D/2D 1T MoS_2/$Ti_2C_2T_x$ heterostructure was prepared, which combines the features of each 2D material and shows improved electrochemical properties.[156] The 1T MoS_2/Ti_2C_2Tx exhibits a specific capacitance of 386.7 F g^{-1} at a current density of 1 A g^{-1} and outstanding rate performance. Rakhi et al.[157] synthesized nanocrystalline ε-MnO_2 nanowhiskers on MXene surfaces (ε-MnO_2/Ti_2CT_X and ε-MnO_2 $Ti_3C_2T_x$) for aqueous SCs. Authors observed that ε-MnO_2 nanowhiskers increased the surface area and enhanced the specific capacitance by three times when compared to pristine MXenes. To improve the conductivity and stability of WO_3, Ambade et al.[158] developed WO_3–Ti_2CT_X

hybrids via a one-step hydrothermal method. The comparison of the electrochemical performance reveals almost double the specific capacitance than the hybrid electrode. The MXene@poly (diallyldimethylammonium chloride) (PDDA)/NiAl-LDH hybrid electrode prepared by an electrostatically assembled approach combines the high electrical conductivity of MXene and high redox activity of PDDA/NiAl-LDHs.[159] The electrode achieved a high specific capacitance of 1825.8 F g^{-1} at a current density of 1.0 A g^{-1} and superior cyclic stability with only 0.9% degradation after 5000 cycles. Flexible hybrid paper with Fe_2O_3 nanoparticles anchored on $Ti_2C_2T_x$ was prepared by electrostatic self-assembly followed by an annealing process.[160] The interlayer spacing between $Ti_2C_2T_x$ layers was significantly increased by the incorporation of Fe_2O_3 nanoparticles with more electrochemically active sites. The Fe_2O_3–$Ti_3C_2T_x$ electrode achieved a wide potential window of 1 V and high volumetric capacitance of 2607 F cm^{-3}. Similarly, NiMn-LDH/MXene,[161] $CoFe_2O_4$/MXene,[162] and Ti_3C_2/NiCoAl-LDH[163] composites were prepared for SCs.

Heteroatom doping is one of the most effective approaches for enhancing the electrochemical performance of SC electrodes. The doping of foreign atoms can significantly reduce the
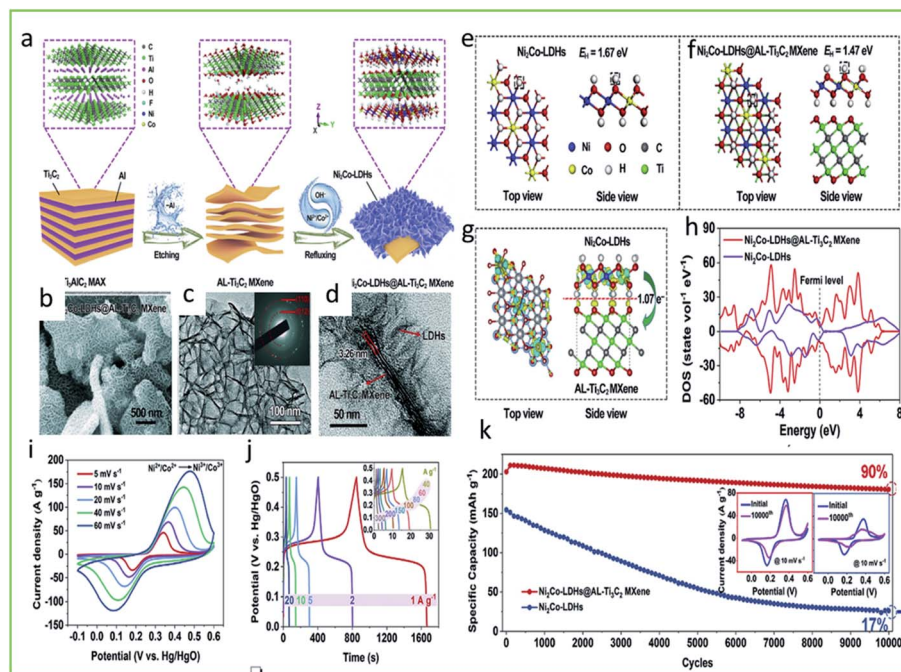
1122 | J. Mater. Chem. A, 2022, 10, 1105–1149

This journal is © The Royal Society of Chemistry 2022

Fig. 14 (a) Schematic protocol for the fabrication of Ni$_2$Co-LDHs@AL-Ti$_3$C$_2$MXene sandwich-type composite; (b–d) SEM and TEM images of the Ni$_2$Co-LDHs@AL-MXene composite; optimized structures of (e) pure Ni$_2$Co-LDHs and (f) Ni$_2$Co-LDHs@AL-MXene (top and side views); (g) distribution of charge in flexible/stiff interface; (h) DOS of Ni$_2$Co-LDHs and Ni$_2$Co-LDHs@AL-MXene composite; (i) CV curves, (j) GCD curves, and (k) cycling performance of all the electrodes at 10 A g^{-1}. (a–k) Are adapted with permission.[155] Copyright 2020, Elsevier.

restacking of MXene layers and increase the interlayer distance. Pan *et al.*[164] developed a simple synthesis approach to prepare N, O co-doped C@Ti$_3$C$_2$ MXenes through *in situ* polymerization in Ar and NH$_3$ atmospheres (Fig. 15a). SEM images of the synthesized samples are illustrated in Fig. 15b–d. The presence of O-doped carbon enhances the hydrophilicity of the material, while N-doped carbon acts as an electron donor, which significantly helps in the displacement of the Fermi level and improves the conductivity of the material. The XRD pattern reveals lower angle shifting of (002) peaks of mixtures of Ti$_3$C$_2$ and AC after sintering by 2.3°, indicating an increase in the interlayer spacing to 1.34 nm after polymerization (Fig. 15e). Raman analysis showed I_D/I_G ratios of 1.62, 1.51, 1.43,1.18, and 0.31 for AT2-NH$_3$, AT2-Ar, Ti$_3$C$_2$-NH$_3$, Ti$_3$C$_2$-Ar, and Ti$_3$C$_2$, respectively (Fig. 15f). Fig. 15g shows the reversible redox reactions associated with the Ti$_3$C$_2$ and N and O dopants in the carbon material. The composite shows the presence of more defects in the carbon material due to the presence of N and O doping after calcination in the NH$_3$ atmosphere. The N, O co-doped C@Ti$_3$C$_2$ MXene electrode showed a high specific capacitance of 260.5 F g^{-1}, which is 3.5 times higher than that of pure Ti$_3$C$_2$ (Fig. 15i) and 94% capacity retention after 5000 cycles. Lu *et al.*[165] comprehensively illustrated the N doping mechanism in Ti$_3$C$_2$T$_x$ using theoretical simulations and experimental studies. The N atoms can be accommodated into three possible sites in Ti$_3$C$_2$T$_x$, *i.e.*, lattice substitution (for carbon), functional substitution (for –OH), and surface absorption (for –O). All three N dopants are favorable for enhancing the specific capacitance of Ti$_3$C$_2$T$_x$. Li *et al.*[166]

successfully demonstrated the intercalation of different metal ions into the Ti$_3$C$_2$T$_x$ electrode in different neutral multivalent electrolytes. Different metal ions, such as alkaline earth metal ions (Be^{2+}, Mg^{2+}, Ca^{2+}), lanthanide ions (Gd^{3+}, Tb^{3+}, Ho^{3+}) transition metal ions (Ag$^+$, Cu^{2+}, Mn^{3+}, Cr^{3+}, Fe^{3+}), and post-transition metal ions (Al^{3+}, In^{3+}) were intercalated into the Ti$_3$C$_2$T$_x$ multilayers. Among all the intercalated metal ions, Be^{2+}-Ti$_3$C$_2$T$_x$ and Al^{3+}-Ti$_3$C$_2$T$_x$ electrodes are favorable for the charge transfer process. Be^{2+}-Ti$_3$C$_2$T$_x$ electrode demonstrates the highest capacitance and high-rate performance in different electrolytes with highest volumetric capacitance of 591.4 F cm^{-3} in ZnSO$_4$. Three-dimensional MXene/N-doped carbon foam (MXene/NCF) prepared using one-step pyrolysis combines various features to enhance the conductivity and hydrophilicity. The MXene/NCF electrode demonstrates gravimetric and volumetric capacitance of 332 F g^{-1} and 3162 mF cm^{-3}, respectively.[167] Ag nanoparticle-decorated Ti$_3$C$_2$T$_x$ hybrid film electrode achieved a high specific surface area of 107 m^2 g^{-1} and areal capacitance of 332.2 mF cm^{-2}.[168]

MXenes show outstanding electrochemical performance as active materials for SCs owing to their superior features of good flexibility, hydrophilicity, and layered 2D structure. Presently, various studies have been conducted on their applications in different SC devices, such as symmetric, asymmetric, hybrid, and micro-SC (MSC) devices. This section comprehensively discusses the recent processes in MXene-based SC devices.

4.1.1 MXene-based symmetric supercapacitor devices. MXene-based symmetric SCs have been extensively studied. The utilization of fiber substrates for SCs is not new; however, the
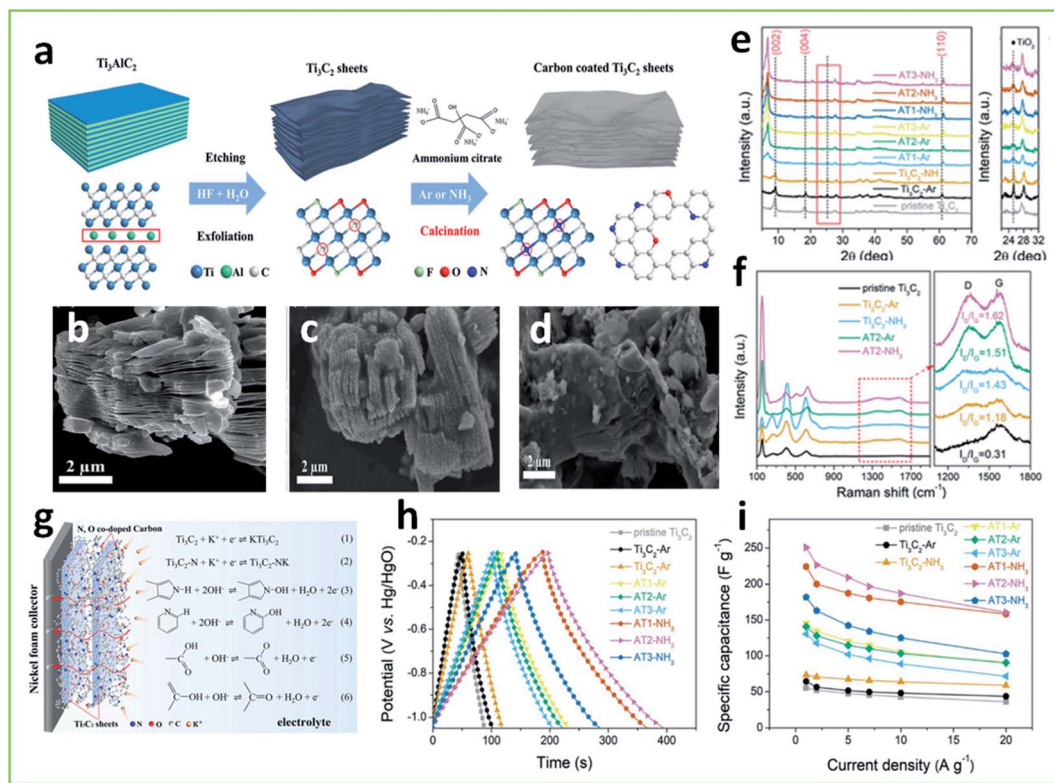
This journal is © The Royal Society of Chemistry 2022

J. Mater. Chem. A, 2022, **10**, 1105–1149 | **1123**

Fig. 15 (a) Schematic illustration of the synthesis process and reaction mechanism of composites; SEM images of (b) Ti_3C_2, (c) Ti_3C_2-NH_3, and (d) AT2-NH_3; (e) XRD patterns and corresponding enlarged XRD patterns of all samples; (f) Raman shifts and enlargement of the equivalent region; (g) schematic diagram of reaction mechanism of charge/discharge process; (h) GCD curves and (i) specific capacitance at all current densities. (a–i) Are adapted with permission.[164] Copyright 2019, Elsevier.

assembly of MXene-based fibers in a regular arrangement is still challenging owing to the insufficient interlaminar interactions between MXene sheets. Yang *et al.*[141] reported a wet-spinning strategy for the continuous fabrication of MXene-based fibers based on the synergistic effect between graphene oxide liquid crystals and MXene sheets. All solid-state MXene fiber-based symmetric SCs show volumetric capacitance of 586.4 F cm^{-3}. $Ti_3C_2T_x$-based symmetric SCs developed by Tian *et al.*[169] show an unequal split in the voltage between the positive and negative electrodes in H_2SO_4 electrolyte. After the incorporation of redox-active electrolyte, symmetric SCs achieved a volumetric energy density of 33.2 W h L^{-1} and maintained 113.5% of the initial capacity after 10 000 cycles. Furthermore, $Ti_3C_2T_x$//$Ti_3C_2T_x$ symmetric SCs fabricated by Xia *et al.*[170] revealed a volumetric specific capacitance of 27.4 F cm^{-3} at 0.25 A g^{-1}, and 96.6% capacitance retention after 5000 cycles. Polypyrrole/$Ti_3C_2T_x$ nanocomposite electrodes were fabricated through the *in situ* polymerization of symmetric SCs. The SCs deliver energy density of 21.61 W h kg^{-1} at a power density of 499.94 W kg^{-1} with 73.68% capacitance retention after 4000 charge and discharge tests.[171] Ramchandran *et al.*[172] developed MXene/non-peripheral octamethyl-substituted copper(II) phthalocyanine (N-CuMe$_2$Pc) composite for SCs. The incorporation of redox-active N-CuMe$_2$Pc into MXene leads to a large surface area and surface-active sites for electrochemical reactions. The symmetric SCs showed an energy density of 8.84 W h kg^{-1} with

a power density of 112.3 W kg^{-1} and cyclic stability of 92.3% after 20 000 cycles. An all-solid-state flexible symmetric SC based on 1T MoS_2/$Ti_3C_2T_x$ demonstrated areal capacitance of 347 mF cm^{-2} at 2 mA cm^{-2}, high energy and power densities with 98.6% initial capacitance after 10 000 cycles, and only 8.9% loss after 20 000 cycles.[173] Symmetric solid-state SCs with Fe_2O_3–$Ti_2C_2T_x$ achieves energy density of 29.7 W h L^{-1} and superior mechanical flexibility.[160]

4.1.2 MXene-based asymmetric supercapacitor devices. The energy density of MXene-based symmetric SCs is significantly low, as the voltage window obtained with MXene electrodes in aqueous electrolytes is not wide. Therefore, an asymmetric SC design is a trustworthy choice to attain a high energy density. Generally, carbon-based materials have been utilized as negative electrodes to construct asymmetric SCs with pseudocapacitive and battery-type materials as positive electrodes. However, the capacitance of such asymmetric SCs is not satisfactory because low-capacitance carbon materials cannot compete with high-capacitance positive electrodes. As MXene is a pseudocapacitive material that works in a negative voltage window, combining it with other positive pseudocapacitive and battery-type electrode materials can broaden the voltage window to attain high capacitance and energy density.[174,175] Li *et al.*[176] successfully attained high volumetric energy and power densities with flexible asymmetric SCs with $Ti_3C_2T_x$ as the negative electrode and rGO/CNT/PANI as the positive electrode

1124 | *J. Mater. Chem. A*, 2022, **10**, 1105–1149

This journal is © The Royal Society of Chemistry 2022
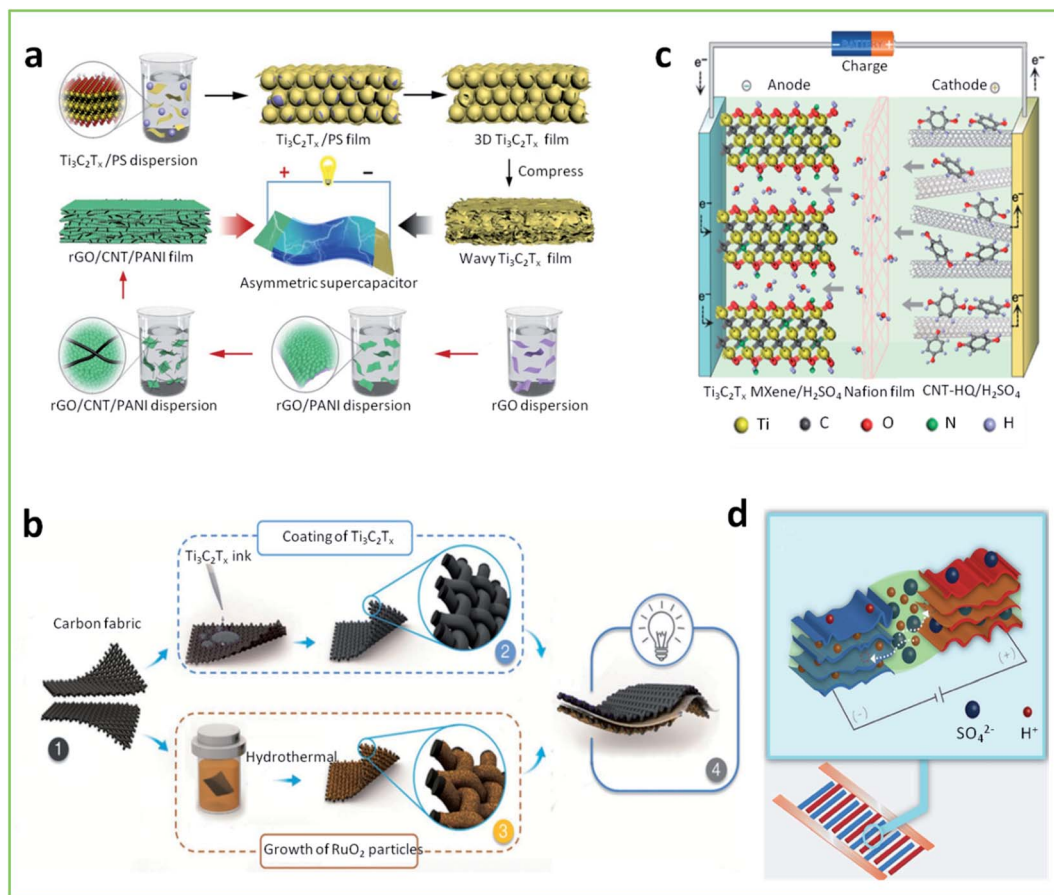
Fig. 16 Schematic illustration showing the fabrication process of (a) $Ti_3C_2T_x$//reduced graphene oxide (rGO)/carbon nanotube (CNT)/polyaniline, (b) $Ti_3C_2T_x$//RuO$_2$ (b) $Ti_3C_2T_x$//CNT-hydroquinone, and (d) $Ti_3C_2T_x$//(rGO) asymmetric supercapacitors. (a) Is adapted with the permission.[176] Copyright 2020, Elsevier. (b) Is adapted with permission.[177] Copyright 2018, WILEY-VC. (c) Is adapted with permission.[178] Copyright 2019, American Chemical Society. (d) Is adapted with permission.[187] Copyright 2017, WILEY-VCH.

(Fig. 16a). The device delivered a volumetric energy density of 70 W h L^{-1} at a power density of 111 kW L^{-1} in H$_2$SO$_4$ aqueous electrolyte, while in PVA/H$_2$SO$_4$ gel electrolyte, a volumetric energy density of 63.5 W h L^{-1} at a power density of 34.3 kW L^{-1}. Jiang *et al.*[177] fabricated asymmetric SCs with $Ti_3C_2T_x$ as the negative electrode and RuO$_2$ as the positive electrode (Fig. 16b). The prepared RuO$_2$//$Ti_3C_2T_x$ asymmetric device achieved a voltage window of 1.5 V and demonstrated an energy density of 37 μW h cm^{-2} at 40 mW cm^{-2}. This device exhibits the limitations of high cost of RuO$_2$ and poor cycling stability of polymers; alternatively, high-performance asymmetric SCs can be achieved using redox-active electrolytes. Hydrogen-ion aqueous-based asymmetric SCs were constructed using a redox-active hydroquinone-H$_2$SO$_4$ electrolyte with CNT as the positive electrode and $Ti_3C_2T_x$ as the negative electrode (Fig. 16c).[178] The prepared device worked in a large potential window of 1.6 V and delivered a high energy density of 62 W h kg^{-1} at a power density of 281 W kg^{-1}. The authors proved that the incorporation of a redox-active electrolyte improves the overall performance of asymmetric SCs. All-pseudocapacitive organic–inorganic asymmetric device constructed with MXene cathodes and rGO-polymer anode worked

in a voltage window of 1.45 V in 3M H$_2$SO$_4$ electrolyte and delivered energy density of 14 W h kg^{-1}.[179] Moreover, asymmetric SCs based on MXenes, but without the aforementioned limitations have also been fabricated such as, MXene/CoS$_2$//rGO,[180] polyaniline/MXene//MXene,[156] Co$_3$O$_4$-MXene/rGO//AC,[181] Ti_3C_2/CuS//Ti_3C_2,[164] and Ti_3C_2/NiCoAl-LDH//AC.[163] Further, owing to their high conductivity, MXenes can be easily coupled with poor-conductivity metal oxides to improve electron transfer. MXene ink was easily coated on Fe$_2$O$_3$-coated carbon cloth. Asymmetric SCs fabricated with MnO$_2$ as the positive electrode and MXene/Fe$_2$O$_3$ as the negative electrode revealed energy density of 1.61 mW h cm^{-3} at power density of 459.47 mW cm^{-3}.[182]

In addition to using aqueous or solid-state electrolytes, metal-ion containing organic electrolytes (Li, Zn, Na, K, *etc.*) can be used for asymmetric SCs to gain a high operating voltage window as the metal ions can reversibly interact with MXene and store pseudocapacitance in organic electrolytes. Yu *et al.*[183] developed an asymmetric Li-ion capacitor using $Ti_3C_2T_x$/CNT as the anode and AC as the cathode in a LiPF$_6$/EC/DEC/DMC electrolyte. The device worked within a wide voltage range of 0.05–3 V and exhibited an energy density of 67 W h kg^{-1} and good capacity

This journal is © The Royal Society of Chemistry 2022

J. Mater. Chem. A, 2022, **10**, 1105–1149 | **1125**

retention of over 5000 cycles. Li-ion capacitors also assembled using conversion-type anode material-Sn(IV)@Ti$_3$C$_2$T$_x$ anode and AC cathode demonstrated significantly high energy density of 239.50 W h kg^{-1} at 10.8 kW kg^{-1}.[183] The performance of MXenes in Na-ion capacitor was also explored. When the Ti$_3$C$_2$T$_x$ anode was coupled with an AC anode, the prepared asymmetric Na-ion capacitor operated within a high voltage range of 0.6–4 V and maintained a coulombic efficiency of 96.6% over 4000 cycles. The Na-ion full cell consisting of alluaudite Na$_2$Fe$_2$(SO$_4$)$_3$ as the positive electrode and Ti$_3$CT$_x$ as the negative electrode operated at a high voltage of 2.4 V and exhibited 90 mA h g^{-1} at 1.0 A g^{-1}, respectively.[184] Moreover, the application of MXene in Zn-ion capacitor (ZIC) was also investigated. A ZIC consisting of MnO$_2$ as the cathode and Ti$_3$C$_2$T$_x$ as the anode works in a relatively high voltage window of 1.9 V and delivers an energy density of 90 W h kg^{-1} and power density of 3838 W kg^{-1}.[185] Wang et al.[186] developed a Ti$_3$CT$_x$–rGO aerogel cathode and Zn foil anode for Zn-ion hybrid SCs (ZHSC) for the first time. The ZHSC demonstrates a specific capacitance of 128.6 F g^{-1} at 0.4 A g^{-1} and an energy density of 34.9 W h kg^{-1} at a power density of 279.9 W kg^{-1}, and more importantly, with 95% capacitance retention over 75 000 cycles. MXene-based asymmetric SCs, especially metal-ion capacitors, deliver a wide operating voltage window and considerably impressive performance.

4.1.3 MXene-based micro-supercapacitor devices. The current miniaturization of electronic devices and smart autonomous systems requires the development of on-chip storage technologies such as MSCs with high energy and power densities for various applications. Symmetric and asymmetric MXene-based MSC devices can be designed with low power utilization owing to their high capacitance and the ease of processing MXenes. Till date, various techniques have been developed to fabricate MXene-based MSC devices on a small scale. Typically, traditional spray coating, printing, stamping, and vacuum filtration techniques are used for the preparation of MSC electrodes. The printed MSC exhibits an areal capacitance of 34.6 mF cm^{-2} at a scan rate of 1 mV s^{-1} and capacity retention of 91% after 15 000 cycles. The asymmetric MSC fabricated with Ti$_3$C$_2$T$_x$ and rGO on polyethylene terephthalate (PET) substrate operates in a voltage window of 1 V, maintains 97% initial capacitance after 10 000 cycles, and delivers 8.6 mW h cm^{-3} energy density at 0.2 W cm^{-3} with superior mechanical flexibility in PVA/H$_2$SO$_4$ gel electrolyte (Fig. 16d).[187] Yue et al.[188] constructed a self-healable 3D MSC by printing Ti$_3$C$_2$T$_x$–rGO composite aerogel electrode by wrapping polyurethane over it as an outer shell (Fig. 17a). Further, asymmetric MSCs constructed with polymer-MXene and MnO$_2$ electrodes work in a large potential window of 1.6 V and delivers an energy
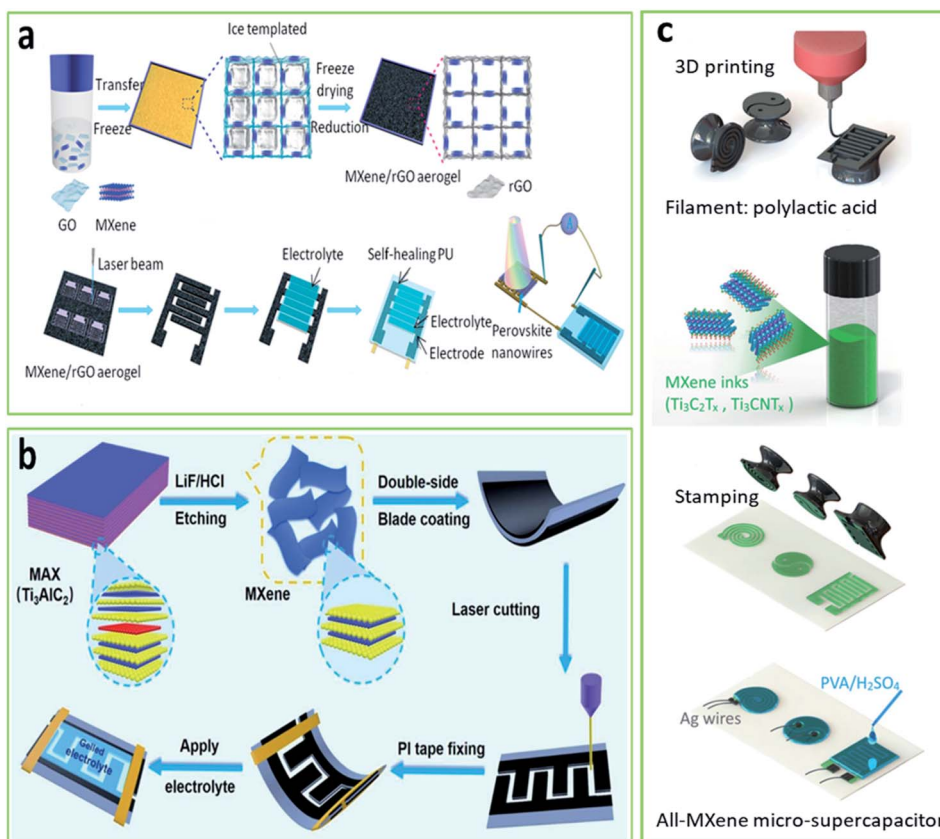
Fig. 17 (a) Schematic illustration showing the fabrication process of MXene-based micro-SC (MSC); (b) schematic for the fabrication process of double-side MSCs; (c) stamping strategy for fabrication of all-MXene-based MSCs. (a) Is adapted with the permission.[188] Copyright 2018, American Chemical Society. (b) Is adapted with the permission.[191] Copyright 2019, Wiley-VCH. (c) Is adapted with the permission.[192] Copyright 2018, Wiley-VCH.

1126 | *J. Mater. Chem. A*, 2022, **10**, 1105–1149

This journal is © The Royal Society of Chemistry 2022

Fig. 18 (a) Textile fabric attained by twisting or knitting fibers and photograph of the device as well as the lighting up of a light-emitting diode; (b) seamlessly knitted cellulose-based MXene-coated yarns; (c) schematic representations of energy textile prototype yarn SC device; (d) wearable Ti_3C_2 nanosheet (NS)/1T WS_2 NS fiber-shaped asymmetric SC device for a biomonitoring system. (a) Is adapted with the permission.[197] Copyright 2017, WILEY-VCH. (b) Is adapted with the permission.[198] Copyright 2019, WILEY-VCH. (c) Is adapted with the permission.[201] Copyright 2018, WILEY-VCH. (d) Is adapted with the permission.[202] Copyright 2020, WILEY-VCH.

density of 250.1 mW h cm^{-3} and power density of 32.9 W cm^{-3}.[189] Inkjet printing is another technique used for the printing of MSC electrodes with a high degree of digital patterning and geometrical flexibility. The organic solvent used as the dispersant of MXene inks promotes fast evaporation of the solvent, which helps to achieve high printing resolution and efficiency. Therefore, additive-free MXene inks are suitable for the direct printing of MSCs. The MSC printed with this technique shows high volumetric capacitance and energy density.[190] The laser cutting technique has also been used to fabricate MXene-based flexible MSCs and has achieved high areal capacitance (Fig. 17b).[191] Moreover, stamping method can also be used, which is also a cost-effective and time-consuming fabrication method when compared to inkjet and 3D printing techniques. Stamps in any shape can be 3D printed by computer-aided design, and then MXene ink is brushed on a substrate. The solid-state $Ti_3C_2T_x$ MSC prepared using the stamping method delivers a high area capacitance of 61 mF cm^{-2} and superior cycling stability (Fig. 17c).[192] MXene-on-paper coplanar electrodes are significantly promising for flexible on-paper MSCs. Various MSC devices have been fabricated using laser machining to develop $Ti_3C_2T_x$ paper electrodes.[193] Huang et al.[194] proposed a freezing-and-thawing approach to exfoliate multilayer MXenes with numerous wrinkles for on-chip MSCs. The as-assembled MSC showed high areal and volumetric capacitances of 23.6 and 591 F cm^{-3}, respectively. The in-plane flexible solid-state interdigitated MSC constructed

using freestanding $Ti_3C_2T_x$ electrodes shows a high areal capacitance of 340 mF cm^{-2} and a high volumetric capacitance of 183 F cm^{-3} at a current density of 0.25 mA cm^{-2}.[195]

MSCs are promising energy storage devices for miniaturized electronics. As discussed above, MXene-based MSCs can be fabricated using various techniques owing to their easy synthesis procedure and good mechanical strength. MXene MSCs exhibit excellent electrochemical performance with high volumetric capacitance and superior energy and power densities. Until now, the development of MXene MSCs is still in its early stages, and more versatile development into material advancement, electrolytes, and device optimization must be thoroughly considered.
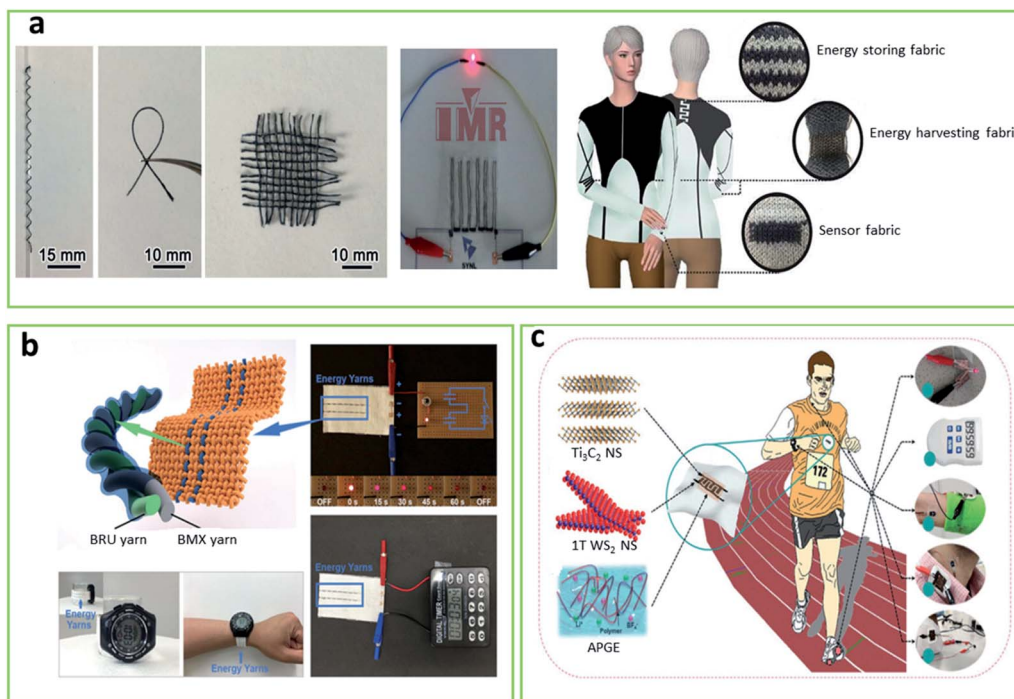
4.1.4 MXene-based transparent/yarn supercapacitor devices. In addition to the various promising properties of MXenes, such as its superior conductivity and hydrophilic nature, MXenes possess outstanding optical properties, which make them useful for the fabrication of transparent electrodes for various applications. MXene-based transparent electrodes were fabricated on PET substrates or conventional indium-doped tin oxide or fluorine-doped tin oxide substrates. Zhang et al.[196] prepared transparent and conductive $Ti_3C_2T_x$ films by spin casting followed by vacuum annealing for transparent solid-state SCs. Symmetric SCs show a high volumetric capacitance of 676 F cm^{-1} with a transmittance of 80%. Asymmetric SCs with a transmittance of 72% were also constructed based on $Ti_3C_2T_x$ and single-walled CNT transparent electrodes. The

This journal is © The Royal Society of Chemistry 2022

J. Mater. Chem. A, 2022, 10, 1105–1149 | 1127

Table 1 Electrochemical performance of MXenes and two-dimensional materials in supercapacitors

Electrode	Electrolyte	Capacitance	Stability	Ref
$Ti_3C_2T_x$	3 M H_2SO_4	208 F g^{-1}	64% after 10 000 cycles	203
$Ti_3C_2T_x$	3 M KOH	246.9 F g^{-1}	96.7% after 5000 cycles	204
Ta_4C_3T	PVA/H_3PO_4	194 F g^{-1}	90% after 10 000 cycles	205
$Ti_3C_2T_x$–rGO	1 M H_2SO_4	276 F g^{-1}	—	206
$Ti_3C_2T_x$–rGO	3 M H_2SO_4	386 F g^{-1}	—	207
V_2C	1 M H_2SO_4	487 F g^{-1}	83% after 10 000 cycles	208
TiC	3 M KOH	276.1 F g^{-1}	94% after 1000 cycles	209
PANI/V_2C	1 M H_2SO_4	337.5 F g^{-1}	—	210
Mo_2CT_x	1 M H_2SO_4	700 F cm^{-3}	—	211
$Ti_3C_2T_x$–polyindole	1 M KOH	226.5 F g^{-1}	90.5% after 8000 cycles	212
MoS_2–$Ti_3C_2T_x$	1 M H_2SO_4	303.8 F g^{-1}	82% after 10 000 cycles	213
Mesoporous carbon/$Ti_3C_2T_x$	6 M KOH	247 F g^{-1}	96.9% after 10 000 cycles	214
$Ti_3C_2T_x$–MCNT	0.5 M Na_2SO_4	1.93 F cm^{-2}	—	215
$Ti_3C_2T_x$–CNT	0.5 M Na_2SO_4	2.26 F cm^{-2}	—	216
MoO_{3-x}–Ti_3C_2	5 M LiCl	631 F cm^{-3}	103.9% after 10 000 cycles	217
$Ti_3C_2T_x$/$CuCo_2S_4$	6 M KOH	992.3C g^{-1}	91.2% after 10 000 cycles	218
MXene-CNT/PANI	1 M H_2SO_4	429.4	93% after 10 000 cycles	219
MoS_2–Mo_2N	1 M Na_2SO_4	351.62 F g^{-1}	93.62 after 10 000 cycles	220
Co_3S_4/CoS/MoS_2	3 M KOH	805.7 F g^{-1}	91.2% after 10 000 cycles	221
NiS_2/MoS_2	2 M KOH	951C g^{-1}	—	222
Ni-Co_4N@NC	2 M KOH	397.5 mA h g^{-1}	93% after 10 000 cycles	223
MoS_2/Ti_3C_2	1 M H_2SO_4	386.7 F g^{-1}	96.8% after 20 000 cycles	173
VS_2/MWCNTs	0.5 M KCl	830 F g^{-1}	95.9% after 10 000 cycles	224
WS_2/carbon	1 M H_2SO_4	248.7 F g^{-1}	100% after 4000 cycles	225
Cu_3N/Ni_3N	1 M KOH	390.5 mA h g^{-1}	94.9% after 10 000 cycles	226
Mo_2N/rGO	1 M H_2SO_4	142 mF cm^{-2}	—	218
VN	1 M KOH	1340 F g^{-1}	—	227
Nb_4N_5	1 M H_2SO_4	225.8 mF cm^{-2}	70.9% after 2000 cycles	228
TiN/VN	1 M KOH	247.5 F g^{-1}	88% after 500 cycles	229
W_2N	1 M H_2SO_4	163 F g^{-1}	95.45% after 10 000 cycles	230
CoN-Ni_3N/N-C	1 M LiOH	1.2 F cm^{-2}	93.3% after 10 000 cycles	231

asymmetric SCs display significantly high capacitance and energy density without capacitance loss for over 20 000 cycles. Furthermore, with the current advancement in miniaturized and wearable electronic devices, the demand for compatible power sources has increased. Yarn SCs are more attractive for wearable devices and textiles because they are more conformal and can be easily integrated into miniaturized devices. Flexible all-solid-state $Ti_3C_2T_x$ fiber-based SCs are fabricated using commercial silver-plated nylon fibers. The MXene-coated fibers are considerably flexible and can be twined and bent into complex shapes and woven into a textile structure (Fig. 18a). The PVA–H_2SO_4 hydrogel is used as the electrolyte to assemble SC devices. The prepared SCs showed an area capacitance of 328 mF cm^{-2} and 80% capacitance retention under different deformation modes.[197] Knittable and washable multifunctional MXene-coated cellulose yarns were fabricated by Uzun et al. (Fig. 18b)[198] Recent reports have shown that MXene-based fibers can achieve a high volumetric capacitance of ~341 F cm^{-3}, which is one order of magnitude greater than that of the graphene fiber.[199] Zhang et al.[200] developed $Ti_3C_2T_x$-based yarn SCs that demonstrated superior performance under different mechanical deformations. Wang et al. employed a biscrolling strategy to create flexible MXene/CNT yarns trapped within helical yarn corridors. The as-developed MXene/CNT and RuO_2 asymmetric yarn SCs demonstrated energy and power densities

of 61.6 mW h cm^{-3} and 5428 mW cm^{-3}, respectively (Fig. 18c).[201] The asymmetric SCs fabricated with $Ti_3C_2T_x$ and 1T-phase WS_2 on a polyester/cellulose blend cloth substrate exhibited superior performance, good flexibility, and wearability, and could be integrated into multiple units and shapes (Fig. 18d).[202] These reports demonstrate the considerable potential of MXenes for SC devices. The electrochemical performance of some of the recently reported MXenes and 2D materials for SCs is listed in Table 1.

4.2 MXenes and their derivatives for batteries

In recent years, as the market for high-performance batteries, such as those used in electric vehicles, has become more competitive, the need for next-generation LIBs has surged.[232,233] However, owing to the restricted capacity of graphite anode materials, there is a growing interest in alternate anode materials despite their superior properties.[234] MXene material is a next-generation electrode material in this circumstance, and numerous investigations are being conducted because of its superior properties.[235,236] MXene material has received increased attention, mostly as an SC material, although numerous research studies have been published that considered it as a battery material as well.[109,237] Research on MXene-based LIBs, which was first published in 2012, has continued to grow every year since then, as shown in Fig. 19 (2012,[31,238]

1128 | J. Mater. Chem. A, 2022, 10, 1105–1149

This journal is © The Royal Society of Chemistry 2022
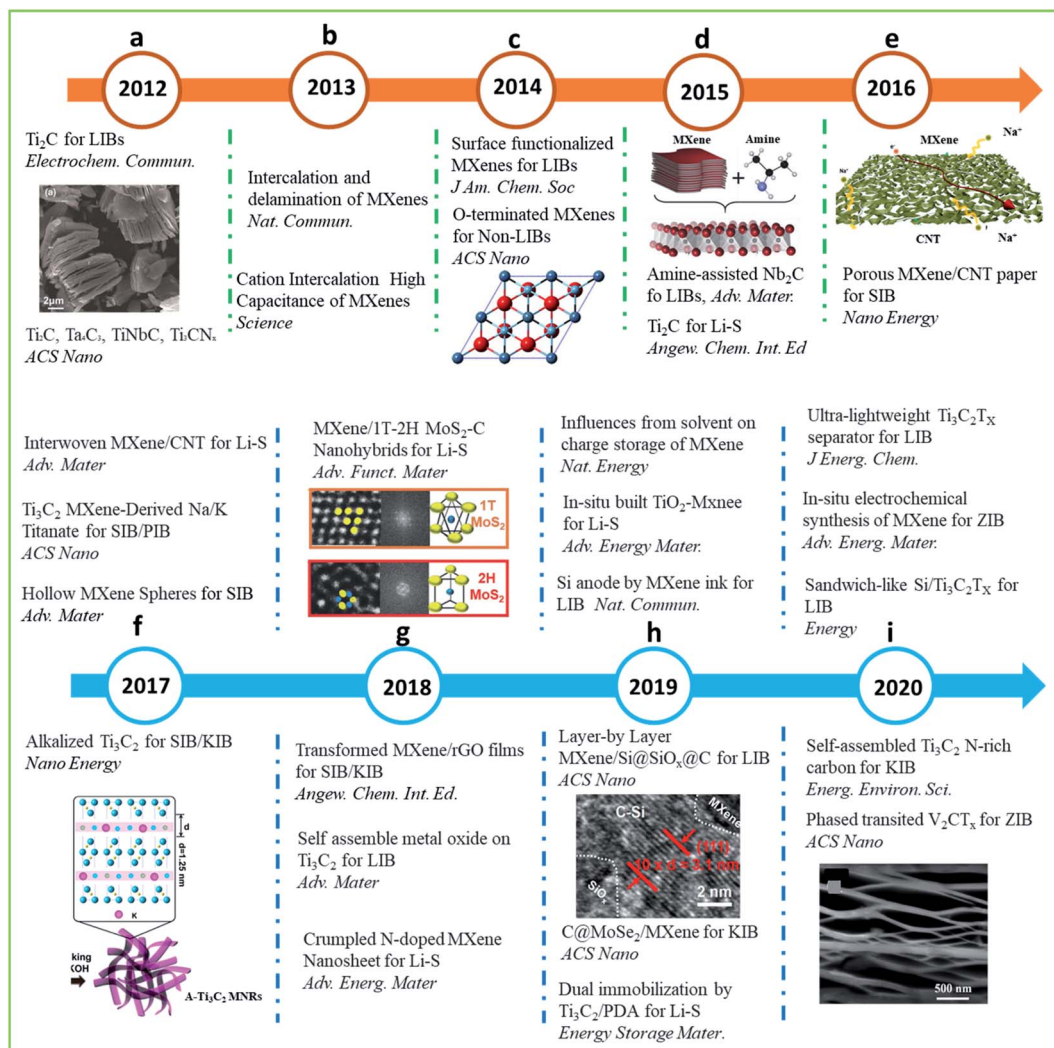
Fig. 19 Timeline of the research progress related to MXene-based metal-ion batteries in the years 2012–2020. (a) Is adapted with permission.[238] Copyright 2012, Elsevier. (c) Is adapted with permission.[239] Copyright 2014, American Chemical Society. (d) Is adapted with permission.[52] Copyright 2015, WILEY-VCH. (e) Is adapted with permission. (e) Is adapted with permission.[242] Copyright 2016, Elsevier. (f) Is adapted with permission.[233] Copyright 2017, Elsevier. (g) Is adapted with permission.[247] Copyright 2018, WILEY-VCH. (h) Is adapted with permission.[255] Copyright 2020, (i) is adapted with permission.[256] Copyright 2020, American Chemical Society.

2013,[51,91,139] 2014,[239,240] 2015,[52,241] 2016,[242] 2017,[233,243–245] 2018,[246–249] 2019,[250–255] and 2020.[90,256–259]). MXene materials are used in a wide range of batteries, including LIBs and Zn-ion batteries (ZIBs).[260] The electrochemical performance of the MXene based battery electrodes are included in Table 2. Aside from being an active material, it also serves other functions such as a conducive binder or synthesizing template.[261] MXene materials are known to exhibit an intercalation reaction with Li ions, similar to graphite anodes.[237,262] Owing to its comparatively wide interlayer distance when compared to graphite, it demonstrates greater potential as a negative electrode material.[261,263]

4.2.1 MXenes for Li-Ion batteries. Owing to its low cost, high stability, and strong electrical conductivity, graphite is the most widely utilized anode material for LIBs. However, the specific capacity of the graphite anode is limited owing to the Li-

ion intercalation process.[264] Naguib et al.[238] designed 2D Ti$_2$C anodes for LIBs in 2012. TiO$_2$ cyclic voltammetry (CV) curves are similar to TiO$_2$ CV curves, showing that the Ti$_2$C surface was likely transformed to Ti$_2$CO$_X$ during titanate reactions, as shown by the broad redox peaks at 1.6 and 2.0 V (*versus* Li$^+$/Li). The exfoliated Ti$_2$C displays a reversible capacity of 225 mA h g^{-1} at 0.04C and 80 mA h g^{-1} at 3C. Since this study was published, MXenes and MXene-based composite electrodes have been the subject of several studies to improve the electrochemical performance of MXene-based LIBs. The proposed reaction mechanism is described as follows.

$$Ti_2CO_x + yLi^+ + ye^- \leftrightarrow Li_yTi_2CO_x \qquad (9)$$
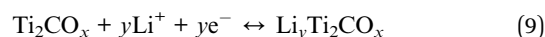
Electrostatic processes may effectively embed metal cations onto the surface of alkaline MXene.[265] For high-performance MXene anodes in LIBs, a metal cation composite might be

Table 2 Electrochemical battery performance of different electrodes

Material	Application	Capacity (mA h g^{-1})	Current density (A g^{-1})	Cycle number (retention)	Ref
BPE@V$_2$CT$_x$	KIBs	593.6	0.1	3000 (91%)	339
Ti$_3$C$_2$T$_x$/MoS$_2$	KIBs	290.7	0.05	100 (75.9%)	338
NG/ReSe$_2$/Ti$_3$C$_2$	KIBs	395.3	0.1	300 (61%)	340
PDDA-NPCN/Ti$_3$C$_2$	KIBs	499.8	0.1	300 (61.4%)	258
K@DN-MXene//S	K-metal batteries	331	0.1C	500 (69.4%)	341
TiO$_x$N$_y$/C	KIBs	765	0.1	1200 (22.8%)	336
MoSe$_2$/Ti$_3$C$_2$T$_x$@C	KIBs	355	0.2	300 (100%)	252
Ti$_3$C$_2$T$_x$/Sb	KIBs	516	0.05	500 (79.1%)	342
KTO/rGO	KIBs	228	0.1	—	249
a-Ti$_3$C$_2$	KIBs	136	0.02	500 (79.2%)	233
M-KTO	KIBs	151	0.05	500 (61%)	245
Ti$_3$CNT$_z$	KIBs	202	0.05	100 (27.2%)	235
Hf$_3$C$_2$T$_x$	LIB	146	0.2	200	39
Mo$_2$TiC$_2$T$_x$	LIB	176	1C	160 (82%)	44
Mo$_2$CT$_x$	LIB	560	0.4	1000	56
Nb$_2$CT$_X$	LIB	170	1C	100	276
Nb$_2$CT$_X$	LIB	110	10C	150	276
(Nb$_{(0.8)}$,Ti$_{(0.2)}$)$_4$C$_3$T$_x$	LIB	158	20.2 mV s^{-1}	20	343
TiO$_2$/Ti$_2$CT$_X$	LIB	389	0.1	50	268
CoNi@NCNTs	Li–S batteries	676.8	1	500	344
V-MoS$_2$	SIBs	548.1	0.1	800	345
MoS$_2$	SIBs	467	0.1	100	346
NaTi$_{1.5}$O$_{8.3}$	SIBs	101	2	150 (135%)	245
K$_2$Ti$_4$O$_9$	KIBs	81	0.3	900 (45%)	245
Na$_{0.23}$TiO$_2$/Ti$_3$C$_2$	SIBs	47	3	4000 (56%)	278
CoS$_2$/CNTs/TiO$_x$N$_y$	SIBs	166	2	100 (72%)	347
PVP Sn(iv)@Ti$_3$C$_2$	LIBs	851	0.1	50 (74.6%)	267
V$_2$CT$_x$-Ca MXene	LIBs	514.6	0.5C	200 (97%)	348
Li-Nb$_2$-CT$_x$-400	LIBs	456	2	50 (75%)	349
SiO$_2$/MXene	LIBs	798	0.2	100 (97%)	350
PDDA-NPCN/Ti$_3$C$_2$	KIBs	583.7	0.1	300 (61%)	258
MoS$_2$/MXene	KIBs	271.4	0.05	100 (75.9%)	351
a-Ti$_3$C$_2$MNRs	KIBs	78	0.2	500 (53%)	233
Bi$_2$S$_3$/MXene	SIBs	281	0.5	250 (55%)	352
CoS/MXene	SIBs	304	2	1700 (87.8%)	353
V$_2$CTx	SIBs	470	2.5C	1000 (56.8%)	243

a viable option.[232,238,266] Luo et al.[267] reported Sn^{4+} ion-decorated Ti$_3$C$_2$ electrodes for LIBs with high volumetric capacities and long life cycles. The multiple effects of Sn^{4+} ions on MXene electrodes include providing an active site for electrochemical reactions, increasing electronic conductivity, and inhibiting volume expansion during lithiation. They produced Sn^{4+}-decorated MXene by simple liquid-phase immersion through electrostatic and ion-exchange processes (Fig. 20a and b). A cation in an electrolyte, such as Li$^+$ or Na$^+$, has been reported to intercalate into MXene layers during the charging process. As a result of the increased interlayer distance, the pre-intercalation of Sn^{4+} ions can improve the electrochemical performance of MXene electrodes. The reversible capacity of Sn^{4+}@Ti$_3$C$_2$ after the fiftieth cycle of 1374.8 mA h cm^{-3} is higher than that of pristine Ti$_3$C$_2$ (197 mA h cm^{-3}) and graphite (550 mA h cm^{-3}) with 94.3% capacity retention over 200 cycles. Generally, MXene materials can act as active sites for charge storage, buffer layers for volume expansion, and conductive agents. The enhanced electrochemical performance indicates that MXene materials are promising anodes for LIBs owing to their multiple effects.

It is also possible to increase the electrochemical performance by treating the MXene LIB anode with H$_2$O$_2$. The MXene interlayer distance could be induced, and TiO$_2$ nanocrystals can be formed on the MXene surface. Ahmed et. al.[268] developed H$_2$O$_2$-assisted Ti$_2$C MXene electrodes for LIBs. The functional groups on the surface of MXene, such as –OH, –F, and –O– from acidic etchants can change the properties of MXene, such as the bandgap and electrochemical performance. The (0002) peak of the Ti$_2$AlC MAX phase was shifted to a lower angle, indicating an increase in the interlayer distance and removal of Al (Fig. 20d). The H$_2$O$_2$-treated Ti$_2$C shows high reversible capacities at the second cycle of 507, 429, and 384 mA h g^{-1} at current densities of 100, 500, and 1000 mA g^{-1}, respectively. As shown in Fig. 20f, H$_2$O$_2$-treated MXene shows superior rate capability and long-term cycle stability under a high current density of 5000 mA g^{-1}.

In addition, the use of a 3D-structured MXene electrode may be a viable method to enhance the energy density of the material. To create a 3D structure with MXene, an optimized synthesis method should be developed, such as the templated method.[243,269–273] Zhao et. al.[274] reported a S-template method to
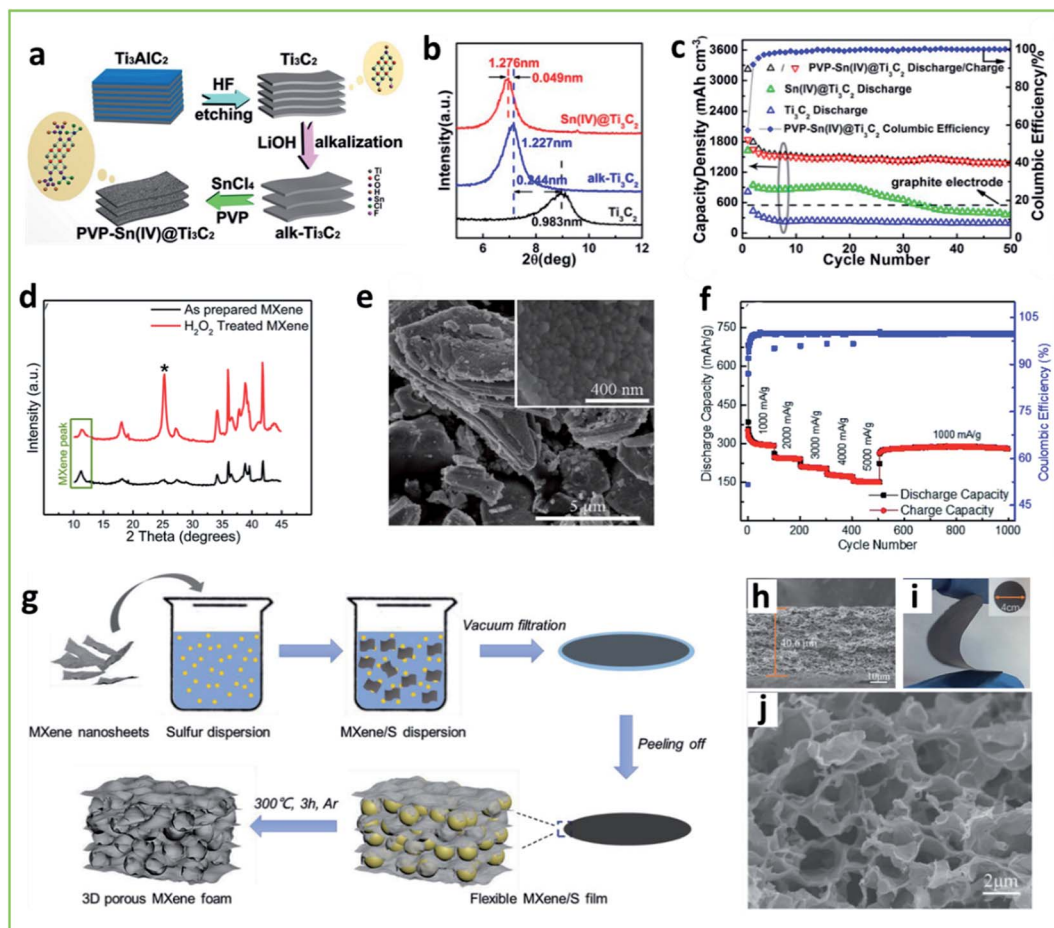
1130 | J. Mater. Chem. A, 2022, **10**, 1105–1149

This journal is © The Royal Society of Chemistry 2022

Fig. 20 (a) Schematic process of Sn^{4+} ion-decorated Ti_3C_2 MXene; (b) XRD patterns of pristine Ti_3C_2 and Sn^{4+}-decorated Ti_3C_2; (c) electrochemical performance of $Sn^{4+}@Ti_3C_2$; (d) XRD spectra of H_2O_2 treated MXene; (e) SEM image of H_2O_2-treated MXene; (f) rate capability test of H_2O_2-MXene at various current densities; (g) schematic illustration of experimental step of flexible 3D MXene foam; (h) SEM image; (i) digital photo of 3D MXene foam; (j) high-resolution SEM image of 3D MXene foam. (a–c) are adapted with permission.[267] Copyright 2016, American Chemical Society. (d–f) Are adapted with permission.[268] Copyright 2016, The Royal Society of Chemistry. (g–j) Are adapted with permission.[274] Copyright 2019, WILEY-VCH.

create 3D foam of MXene from 2D nanosheets. As shown in Fig. 20g, they prepared a MXene-S composite, which was vacuum filtered to form freestanding films. They used polyvinyl pyrrolidone (PVP) as a dispersion agent, which performs a critical role in preventing the aggregation of S particles and enhancing the reaction between S and MXene (Fig. 20h and i). The high-thickness MXene foam has a low packing density of 2.3 g cm^{-3} than that of conventional vacuum-filtrated MXene film (0.65 g cm^{-3}). The 3D MXene foam shows a high initial reversible capacity of 455.5 mA h g^{-1} with a 65.5% ICE. However, pristine MXene films show low reversible capacity of 35.4 mA h g^{-1}. The 3D MXene also exhibited superior rate capabilities of 215.6, 187.4, 133.3, 112.5, and 101 mA h g^{-1} at current densities of 1, 2, 10, 15, and 18 A g^{-1}, respectively, with good long-term cycle stability of up to 3500 cycles.

While finetuning its properties, the performance may be tuned by varying the composition of the M elements, C and/ or N, and/or the terminations T (–O, –OH, and –F) in the MXene.[275] MXenes differ in particular capacity according to the

sequence Ti_2C, Nb_2C, V_2C, with both Nb_2C and V_2C exhibiting high-rate capability.[276] In addition, the voltage profiles of different MXenes vary considerably, indicating the applicability of different MXenes as anode or cathode materials. Furthermore, the surface terminations of MXenes influence the Li uptake capacity and transport. Moreover, nonnative termination groups of MXene, such as chlorides, can increase the interlayer space and mitigate the negative effects of the native OH and F functional groups.[92] There are several factors that can impact the LIB capacity, including differences in stoichiometric ratios of "M" within the same species, as well as differences in manufacturing processes. For example, Ti_2CT_X has a lower c-lattice parameter than $Ti_3C_2T_X$ with a higher surface energy, thereby hindering the intercalation of Li ions. Instead of using MXene as an anode material for LIBs because of its theoretical capacity, a better alternative is to use MXene-based nanostructured electrodes for Li–S batteries, which can achieve a specific capacity of up to 1675 mA h g^{-1} and high energy owing to the chemistry between Li and S.[277] However, as a result of the

This journal is © The Royal Society of Chemistry 2022

J. Mater. Chem. A, 2022, 10, 1105–1149 | 1131

polysulfide shuttling action, the capacity rapidly degrades. Polysulfide-anchoring materials have been shown to be useful in easing this problem, both theoretically and experimentally.

The self-assembly of TMO nanostructures on MXene for rapid Li storage was described by Liu et al.[248] Heterostructures consisting of SnO_2 nanowires and a TiO_2/MXene nanorod were created using a straightforward technique. Ti_3C_2-MXene acts as an underlying substrate, enabling reversible electron and ion transport at the interface and preventing the formation of TMO during the lithiation/delithiation process. On the outer side, TMO acted as a spacer to prevent the restacking of MXene nanosheets. Specific capacities of 272 mA h g^{-1} at a current density of 50 mA g^{-1} and 720 mA h g^{-1} at 100 mA g^{-1} were reported for the TiO_2/MXene and SnO_2/MXene heterostructures, respectively. Huang et al.[278] reported sandwich-like $Na_{0.23}TiO_2$ nanobelt/Ti_3C_2-MXene composites for LIBs/SIBs. The $Na_{0.23}TiO_2$ nanobelt/Ti_3C_2-MXene composite was synthesized through an in situ transformation process in which oxidation was performed in the presence of NaOH. It was observed that the interlayer spacing of Ti_3C_2 MXenes increased in the composite with $Na_{0.23}TiO_2$ nanobelts, which was confirmed by the shift in the (002) peak from 8.8° to 6.9°. With the use of this composite electrode in LIBs/SIBs, an excellent cycling stability of 100% was achieved over 4000 cycles. Shang et al.[279] synthesized 2D $GeO_x(x = 1.57)$@MXene composite using a wet-chemical process and used it as an anode material for LIBs. This battery showed fast charge/discharge performance of 3 min at 20.0C owing to the enhanced e^{-}/Li^{+} conductivity based on the metallic properties of Ge and MXenes. The half-cell battery showed a capacity retention of 86.9% after 500 cycles with an initial capacity of 1206.3 mA h g^{-1} with a coulombic efficiency of 91.5%.

In conclusion, the performance of LIBs based on MXene-based electrodes relies on the different factors and properties of the electrode materials and electrolytes. The electrochemical performance can be tuned by surface decoration, group grafting, and adjustment of the composition. Hence, the rational nanoengineering of electrode materials based on MXenes will support their application in LIBs. However, only a few MXenes are synthesized with certain metals; thus, alteration of the composition such as metal/carbon ratios and metal species will predominantly affect the performance of LIBs. Furthermore, the surface terminations and interlayer distances of the prepared MXenes influence the performance of LIBs. Composites with metal oxides and silicon might be a possible way to improve the performance of LIBs.

4.2.2 MXenes for Na-ion batteries. The growth of the market for LIBs is driving up the cost of raw materials.[260] This has resulted in a huge growth in the demand for batteries that are both inexpensive and efficient.[280,281] There is an ever-increasing need for innovative low-cost energy storage technologies, namely high-capacity batteries that require relatively significant amounts of raw materials.[282–284] Na, which is an earth-abundant, evenly distributed element, is receiving significant attention as a next-generation battery material for large-scale batteries.[285,286] As it is an alkali metal similar to Li and relatively inexpensive, it is possible to manufacture

batteries using a structure similar to conventional LIBs.[287–289] Therefore, several researchers have developed SIBs based on their research experience in LIBs because they thought that SIBs could be developed using similar synthesis methods as conventional LIBs.[290,291] However, several investigations have revealed significant variations in electrochemical behavior between Li and Na, and the general consensus currently is that applying electrodes from LIBs to SIBs is problematic.[292–294] Particularly, as there are no candidates so far who show the best characteristics of the anode material of the SIBs, the study of various materials is being actively conducted.[295–297]

The difficulty in developing anode materials for SIBs is that, graphite which performs well in LIBs, performs poorly with Na ions.[285,298,299] The reason for this low performance of graphite is the large ionic radius of Na ions. This was identified in the beginning of the study on SIB anodes and was later reported to be a thermodynamic problem caused by a low binding force between Na ions and the graphite surface.[300–302] Under these circumstances, carbon-based SIB anode materials that are primarily based on hard carbon were considered, and several successful studies have been reported.[269,303,304] In the development of high-performance SIB anodes, MXene materials have attracted significant attention because they can perform well as anode materials.[305–307] The computational results indicated low diffusion barriers with Na^{+} ions, which are related to MXene-based electrodes (Fig. 21).[99,308] $Ti_3C_2T_X$ displays Na^{+} ion intercalation as a two-phase reaction and solid–solution reaction. Furthermore, DFT calculations indicate that MXenes have good intercalation characteristics with horizontal sliding into Ti_3C_2X layers. This computational study shows that the Na^{+} ions can smoothly intercalate into MXene layers and demonstrates the versatility of MXene materials.[237] The interlayer distance of Ti_2CT_X nanosheets was extended during the first sodiation phase, and this enhanced interlayer gap was maintained without substantial change during desodiation.

The absorption energies of alkali metals such as Li, Na, K, and Ca differ according to the coverage.[232,233,309] Based on the first-principles DFT calculations, a linear relationship between the effective ion radius and reversible capacity can be determined.[275] A larger effective ionic radius increases the reaction of alkali atoms and MXene electrodes.[310] Furthermore, the diffusion barrier is well known as an important factor for determining the battery electrode performance.[311] Fig. 22a–d show that optimized pathways of various alkali ions with Ti_3C_2 monolayer calculated by the nudged elastic band method with diffusion barrier profiles.[312] Li ions show a calculated diffusion barrier of 0.068 eV, but Na displays a value of 0.096 eV, which implies that Ti_3C_2 has a low diffusion barrier against alkali metal. This result shows the possibility of using MXene electrodes as high-rate electrodes. The Na-ion storage properties of Ti_3C_2 MXenes, such as capacity, mobility, and volume expansion during sodiation, as well as desodiation with interlayer-expanded electrodes, were investigated using the ab initio DFT method.[310,313,314] This computational study showed that interlayer-expanded MXenes have a low diffusion barrier energy against Na ions.[312] Moreover, the lattice parameter of expanded MXenes was marginally changed when compared to pristine
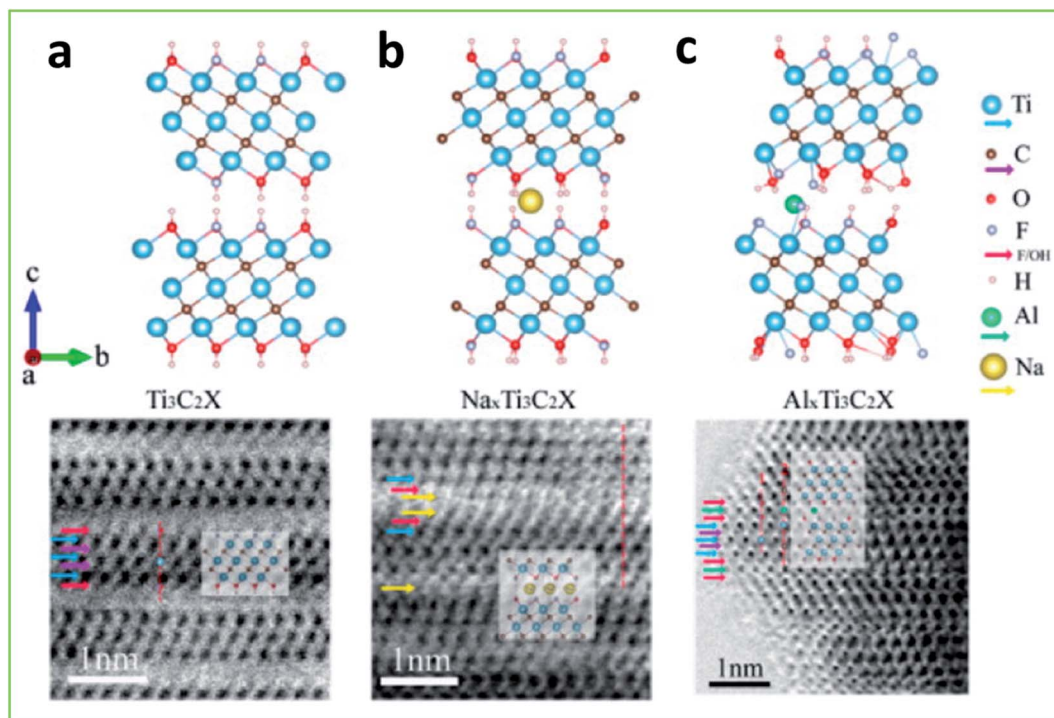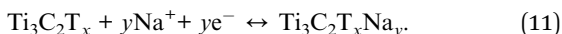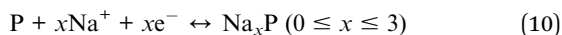
Fig. 21 (a–c) Optimized geometries of $Ti_3C_2T_X$, $Na_XTi_3C_2T_X$, and $Al_XTi_3C_2T_X$ from side and top views. (a) Is adapted with permission.[99] Copyright 2015, American Chemical Society.

MXenes. As shown in Fig. 22e–j, interlayer-expanded MXenes have the most favorable thermodynamic migration with Na ions than pristine MXenes. This result suggests that surface-treated MXenes demonstrate superior performance than pristine MXene electrodes. Recent studies on MXene-based SIB anodes have focused on surface-enhanced MXene electrodes.[315–320] A molecular-level PDDA-BP/Ti_3C_2 nanosheet heterostructure was reported with the synergistic effects of high capacity (BP) and abundant functional groups (Ti_3C_2).[312] The PDDA modification can enhance electronic conductivity and passivate BP from oxidization in water, resulting in improved cycle stability. PDDA-BP and Ti_3C_2 nanosheets were synthesized in face-to-face contact with a suitable interlayer distance to store Na ions. This parallel 2D structure can provide a low diffusion barrier and an effective channel, which enhances the electrochemical kinetics. The PDDA-BP/Ti_3C_2 heterostructure shows high reversible capacity of 112 mA h g^{-1} at 0.1 A g^{-1}. This heterostructure shows two distinct cathode peaks at the first sodiation steps at 1.0 and 0.45 V, which are related to the initial irreversible side reaction to form solid electrolyte interphase. The GCD profiles of the PDDA-BP/Ti_3C_2 electrode showed clear plateau regions at low potentials, which were due to the alloying reaction of BP. The possible reactions of the PDDA-BP/Ti_3C_2 electrode are as follows.

$$P + xNa^+ + xe^- \leftrightarrow Na_xP \ (0 \leq x \leq 3) \tag{10}$$

$$Ti_3C_2T_x + yNa^+ + ye^- \leftrightarrow Ti_3C_2T_xNa_y. \tag{11}$$

PDDA-BP/Ti_3C_2 exhibits superior rate capability of 43.4% of capacity retention when compared to high current density of 2.0–0.1 A g^{-1}. It also exhibits good long-term cycle stability, with only 0.05% capacity decay per cycle to 2000 cycles. The superior electrochemical performance was attributed to the strong interaction between BP and MXenes with lower binding energy and enhanced interfacial charge transfer due to the large interlayer distance of the heterostructure. It is an effective approach to prepare composites with carbon and MXenes for high-performance SIB anodes.[242,269,323–325] Usually, MXenes materials are easily exposed to severe problems such as restacking and aggregation.[87,326,327] To overcome this problem, several researchers have developed MXene-carbon composites.

Recently, Xu *et al.* reported 3D carbon-coated MXene architectures for ultrafast Na storage.[269] A simple approach was suggested for the direct synthesis of 3D carbon-coated MXene structures by transformation of 2D $T_3C_2T_x$ nanosheets by self-polymerization of dopamine, which was coated on the surface of MXenes, as shown in Fig. 23a. First, the MXene/dopamine mixture was prepared and self-polymerized to form a polydopamine layer on the MXene surface. A polymeric layer was formed, which facilitated the transformation of 2D nanosheets into a tremella-like 3D structure with a highly exposed active site and smaller overall surface energy. After carbonization under inert conditions, the polydopamine layer was converted into carbon, and this 3D carbon-coated structure can preserve the structural collapse and oxidation of MXene materials by air exposure. The SEM images of the 3D carbon-MXene composite exhibit a disordered structure with exposed facets, which confirms the effect of polydopamine on the structure. TEM

This journal is © The Royal Society of Chemistry 2022

J. Mater. Chem. A, 2022, **10**, 1105–1149 | **1133**
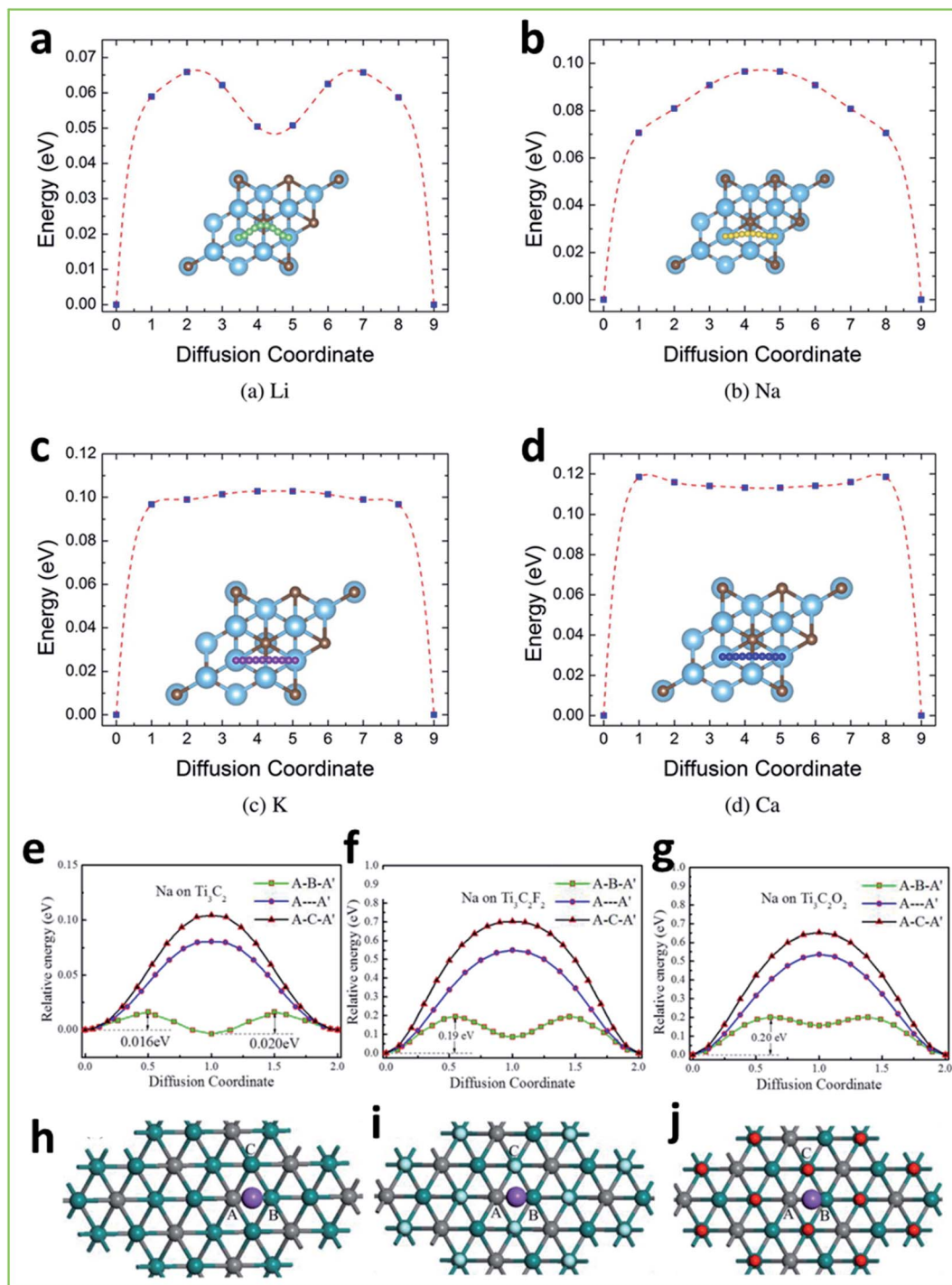
Fig. 22 (a–d) Schematic representation of the top view of the energetically optimized migration pathways and the corresponding diffusion barrier profiles of Li, Na, K, and Ca on Ti_3C_2 MXene, respectively, and (e–j) energy profiles of Na atom diffusion on a $3 \times 3 \times 1$ supercell of Ti_3C_2 and corresponding geometries. (a–d) Are adapted with permission.[321] Copyright 2014, American Chemical Society. (e–j) Are adapted with permission.[322] Copyright 2016, American Chemical Society.

images show the microscopic structure of the 3D carbon-MXene composite with surface facets and increased lattice interlayer space (Fig. 23b–d). This extended gap can facilitate the access of electrolyte ions to the active material and enhance the redox reaction and charge transportation. Finally, representative energy-dispersive X-ray spectrometry (EDS) mapping confirmed

the presence of $Ti_3C_2T_X$ MXenes in the 3D structure. This 3D carbon-MXene structure shows high capacity 257.6 mA h g^{-1} at a current density of 0.05 A g^{-1} and this capacity was retained even after 200 cycles. Furthermore, the 3D carbon-MXene structure exhibited good long-term cycle stability of 91.7% after 3000 continuous cycles at a high current density of 1 A g^{-1}.

1134 | J. Mater. Chem. A, 2022, **10**, 1105–1149

This journal is © The Royal Society of Chemistry 2022
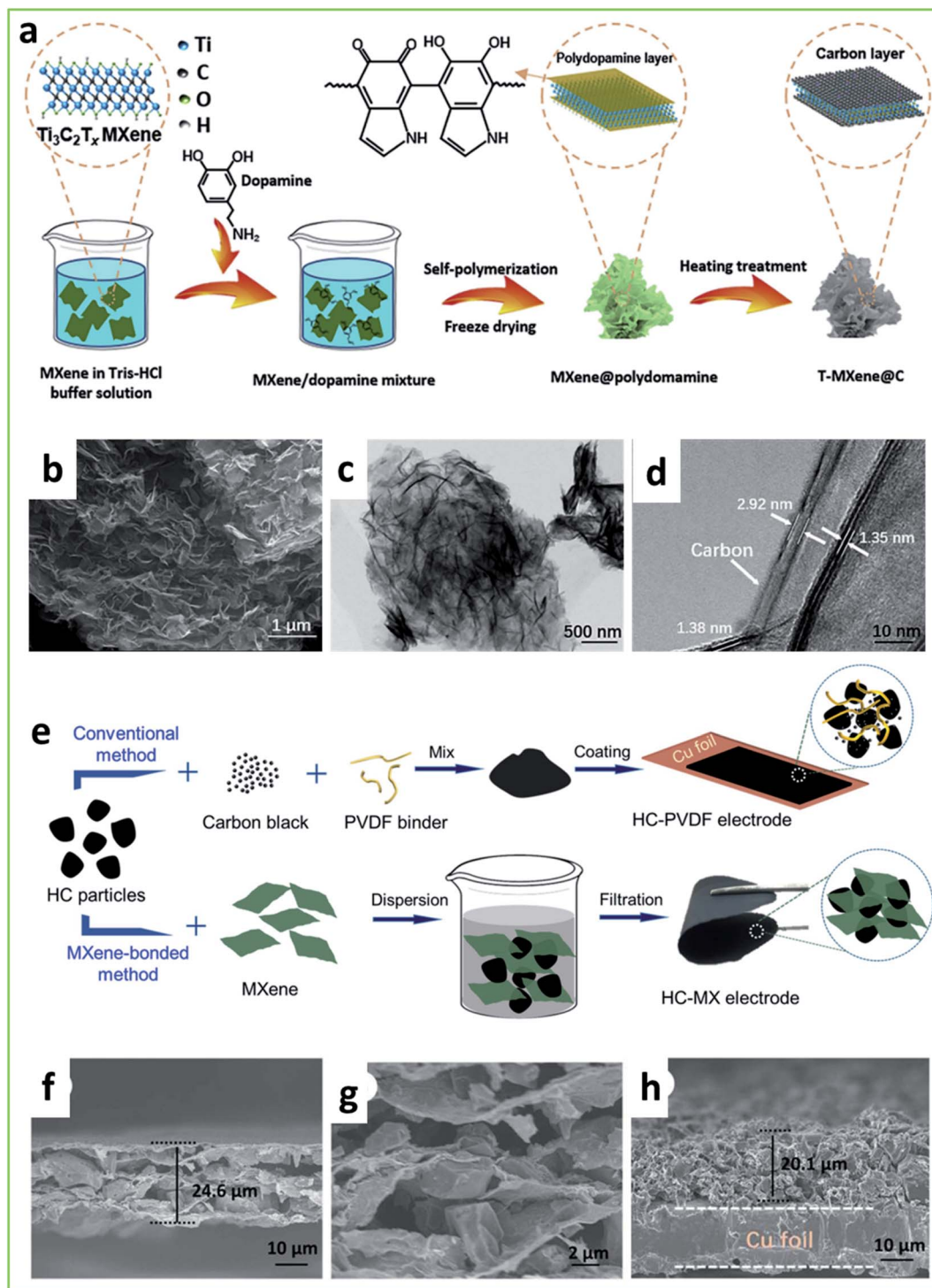
Fig. 23 (a) Schematic diagram generalizing the preparation of T-MXene@C; (b) SEM image, (c) low-magnification TEM, (d) high-magnification TEM, (e) schematic diagram showing the preparation of conventional polyvinylidene fluoride (PVDF)-bonded (top) and MXene-bonded hard carbon (HC) (bottom) electrodes. Using $Ti_3C_2T_x$ as a multifunctional binder, flexible and freestanding film electrodes are prepared without the need for electrochemically inactive additives, including conductive agent, PVDF binder, and copper current collector. (f–h) SEM images of MXene-bonded HC film (HC-MX-2:1) and conventional PVDF-bonded HC electrode coating on the Cu foil current collector. (a–d) Are adapted with permission.[269] Copy right 2020, Elsevier. (e–h) Are adapted with permission.[328] Copyright 2019, WILEY-VCH.

The effective strategy of the 3D carbon-MXene structure is a simple approach to prepare carbon-MXene structures to prevent layer restacking and air oxidation.

Another approach to prepare MXene-carbon composite electrodes for SIBs is by using MXene-bonded hard carbon films.[328] Hard carbon is a promising candidate for SIB anode

This journal is © The Royal Society of Chemistry 2022

J. Mater. Chem. A, 2022, 10, 1105–1149 | 1135

materials with high reversible capacity; however, it has severe problems such as large volume expansion during sodiation/desodiation.[329] These limit the performance of hard carbon anodes. Bin Xu *et al.*[328] reported a novel approach to overcome these limitations using MXene as a conductive binder. The MXene binder can reduce the necessity of electrochemically inactive components such as polyvinylidene fluoride binder and carbon conductive additives. MXene 2D nanosheets can construct a 3D network, which can enhance the electrochemical reaction and accommodate the volume expansion of active materials during sodiation/desodiation. The MXene-bonded flexible freestanding hard carbon electrode was prepared *via* facile one-step vacuum-assisted filtration of an aqueous suspension of hard carbon and $Ti_3C_2T_x$, as shown in Fig. 24e. The prepared film is flexible and freestanding; therefore, it is possible to fabricate SIB cells without a metal foil assistant. In contrast, a conventional electrode with a conductive additive and polymer binder was prepared using the slurry casting method for comparison. The SEM images in Fig. 23f–h shows the cross-section surface of the MXene-bonded hard carbon film with a 2 : 1 mass ratio. There are irregular hard carbon particles with micrometer-sized gap between the MXene nanosheets. In higher magnification images, it can be clearly observed that a 3D network structure is formed by the encapsulation of hard carbon particles by the MXene nanosheet. Hard carbon structure can act as "spacer" to prevent restacking of MXene layers. Moreover, MXene can accommodate the volume expansion of hard carbon using a 3D architecture. Based on the synergistic effect of hard carbon and MXene, the freestanding

film delivers a high reversible capacity of 368 mA h g^{-1} at 30 mA g^{-1} with superior long-term cycle stability and rate capability with Na ions.

Tang *et al.*[330] reported MXene-derived TiS_2 nanosheets for high-performance SIBs. The carbon-coated TiS_2 nanosheets were prepared using an *in situ* conversion process with PVP-modified $Ti_3C_2T_X$ (TiS_2@Cpvp). The SEM and TEM images of TiS_2@Cpvp show a homogeneous distribution of TiS_2 inside the carbon. The hexagonal arrangement of the spots in the SAED pattern confirms the purity of the phase and crystallinity of the materials. The CV, GCD, rate performance, and cycling stability plots were obtained. A specific capacity of 448 mA hg^{-1} was reported at 0.1 A g^{-1}, and it was maintained at approximately 387 mA h g^{-1} at a current density of 10 A g^{-1}. TiS_2@Cpvp showed a superior cycling stability of 92.5% capacity retention over 5000 cycles. Furthermore, the TiS_2@Cpvp/AC Na-ion capacitor showed 101.7 W h kg^{-1} energy density at a power density of 200 W kg^{-1}.

Similar to LIBs, the electrochemical properties of Na storage in SIBs are influenced by several factors, such as surface terminations, interplanar distance, types of MXenes, and structure of the materials. The Na-ion diffusion kinetics is generally slower than that of Li ions owing to its higher ionic radius. Hence, to achieve comparative specific capacities and other electrochemical properties for Na storage, it is essential to modify the structure of the MXene-based electrode materials according to requirements such as higher reactivity and shorter diffusion pathways. Therefore, the rational design of
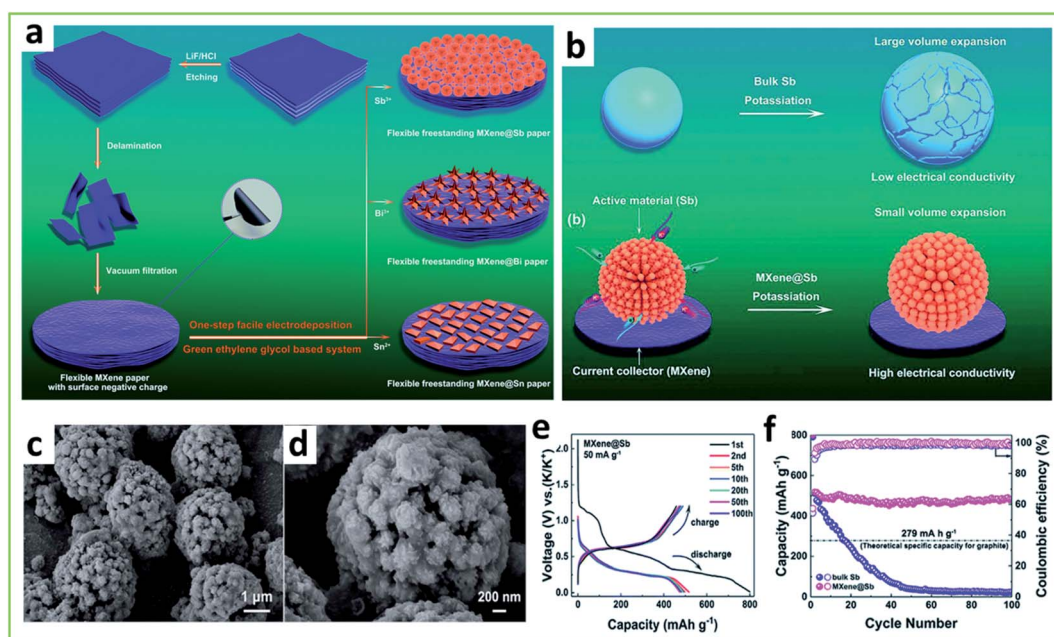
Fig. 24 (a) Schematic illustration of the overall fabrication process for flexible freestanding MXene@Sb, MXene@Bi, and MXene@Sn papers; (b) schematic diagrams for potassiation of bulk Sb and MXene@Sb anodes for K-ion batteries (KIBs); (b) potassiation schematic diagrams for bulk Sb and MXene@Sb anodes for KIBs, showing large volume expansion and poor electrical conductivity for bulk Sb and small volume expansion and high electrical conductivity for MXene@Sb; (c and d) typical SEM images of MXene@Sb anodes after 100 cycles; (e) GCD curves corresponding to MXene@Sb; (f) cycling stability performance of both anodes. (a–f) Are adapted with permission.[342] Copyright 2019, The Royal Society of Chemistry.

1136 | *J. Mater. Chem. A*, 2022, **10**, 1105–1149

This journal is © The Royal Society of Chemistry 2022

appropriate MXene-based materials for SIBs is an important challenge for future research.

4.2.3 MXenes for K-ion batteries. Gogotsi *et al.* reported the possibility of using MXene electrodes for K-ion batteries (KIBs) through a cation intercalation phenomena.[331] Cation intercalation into a layered structure is a well-known concept in the battery industry. However, there are only a few candidates that can act as host materials for cations with larger ionic radii than Li ions. Gogotsi *et al.* reported that 2D Ti_3C_2 MXenes can store various cations, including Na, K, Mg, and Al. They suggested that the XRD peak shifted to a low angle after the charging process based on *in situ* XRD measurements. This indicates that the intercalation reaction occurs in the MXene layer. Eames *et. al.*[332] also supported this experimental work through computational studies. A global screening of the intercalation phenomena of various ions into M_2C-based compounds (M = Sc, Ti, V, Cr, Zr, Nh, Mo, Hf, and Ta) with functionalized surfaces using diverse ions was conducted. By DFT calculations, it was determined that the most promising M_2C materials were light transition metals, such as Ti, which showed superior intercalation properties.

Naguib *et al.*[235] were the first to report MXene-based KIB anodes with organic electrolytes. They described the electrochemical performance of Ti_3CNT which was chosen because of its outstanding performance in LIBs. The Ti_3CNT electrode displays a high potassiation capacity of 710 mA h g^{-1} and depotassiation capacity of 202 mA h g^{-1} in the first cycle with 28.4% efficiency. The second cycle shows a higher efficiency of 56% with a depotassiation capacity of 154 mA h g^{-1}. The depotassiation capability of the MXene electrode was greater than that of the previously reported carbon nanofiber (75 mA h g^{-1}). The *ex situ* XRD results also confirmed that K^+ ions intercalated into the MXene layers. After potassiation, the XRD peak of Ti_3CNT was shifted to the low-angle region, which implies that the interlayer distance of MXene was increased due to the intercalation reaction. After this study, several studies have reported the development of high-performance KIB anode materials based on MXenes.[252,258,260,333–338] As part of this effort, there have been attempts to change the structure of MXene materials. Huang *et al.*[252] reported the hydrothermal synthesis of carbon-coated $MoSe_2$/MXene nanosheets for K storage. The 3D porous surface with a hierarchical 2D nanosheet structure of $MoSe_2$/MXene@C achieved a capacity of 355 mA hg^{-1} at a current density of 200 mA g^{-1} after 100 cycles, and it retained 183 mA h g^{-1} at 10 A g^{-1} and predicted excellent rate performance.

Dong *et al.*[245] reported Ti_3C_2 MXene-derived potassium titanate nanoribbons for KIB anodes. Ultrathin potassium titanate was successfully prepared by the simultaneous oxidation and alkalization of Ti_3C_2. This modification of the MXene material creates a suitable structure to store a large ionic radius of K ion such as wide interlayer distance (0.90 nm), narrow width (<60 nm), and ultrathin thickness (<11 nm). Electrochemical measurements showed that potassium titanate displayed a capacity of 151 mA h g^{-1} at a current density of 50 mA g^{-1}. Notably, it also showed superior long-term cycle stability over 900 cycles. This high performance was attributed to the

expanded *d*-spacing for significantly accommodating ions with large ionic radius in the interlayer channels by the intercalation reaction. The proposed charge/discharge mechanism is as follows.

$$K_2Ti_4O_9 + 2K^+ + 2e^- \leftrightarrow K_4Ti_4O_4 \qquad (12)$$

A similar approach to prepare a high-capacity KIB anode with MXene materials performs the alkalization of the MXene electrode. Lian *et al.*[233] reported alkalized Ti_3C_2 MXene nanoribbons with expanded interlayer distances for KIB anodes. Alkalized MXene nanoribbons were prepared by continuous shaking treatment in an aqueous KOH solution. The alkalized Ti_3C_2 (a-Ti_3C_2) showed high reversible capacities of 136 and 78 mA h g^{-1} at current densities of 20 and 200 mA g^{-1}, respectively. This is due to the increased interlayer spacing of a-Ti_3C_2 during the alkalization process, as well as the 3D interconnected porous structure enabling improved electron transport with high kinetics. The alkalization method used in this study was a facile and scalable method. This method could be used for other MXene materials to prepare electrodes for high electrochemical energy storage and for conversion.

Zhao *et al.*[258] reported self-assembled Ti_3C_2 MXenes and N-rich porous carbon nanosheets (NPCNs) as high-performance anodes for KIBs. The polymer PDDA-NPCNs/Ti_3C_2 hybrid structure was synthesized through an electrostatic self-assembly approach. The porous interconnected conductive network structure of PDDA-NPCNs and ex-Ti_3C_2 nanosheets offers short ion transport pathways. The GCD cycles of PDDA-NPCNs/Ti_3C_2, PDDA-NPCNs, and ex-Ti_3C_2 at 0.1 A g^{-1} clearly indicate the higher capacity of the electrode. The electrodes demonstrated an outstanding capacity of 358.4 mA h g^{-1} at 0.1 A g^{-1}, rate performance, and cycling stability (0.03% each cycle at 1.0 A g^{-1}). Moreover, the voltage profile and *ex situ* XRD patterns of the PDDA-NPCN/Ti_3C_2 electrode were studied in the few first cycles to anticipate the improved cycling stability and rate performance. During potassiation, the intensity of the peak of the NPCNs decreased and shifted to a lower angle, suggesting an increased interlayer distance of the NPCNs because of K^+ insertion. Furthermore, the (001) peak of Ti_3C_2 shifted to a lower angle, indicating the effective expansion of the interlayer distance (19.2 to 24.6 Å).

Zeng *et al.*[249] reported ultrathin titanate nanosheets/graphene films for KIB anode electrodes. They suggested the confined transformation of assembled 2D materials such as MXene and graphene oxide nanosheets to prepare freestanding films. They first confined MXene with rGO nanosheets and transformed MXene into ultrathin titanate for a well-confined layered structure, which demonstrated superior electrical conductivity owing to the ultrathin rGO nanosheets. The resulting film showed a good initial discharge capacity of 1094 mA h g^{-1} with a low coulombic efficiency of 24%. Moreover, the MXene/rGO film displayed superior rate capability with high remaining capacities of 228, 162, 116, and 84 mA h g^{-1} at current densities of 0.1–1 A g^{-1}. At a current density of 2 A g^{-1}, a high discharge capacity of 75 mA h g^{-1}

This journal is © The Royal Society of Chemistry 2022

J. Mater. Chem. A, 2022, **10**, 1105–1149 | **1137**

remained, which implies that the MXene/rGO film has a remarkable rate performance. This high-rate performance can be attributed to the advantages of the sandwich-type structure, which effectively prevents self-restacking of MXene and rGO nanosheets. The preparation of a sandwich structure not only increased the conductivity, but also prevented restacking during continuous electrochemical reactions such as intercalation of K^+ ions. Moreover, this sandwich structure can improve the mechanical strength of the film, which is an important factor for flexible batteries.

Tian et al.[342] synthesized Sb, Sn, and Bi hierarchical structures on MXene paper via a facile one-step electrodeposition process (Fig. 24a, c and d). A large volume expansion of bulk Sb anodes and small volume expansion of MXene@Sb anodes was observed during the potassiation process (Fig. 24b). In the large volume expansion, the electrical conductivity was poor; conversely, the small volume expansion showed higher electrical conductivity. MXene@Sb displayed a high reversible capacity of 516.8 mA h g^{-1} and superior cycling performance with a capacity fading rate of 0.042% per cycle (Fig. 24e and f).

4.2.4 MXenes for Zn-ion batteries. Aqueous electrolyte-based next-generation batteries have received interest owing to their distinct benefits, which include cheap cost, high safety, and minimal toxicity.[354–358] Particularly, aqueous electrolyte has better ionic conductivity ($\sim 10^{-1}$ S cm^{-1}) than that of organic electrolyte ($\sim 10^{-3}$–10^{-2} S cm^{-1}), which highly affects the overall performance of electrochemical batteries.[359–361] Recently, the cost of manufacturing LIBs has continued to rise owing to the overheated competition in the LIB market.[362,363] Consequently, the price competitiveness of next-generation batteries that do not use Li is also increasing.[364,365] Therefore, owing to its high ion conductivity and price competitiveness, many aqueous electrolyte-based batteries are being studied, and even among them ZIBs are attracting attention because of its superior characteristics.[356,366] ZIBs have multivalent aqueous ions with multiple electron transfers during the electrochemical reactions, which can maximize the high energy density and power density both.[367–369]

By introducing MXene electrodes for ZIBs, high energy density with superior power delivery can be achieved because a well-defined MXene structure can provide a highly efficient pathway for Zn ions with parallel pathways in the layered structure. Luo et. al.[370] reported nanoscale parallel circuitry-based conductive assemblies for high-power ZIBs. They prepared MnO_x-functionalized MXene stacks ($Ti_3C_2T_x$) with CNTs by a conductive assembly method, as shown in Fig. 25a.

Fig. 25 (a) Schematic illustration of the synthesis of $MnO_x@Ti_3C_2T_x$; (b) SEM images of multilayered $Ti_3C_2T_x$; (c) Fourier-transform infrared spectroscopy of Ti_3C_2Tx and $MnO_x@Ti_3C_2T_x$; (d) GCD profiles of $MnO_x@Ti_3C_2T_x$ at different current densities; (e) discharge profiles based on galvanostatic intermittent titration technique of $MnO_x@Ti_3C_2T_x$-based Zn-ion battery; (f) CV curves of $MnO_x@Ti_3C_2T_x$ based Zn-ion battery at different scan rates; (g) schematic illustration of the nanoscale-level parallel circuitry-based on $MnO_x@Ti_3C_2T_x$. (a–g) Are adapted with permission.[370] Copyright 2019, WILEY-VCH.

1138 | J. Mater. Chem. A, 2022, **10**, 1105–1149

This journal is © The Royal Society of Chemistry 2022

First, MXene was prepared by HF etching of raw material (Ti_3SiC_2, MAX phase) to form multilayered $Ti_3C_2T_x$ with various functional groups such as –F, –OH, and –O due to the slow oxidation of the dissolved O_2 in the etchant. The undersigned functional group is primarily related to the formation of anatase TiO_2, which can decrease the electrical conductivity of MXene materials. To avoid this side reaction, a strong oxidant, such as $KMnO_4$, was used to suppress the spontaneous oxidation and formation of TiO_2 by decorating the surface of MXene using MnO_x. MnO_x can bond uniformly with the MXene surface and prevent the formation of TiO_2. It can be clearly observed in Fig. 25b that MnO_x nanoparticles were uniformly formed on the surface of MXene with a rough surface.

The chemical properties of the $MnO_x@Ti_3C_2T_x$ flakes were investigated by Fourier-transform infrared (FTIR) spectroscopy, as shown in Fig. 25c. To test the electrochemical performance of $MnO_x@Ti_3C_2T_x$, GCD tests were performed, as shown in Fig. 25d, under different current densities. $MnO_x@Ti_3C_2T_x$ achieved a high reversible capacity of 88 mA h g^{-1} at a current density of 0.1 A g^{-1}. This capacity is primarily oriented from MnO_2 in the $MnO_x@Ti_3C_2T_x$ structure because the individual capacity of MnO_2 (~270 mA h g^{-1}) is significantly higher than that of MXene. However, only MnO_x without the MXene structure displays a considerably low reversible capacity of 30 mA h g^{-1} with a stainless-steel current collector, which implies that MXene perform an important role in electrochemical reactions. The first plateau of the overvoltage in the galvanostatic intermittent titration technique (GITT) measurement is smaller than that of the second plateau owing to the variation in ion intercalation (Fig. 25e). The first plateau is caused by the intercalation of protons owing to the existence of an electrolyte without any Zn ions. The second plateau is attributed to Zn-ion intercalation. It can be clearly observed that the second plateau is lower than that of the $MnO_x@Ti_3C_2T_x$ structure. This can be ascribed to the fact that the high conductivity of MXene with a skeleton structure can enhance the electron transfer of MnO_x by introducing a parallel reaction in the layered structure. The result of kinetic analysis by power law from CV curves at different scan rates also supports this fact, as shown in Fig. 25f.

To develop a cheap and nontoxic electrode material, a CNT-delaminated V_2C MXene electrode was recommended by Wang et al.[371] for Zn-ion storage applications. Typically, MXene has an interactable layer structure with a rich surface chemical available, which makes it a promising active material. However, despite several successful studies on MXene ZIB electrodes, there are considerable bottlenecks related to MXene electrodes, such as dynamic structural changes and limited life cycle due to performance failure. To overcome these limitations, intensive research should be conducted to understand the working mechanism by in situ and operando measurements. Wang et al.[371] reported freestanding porous films with delaminated V_2C MXene and CNT composites. Furthermore, operando X-ray absorption spectroscopic analysis was performed to understand the charge/discharge mechanism. To synthesize the delaminated VC_2 and CNT composite ($DV_2C@CNT$) freestanding film, pristine V_2C was prepared from V_2AlC MAX phase using the HF

etching method. After HF etching, the pristine V_2C exhibited an accordion-like architecture with a distinct layered structure. Subsequently, the delaminated process was conducted by intercalation of TMAOH, which has a strong van der Waals force between the interlayers of MXene.[355] This force can induce self-restacking of V_2C MXene particles. Therefore, CNTs can be uniformly introduced into the interlayer. The prepared freestanding film had a thickness of 5 μm, and the SEM cross-sectional images of $DV_2C@CNT$ showed a uniformly mixed structure. To evaluate the electrochemical performance of the freestanding film, a hybrid cell with $DV_2C@CNT//ZnSO_4//Zn$ was prepared with a $DV_2@CNT$ cathode and Zn foil as the anode. After the assembly of this cell, nanoflakes were immediately formed on both the cathode and anode sides. The sharp XRD peaks at 9.5 and 8.1 can be attributed to intercalated water molecules, and the other peaks indicate that the precipitated nanoflakes were zinc hydroxide sulfate hydrate (ZHS). The possible reaction mechanism of precipitation is as follows.

$$4Zn^{2+} + 6OH^- + SO_4^{2-} + nH_2O \leftrightarrow (Zn(OH)_2)_3(ZnSO_4)(H_2O)_n \quad (13)$$
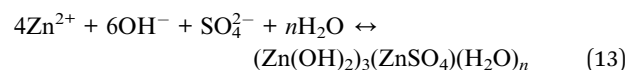
The formation of ZHS can induce an electrostatic field in the primary Zn battery. Because of this electrostatic field, the –OH ions moved to the surface of the electrode and generated the formation of ZHS nanoflakes. To determine the reason and effect of precipitation, synchrotron-based X-ray absorption fine structure spectroscopy was conducted on the as-prepared Zn primary cell. CV and electrochemical impedance spectroscopy plots were obtained. The apparent redox peaks illustrate the pseudocapacitance contribution as well as reversibility because of the insertion/extraction of Zn ions within the interlayer of MXene. Additionally, the co-contribution of H^+/Zn^{2+} was confirmed by the GITT profiles. During the first discharge cycle, the diffusion coefficient slowly increased to 1.08×10^{-11} cm^2 s^{-1}. The schematic representation shows the insertion of H^+ and Zn^{2+} throughout discharge cycles within 1.1–0.71 V and 0.71–0.32 V as well as CV cycles at 10 mV s^{-1} with charge contribution profile.

Li et al.[372] synthesized vertically aligned Sn^{4+} pre-intercalated Ti_2CT_X MXene spheres and used them for ZICs. The Ti_2AlC MAX coating was synthesized on carbon spheres, and then HF acid was used to etch the MAX phases to synthesize Ti_2CT_X. The CV curves of the Ti_2AlC/C, Ti_2CT_X/C, and $Sn^{4+}-Ti_2CT_X/C$ spheres within potentials of 0.1 to 2.0 V at 2 mV s^{-1} show redox peaks, which confirm the pseudocapacitive behavior of electrodes. The cycling stability and rate performance of the samples were also depicted. $Sn^{4+}-Ti_2CT_X/C$ shows specific capacities of 138 and 92 mA h g^{-1} at 0.1 and 5 A g^{-1}, respectively, indicating superior rate performance. The ion transport paths of random Ti_2CT_X particles and Ti_2CT_X/C spheres were also analyzed. It was observed that after Sn^{4+} pre-intercalation, the interlayer spacing increased from 1.15 to 1.27 nm. Therefore, the capacity of the electrodes was improved. The prepared device can operate at low temperatures such as −20 °C. The schematic of the future research progress, advanced characterization and challenges of
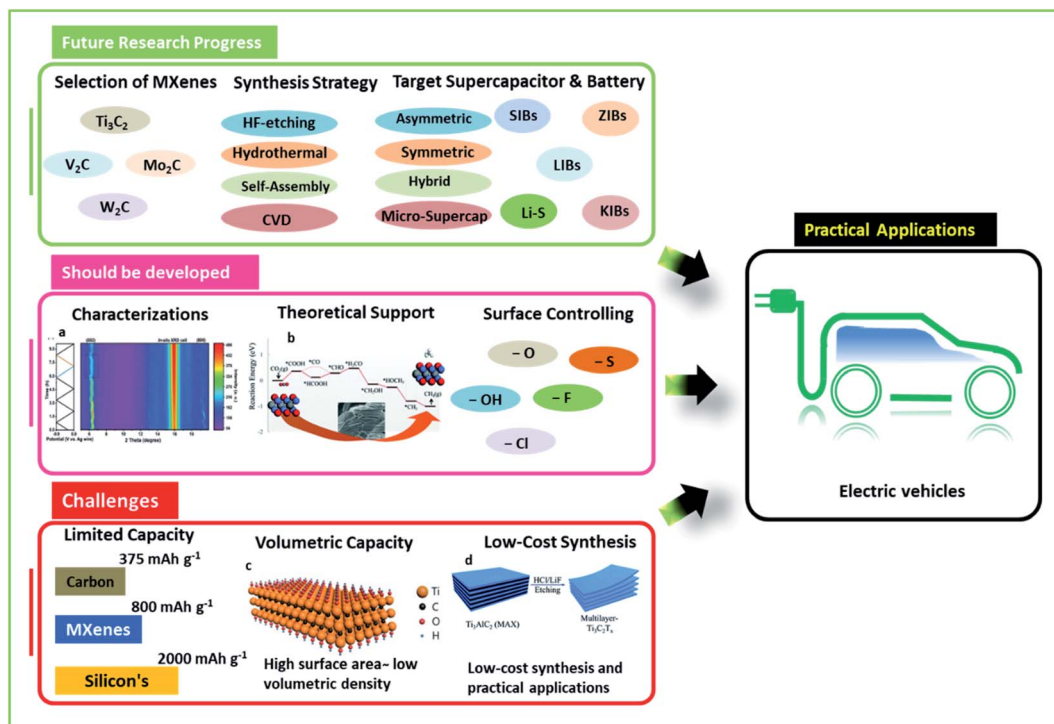
Fig. 26 Prospective applications and challenges of MXene–based battery research. (a) Is adapted with permission.[373] Copyright 2019, WILEY-VCH. (b) Is adapted with permission.[102] Copyright 2019, The Royal Society of Chemistry. (c) Is adapted with permission.[374] Copyright 2018, American Chemical Society. (d) Is adapted with permission.[375] Copyright 2019, The Royal Society of Chemistry.

the MXene based electrodes development is represented in Fig. 26.

5. Conclusions and perspectives

Owing to the key features of MXenes, such as 2D lamellar structures, varying surface terminations, metallic conductivity, and intercalation pseudocapacitance, MXene materials are a considerably appealing prospect for energy storage SCs with high energy and power densities when compared to conventional materials. This study highlights the synthesis, properties, and progress of research on MXene-based electrochemical energy storage systems, including SCs, LIBs, SIBs, KIBs, and ZIBs. Despite the fact that the synthesized MXenes have good electrochemical performance in non-Li energy storage devices, there are still a number of challenges to be addressed. Researchers are concentrating on $Ti_3C_2T_X$ MXene, although a small percentage of Ti_2CT_X and V_2CT_X materials also contributed to the performance. The structure of the most researched MXene, $Ti_3C_2T_X$, is well characterized and understood; however, studies on other MXenes must be prioritized. Although MXene is utilized as the electrode material for secondary batteries, there is still considerable room for improvement in terms of capacity. Based on the content of this review article, the following paths should be pursued in future research and development of MXene SCs and batteries:

(1) to maximize the merits of MXene materials, it is necessary to develop systematic research and development methods. It is important to select an appropriate target because of the

characteristics of MXene-related SCs and battery research, which is the main research point for improving the characteristics through composite formation with various materials. It is important to select an appropriate energy storage device according to the performance required by the target, that is, energy density or high-power density. Each battery technology has its own energy storage mechanism, and the characteristics that appear accordingly also change. Therefore, it is significantly important to choose an appropriate battery technology. There are various candidate groups for MXene materials, and it is important to identify MXene materials suitable for the desired characteristics among these candidate groups. The current MXene technology focuses on changing properties due to the formation of a composite between MXene and other materials, and not a comparison between various MXene materials. Therefore, for a commercially available MXene-based battery research, a comparison between MXene materials and study on the characteristics of each MXene material must be performed. To maximize the properties of MXene materials, it is important to manufacture MXenes with an optimal structure through the development of an appropriate synthesis method.

(2) Several supporting technologies must be developed for the successful development of MXene-based batteries. First, a characterization method suited for MXene analysis must be developed. The specific surface area of MXene materials is greater than that of traditional battery materials. Furthermore, the crystallinity is poor when compared to typical LIB cathode materials. Consequently, more efficient research can be performed if an improved analytical technique for MXene

1140 | J. Mater. Chem. A, 2022, **10**, 1105–1149

This journal is © The Royal Society of Chemistry 2022

materials is devised. It is also critical to employ *in situ* and *ex situ* analytical methodologies for electrodes used in SCs and battery manufacturing. Furthermore, the experimental results should be validated by theoretical studies, and a new research and development strategy should be proposed. Because MXene materials have a shorter research and development time than other materials, practical and theoretical investigations must be performed concurrently for quick development. Finally, technologies for regulating the surface characteristics of MXene materials must be developed. The development of a surface functional group is unavoidable because of the characteristics of MXene materials generated by the acidic etching technique. Consequently, if the production of this surface functional group can be regulated and the conversion to another surface functional group is feasible, the characteristics of MXene materials can be enhanced.

(3) Nevertheless, morphological modifications are crucial for expanding active sites. For energy storage applications, such as SCs and rechargeable batteries, the regulation of porosity and curvature of MXene nanomaterials in 2D may create a high surface area and pore volume. Therefore, each application has its own requirements for the structure or composition of MXene materials in terms of their structure. In the case of LIBs and SIBs, for the best initial coulombic efficiency, electrode materials should be devoid of any defects or functional groups. A good cycle life may be attained with Li–S batteries if the shuttle effect of polysulfides is reduced. As Li–S batteries include polysulfide molecules, MXene materials must have strong polysulfide molecular trapping capabilities.

(4) Finally, numerous issues must be resolved to commercialize MXene materials. First, there is an issue with limited reversible capacity when compared to conversion-type materials. MXene compounds have a limited reversible capacity than high-capacity materials such as silicon. Consequently, it is critical to increase or utilize the distinct benefits of MXene materials. The second issue is volumetric capacity maximization. The volumetric capacity is limited owing to the properties of MXene materials with high surface areas. Therefore, this problem must be resolved for its utilization in commercially available batteries. Finally, a low-cost synthesis procedure was developed.

The following factors should be highlighted to further support the rapid development of MXenes. (1) Reducing the preparation of MAX and MXene, reducing the costs, clarifying important elements that affect the preparation process, and exploring innovative, environmentally friendly etching technologies are all goals of this project. (2) The interaction between MXene and the utilized solvents must be examined to achieve modifications and stability of MXenes, antioxidants, and other factors. (3) The effects of surface terminations on the properties and the different applications of MXenes must be investigated. (4) The theoretical simulations computation capability must be intensified, and it must be utilized as a guide for selecting additional viable MAX and MXene possibilities. (5) In addition to power and energy densities, MXene-based hybrid SCs have significant practical utility and merit further study. (6) Further research on solid secondary batteries based on MXene

electrodes and their applications must be performed. (7) The packing of MXene-based devices must be investigated. (8) It is also necessary to optimize its structural design to maximize its volumetric capacity. (9) It is critical to develop a flexible and transparent MXene film for future wearable electronic equipment.

Conflicts of interest

There are no conflicts to declare.

Acknowledgements

References

1 E. Linda, A. Metelitsa, J. Barden, M. Mellish, B. Murphy, B. Hojjati, P. Gross, V. Zaretskaya and P. Lindstrom, *US DoE.*, Washington, DC, 2013, p. 20585.
2 S. Chu and A. Majumdar, *Nature*, 2012, **488**, 294–303.
3 Y. Wang, Y. Song and Y. Xia, *Chem. Soc. Rev.*, 2016, **45**, 5925–5950.
4 D.-H. Liu, Z. Bai, M. Li, A. Yu, D. Luo, W. Liu, L. Yang, J. Lu, K. Amine and Z. Chen, *Chem. Soc. Rev.*, 2020, **49**, 5407–5445.
5 A. M. Patil, X. Yue, A. Yoshida, S. Li, X. Hao, A. Abudula and G. Guan, *Appl. Mater. Today*, 2020, **19**, 100563.
6 P. Simon and Y. Gogotsi, in *Nanoscience and technology: a collection of reviews from Nature journals*, World Scientific, 2010, pp. 320–329.
7 K. Fic, A. Platek, J. Piwek and E. Frackowiak, *Mater. Today*, 2018, **21**, 437–454.
8 A. M. Patil, J. Wang, S. Li, X. Hao, X. Du, Z. Wang, X. Hao, A. Abudula and G. Guan, *Chem. Eng. J.*, 2021, **421**, 127883.
9 D. P. Dubal, O. Ayyad, V. Ruiz and P. Gomez-Romero, *Chem. Soc. Rev.*, 2015, **44**, 1777–1790.
10 A. M. Patil, A. C. Lokhande, N. R. Chodankar, V. S. Kumbhar and C. D. Lokhande, *Mater. Des.*, 2016, **97**, 407–416.
11 A. K. Geim and K. S. Novoselov, in *Nanoscience and technology: a collection of reviews from nature journals*, World Scientific, 2010, pp. 11–19.
12 H. Zeng, C. Zhi, Z. Zhang, X. Wei, X. Wang, W. Guo, Y. Bando and D. Golberg, *Nano Lett.*, 2010, **10**, 5049–5055.

This journal is © The Royal Society of Chemistry 2022

J. Mater. Chem. A, 2022, **10**, 1105–1149 | **1141**

13 T. Yang, T. T. Song, M. Callsen, J. Zhou, J. W. Chai, Y. P. Feng, S. J. Wang and M. Yang, *Adv. Mater. Interfaces*, 2019, **6**, 1801160.

14 M. Naguib, M. Kurtoglu, V. Presser, J. Lu, J. Niu, M. Heon, L. Hultman, Y. Gogotsi and M. W. Barsoum, *Adv. Mater.*, 2011, **23**, 4248–4253.

15 M. Naguib, V. N. Mochalin, M. W. Barsoum and Y. Gogotsi, *Adv. Mater.*, 2014, **26**, 992–1005.

16 B. Anasori, M. R. Lukatskaya and Y. Gogotsi, *Nat. Rev. Mater.*, 2017, **2**, 1–17.

17 M. Ghidiu, M. R. Lukatskaya, M.-Q. Zhao, Y. Gogotsi and M. W. Barsoum, *Nature*, 2014, **516**, 78–81.

18 T. Y. Ma, J. L. Cao, M. Jaroniec and S. Z. Qiao, *Angew. Chem.*, 2016, **128**, 1150–1154.

19 Z. W. Seh, K. D. Fredrickson, B. Anasori, J. Kibsgaard, A. L. Strickler, M. R. Lukatskaya, Y. Gogotsi, T. F. Jaramillo and A. Vojvodic, *ACS Energy Lett.*, 2016, **1**, 589–594.

20 G. Gao, A. P. O'Mullane and A. Du, *ACS Catal.*, 2017, **7**, 494–500.

21 E. Lee and D.-J. Kim, *J. Electrochem. Soc.*, 2019, **167**, 037515.

22 N. Hemanth, T. Kim, B. Kim, A. H. Jadhav, K. Lee and N. K. Chaudhari, *Mater. Chem. Front.*, 2021, **5**, 3298–3321.

23 T. Zhou, C. Wu, Y. Wang, A. P. Tomsia, M. Li, E. Saiz, S. Fang, R. H. Baughman, L. Jiang and Q. Cheng, *Nat. Commun.*, 2020, **11**, 1–11.

24 W. Bao, X. Xie, J. Xu, X. Guo, J. Song, W. Wu, D. Su and G. Wang, *Chem. - Eur. J.*, 2017, **23**, 12613–12619.

25 R. Li, W. Sun, C. Zhan, P. R. Kent and D.-e. Jiang, *Phys. Rev. B*, 2019, **99**, 085429.

26 Y. Aierken, C. Sevik, O. Gülseren, F. M. Peeters and D. Çakır, *J. Mater. Chem. A*, 2018, **6**, 2337–2345.

27 K. A. Papadopoulou, A. Chroneos, D. Parfitt and S.-R. G. Christopoulos, *J. Appl. Phys.*, 2020, **128**, 170902.

28 Y. Wang, Y. Xu, M. Hu, H. Ling and X. Zhu, *Nanophotonics*, 2020, **9**, 1601–1620.

29 M. W. Barsoum, *MAX phases: properties of machinable ternary carbides and nitrides*, John Wiley & Sons, 2013.

30 L. Verger, C. Xu, V. Natu, H.-M. Cheng, W. Ren and M. W. Barsoum, *Curr. Opin. Solid State Mater. Sci.*, 2019, **23**, 149–163.

31 O. M. Michael Naguib, J. Carle, V. Presser, J. Lu, L. Hultman and a. M. W. B. Yury Gogotsi, *ACS Nano*, 2012, **6**, 1322–1331.

32 G. Ying, A. D. Dillon, A. T. Fafarman and M. W. Barsoum, *Mater. Res. Lett.*, 2017, **5**, 391–398.

33 M. Alhabeb, K. Maleski, B. Anasori, P. Lelyukh, L. Clark, S. Sin and Y. Gogotsi, *Chem. Mater.*, 2017, **29**, 7633–7644.

34 W. Sun, S. A. Shah, Y. Chen, Z. Tan, H. Gao, T. Habib, M. Radovic and M. J. Green, *J. Mater. Chem. A*, 2017, **5**, 21663–21668.

35 J. Halim, M. R. Lukatskaya, K. M. Cook, J. Lu, C. R. Smith, L. A. Naslund, S. J. May, L. Hultman, Y. Gogotsi, P. Eklund and M. W. Barsoum, *Chem. Mater.*, 2014, **26**, 2374–2381.

36 T. Li, L. Yao, Q. Liu, J. Gu, R. Luo, J. Li, X. Yan, W. Wang, P. Liu, B. Chen, W. Zhang, W. Abbas, R. Naz and D. Zhang, *Angew. Chem., Int. Ed. Engl.*, 2018, **57**, 6115–6119.

37 S. Yang, P. Zhang, F. Wang, A. G. Ricciardulli, M. R. Lohe, P. W. M. Blom and X. Feng, *Angew. Chem., Int. Ed. Engl.*, 2018, **57**, 15491–15495.

38 M. Alhabeb, K. Maleski, T. S. Mathis, A. Sarycheva, C. B. Hatter, S. Uzun, A. Levitt and Y. Gogotsi, *Angew. Chem., Int. Ed. Engl.*, 2018, **57**, 5444–5448.

39 J. Zhou, X. Zha, X. Zhou, F. Chen, G. Gao, S. Wang, C. Shen, T. Chen, C. Zhi, P. Eklund, S. Du, J. Xue, W. Shi, Z. Chai and Q. Huang, *ACS Nano*, 2017, **11**, 3841–3850.

40 J. Zhou, X. Zha, F. Y. Chen, Q. Ye, P. Eklund, S. Du and Q. Huang, *Angew. Chem., Int. Ed. Engl.*, 2016, **55**, 5008–50013.

41 H. N. J. C. Schuster and C. Vaccaro, *J. Solid State Chem.*, 1980, **32**, 213–219.

42 P. R. Hans Nowotny and J. C. Schuster, *J. Solid State Chem.*, 1982, **44**, 126–133.

43 Z. Liu, L. Zheng, L. Sun, Y. Qian, J. Wang, M. Li and G. P. Bei, *J. Am. Ceram. Soc.*, 2014, **97**, 67–69.

44 B. Anasori, Y. Xie, M. Beidaghi, J. Lu, B. C. Hosler, L. Hultman, P. R. Kent, Y. Gogotsi and M. W. Barsoum, *ACS Nano*, 2015, **9**, 9507–9516.

45 R. Meshkian, Q. Tao, M. Dahlqvist, J. Lu, L. Hultman and J. Rosen, *Acta Mater.*, 2017, **125**, 476–480.

46 R. Meshkian, M. Dahlqvist, J. Lu, B. Wickman, J. Halim, J. Thornberg, Q. Tao, S. Li, S. Intikhab, J. Snyder, M. W. Barsoum, M. Yildizhan, J. Palisaitis, L. Hultman, P. O. A. Persson and J. Rosen, *Adv. Mater.*, 2018, **30**, e1706409.

47 M. Dahlqvist, J. Lu, R. Meshkian, Q. Tao, L. Hultman and J. Rosen, *Sci. Adv.*, 2017, **3**, e1700642.

48 X. Zhao, A. Vashisth, E. Prehn, W. Sun, S. A. Shah, T. Habib, Y. Chen, Z. Tan, J. L. Lutkenhaus, M. Radovic and M. J. Green, *Matter*, 2019, **1**, 513–526.

49 L. Ma, L. R. L. Ting, V. Molinari, C. Giordano and B. S. Yeo, *J. Mater. Chem. A*, 2015, **3**, 8361–8368.

50 Y. Gogotsi and Q. Huang, *ACS Nano*, 2021, **15**, 5775–5780.

51 O. Mashtalir, M. Naguib, V. N. Mochalin, Y. Dall'Agnese, M. Heon, M. W. Barsoum and Y. Gogotsi, *Nat. Commun.*, 2013, **4**, 1716.

52 O. Mashtalir, M. R. Lukatskaya, M. Q. Zhao, M. W. Barsoum and Y. Gogotsi, *Adv. Mater.*, 2015, **27**, 3501–3506.

53 M. Naguib, R. R. Unocic, B. L. Armstrong and J. Nanda, *Dalton Trans.*, 2015, **44**, 9353–9358.

54 B. Anasori, C. Shi, E. J. Moon, Y. Xie, C. A. Voigt, P. R. C. Kent, S. J. May, S. J. L. Billinge, M. W. Barsoum and Y. Gogotsi, *Nanoscale Horiz.*, 2016, **1**, 227–234.

55 P. Urbankowski, B. Anasori, T. Makaryan, D. Er, S. Kota, P. L. Walsh, M. Zhao, V. B. Shenoy, M. W. Barsoum and Y. Gogotsi, *Nanoscale*, 2016, **8**, 11385–11391.

56 J. Halim, S. Kota, M. R. Lukatskaya, M. Naguib, M.-Q. Zhao, E. J. Moon, J. Pitock, J. Nanda, S. J. May, Y. Gogotsi and M. W. Barsoum, *Adv. Funct. Mater.*, 2016, **26**, 3118–3127.

57 V. Kamysbayev, A. S. Filatov, H. Hu, X. Rui, F. Lagunas, D. Wang, R. F. Klie and D. V. Talapin, *Science*, 2020, **369**, 979–983.

58 L. Yu, L. Lu, X. Zhou, L. Xu, Z. Alhalili and F. Wang, *ChemElectroChem*, 2021, **8**, 1948–1987.

59 Y. Li, H. Shao, Z. Lin, J. Lu, L. Liu, B. Duployer, P. O. A. Persson, P. Eklund, L. Hultman, M. Li, K. Chen, X. H. Zha, S. Du, P. Rozier, Z. Chai, E. Raymundo-Pinero, P. L. Taberna, P. Simon and Q. Huang, *Nat. Mater.*, 2020, **19**, 894–899.

60 L.-Y. Xiu, Z.-Y. Wang and J.-S. Qiu, *Rare Met.*, 2020, **39**, 1237–1238.

61 J. Lu, I. Persson, H. Lind, J. Palisaitis, M. Li, Y. Li, K. Chen, J. Zhou, S. Du, Z. Chai, Z. Huang, L. Hultman, P. Eklund, J. Rosen, Q. Huang and P. O. Å. Persson, *Nanoscale Adv.*, 2019, **1**, 3680–3685.

62 M. Naguib, V. Presser, D. Tallman, J. Lu, L. Hultman, Y. Gogotsi, M. W. Barsoum and Y. Zhou, *J. Am. Ceram. Soc.*, 2011, **94**, 4556–4561.

63 M. Li, J. Lu, K. Luo, Y. Li, K. Chang, K. Chen, J. Zhou, J. Rosen, L. Hultman, P. Eklund, P. O. A. Persson, S. Du, Z. Chai, Z. Huang and Q. Huang, *J. Am. Chem. Soc.*, 2019, **141**, 4730–4737.

64 Z. Bao, C. Lu, X. Cao, P. Zhang, L. Yang, H. Zhang, D. Sha, W. He, W. Zhang, L. Pan and Z. Sun, *Chin. Chem. Lett.*, 2021, **32**, 2648–2658.

65 F. Zhang, Z. Zhang, H. Wang, C. H. Chan, N. Y. Chan, X. X. Chen and J.-Y. Dai, *Phys. Rev. Mater.*, 2017, **1**, 034002.

66 R. Deng, H. Zhang, Y. Zhang, Z. Chen, Y. Sui, X. Ge, Y. Liang, S. Hu, G. Yu and D. Jiang, *Chin. Phys. B*, 2017, **26**, 067901.

67 X. Xiao, H. Yu, H. Jin, M. Wu, Y. Fang, J. Sun, Z. Hu, T. Li, J. Wu, L. Huang, Y. Gogotsi and J. Zhou, *ACS Nano*, 2017, **11**, 2180–2186.

68 M. Zeng, Y. Chen, J. Li, H. Xue, R. G. Mendes, J. Liu, T. Zhang, M. H. Rümmeli and L. Fu, *Nano Energy*, 2017, **33**, 356–362.

69 Z. Wang, V. Kochat, P. Pandey, S. Kashyap, S. Chattopadhyay, A. Samanta, S. Sarkar, P. Manimunda, X. Zhang, S. Asif, A. K. Singh, K. Chattopadhyay, C. S. Tiwary and P. M. Ajayan, *Adv. Mater.*, 2017, **29**, 1700364.

70 S. Joshi, Q. Wang, A. Puntambekar and V. Chakrapani, *ACS Energy Lett.*, 2017, **2**, 1257–1262.

71 C. Xu, L. Chen, Z. Liu, H.-M. Cheng and W. Ren, Bottom-Up Synthesis of 2D Transition Metal Carbides and Nitrides, in *2D Metal Carbides and Nitrides (MXenes)*, ed. B. Anasori and Y. Gogotsi, Springer, Cham, 2019, DOI: 10.1007/978-3-030-19026-2_6.

72 Z. Liu, C. Xu, N. Kang, L. Wang, Y. Jiang, J. Du, Y. Liu, X. L. Ma, H. M. Cheng and W. Ren, *Nano Lett.*, 2016, **16**, 4243–4250.

73 C. Xu, L. Wang, Z. Liu, L. Chen, J. Guo, N. Kang, X. L. Ma, H. M. Cheng and W. Ren, *Nat. Mater.*, 2015, **14**, 1135–1141.

74 D. Geng, X. Zhao, Z. Chen, W. Sun, W. Fu, J. Chen, W. Liu, W. Zhou and K. P. Loh, *Adv. Mater.*, 2017, **29**, 1700072.

75 J.-B. Qiao, Y. Gong, W.-J. Zuo, Y.-C. Wei, D.-L. Ma, H. Yang, N. Yang, K.-Y. Qiao, J.-A. Shi, L. Gu and L. He, *Phys. Rev. B*, 2017, **95**, 201403.

76 C. Xu, S. Song, Z. Liu, L. Chen, L. Wang, D. Fan, N. Kang, X. Ma, H. M. Cheng and W. Ren, *ACS Nano*, 2017, **11**, 5906–5914.

77 S. Chaitoglou, P. Tsipas, T. Speliotis, G. Kordas, A. Vavouliotis and A. Dimoulas, *J. Cryst. Growth*, 2018, **495**, 46–53.

78 J.-B. Qiao, Y. Gong, H. Liu, J.-A. Shi, L. Gu and L. He, *Phys. Rev. Mater.*, 2018, **2**, 054002.

79 Q. Chen, D. Zhang, J. Pan and W. Fan, *Optik*, 2020, **219**, 165046.

80 Y. W. Sicong Liu, R. Lv, J. Wang, H. Wang, Y. Wang and L. Duan, *Nanophotonics*, 2012, **9**, 2192–8614.

81 G. Li, L. Yang, R. Zhao, F. Wang, H. Nie, R. Wang, K. Yang, B. Zhang and J. He, *Appl. Opt.*, 2020, **59**, 11240–11245.

82 J. Wang, Y. Wang, S. Liu, G. Li, G. Zhang and G. Cheng, *Nanomaterials*, 2020, **10**, 2391.

83 J. Wang, S. Liu, Y. Wang, T. Wang, S. Shang and W. Ren, *J. Mater. Chem. C*, 2020, **8**, 1608–1613.

84 J. Jia, T. Xiong, L. Zhao, F. Wang, H. Liu, R. Hu, J. Zhou, W. Zhou and S. Chen, *ACS Nano*, 2017, **11**, 12509–12518.

85 Z. Zhang, F. Zhang, H. Wang, C. Ho Chan, W. Lu and J.-y. Dai, *J. Mater. Chem. C*, 2017, **5**, 10822–10827.

86 M. Alhabeb, K. Maleski, B. Anasori, P. Lelyukh, L. Clark, S. Sin and Y. Gogotsi, *Chem. Mater.*, 2017, **29**, 7633–7644.

87 B. Anasori and Y. Gogotsi, *2D Metal carbides and nitrides (MXenes): Structure, properties and applications*, 2019.

88 N. M. Caffrey, *Nanoscale*, 2018, **10**, 13520–13530.

89 X. Xie, Y. Xue, L. Li, S. Chen, Y. Nie, W. Ding and Z. Wei, *Nanoscale*, 2014, **6**, 11035–11040.

90 X. Li, M. Li, Q. Yang, G. Liang, Z. Huang, L. Ma, D. Wang, F. Mo, B. Dong, Q. Huang and C. Zhi, *Adv. Energy Mater.*, 2020, **10**, 2001791.

91 M. Khazaei, M. Arai, T. Sasaki, C.-Y. Chung, N. S. Venkataramanan, M. Estili, Y. Sakka and Y. Kawazoe, *Adv. Funct. Mater.*, 2013, **23**, 2185–2192.

92 S. Kajiyama, L. Szabova, H. Iinuma, A. Sugahara, K. Gotoh, K. Sodeyama, Y. Tateyama, M. Okubo and A. Yamada, *Adv. Energy Mater.*, 2017, **7**, 1601873.

93 X. Jiang, A. V. Kuklin, A. Baev, Y. Ge, H. Ågren, H. Zhang and P. N. Prasad, *Phys. Rep.*, 2020, **848**, 1–58.

94 Z. H. Fu, Q. F. Zhang, D. Legut, C. Si, T. C. Germann, T. Lookman, S. Y. Du, J. S. Francisco and R. F. Zhang, *Phys. Rev. B*, 2016, **94**, 104103.

95 M. Magnuson, J. Halim and L.-Å. Näslund, *J. Electron Spectrosc. Relat. Phenom.*, 2018, **224**, 27–32.

96 V. Natu, M. Sokol, L. Verger and M. W. Barsoum, *J. Phys. Chem. C*, 2018, **122**, 27745–27753.

97 M. A. Hope, A. C. Forse, K. J. Griffith, M. R. Lukatskaya, M. Ghidiu, Y. Gogotsi and C. P. Grey, *Phys. Chem. Chem. Phys.*, 2016, **18**, 5099–5102.

98 M. N. Hsiu-Wen Wang, K. Page, D. J. Wesolowski and Y. Gogotsi, *Chem. Mater.*, 2016, **28**, 349–359.

99 X. Wang, X. Shen, Y. Gao, Z. Wang, R. Yu and L. Chen, *J. Am. Chem. Soc.*, 2015, **137**, 2715–2721.

100 J. Halim, K. M. Cook, M. Naguib, P. Eklund, Y. Gogotsi, J. Rosen and M. W. Barsoum, *Appl. Surf. Sci.*, 2016, **362**, 406–417.

101 L. H. Karlsson, J. Birch, J. Halim, M. W. Barsoum and P. O. Persson, *Nano Lett.*, 2015, **15**, 4955–4960.

This journal is © The Royal Society of Chemistry 2022

J. Mater. Chem. A, 2022, **10**, 1105–1149 | 1143

102 A. D. Handoko, S. N. Steinmann and Z. W. Seh, *Nanoscale Horiz.*, 2019, **4**, 809–827.

103 Z. Lin, H. Shao, K. Xu, P.-L. Taberna and P. Simon, *Trends Chem.*, 2020, **2**, 654–664.

104 A. S. F. Vladislav Kamysbayev, H. Hu, X. Rui, F. Lagunas, D. Wang, R. F. Klie and D. V. Talapin, *Science*, 2020, **369**, 979–983.

105 L. Dong, H. Kumar, B. Anasori, Y. Gogotsi and V. B. Shenoy, *J. Phys. Chem. Lett.*, 2017, **8**, 422–428.

106 M. Hu, H. Zhang, T. Hu, B. Fan, X. Wang and Z. Li, *Chem. Soc. Rev.*, 2020, **49**, 6666–6693.

107 M. Khazaei, A. Ranjbar, M. Arai and S. Yunoki, *Phys. Rev. B*, 2016, **94**, 125152.

108 Y. Lee, Y. Hwang, S. B. Cho and Y. C. Chung, *Phys. Chem. Chem. Phys.*, 2014, **16**, 26273–26278.

109 N. K. Chaudhari, H. Jin, B. Kim, D. San Baek, S. H. Joo and K. Lee, *J. Mater. Chem. A*, 2017, **5**, 24564–24579.

110 C. Zhang, Y. Ma, X. Zhang, S. Abdolhosseinzadeh, H. Sheng, W. Lan, A. Pakdel, J. Heier and F. Nüesch, *Energy Environ. Mater.*, 2020, **3**, 29–55.

111 J. Xu, J. Shim, J.-H. Park and S. Lee, *Adv. Funct. Mater.*, 2016, **26**, 5328–5334.

112 L. Zhou, Y. Zhang, Z. Zhuo, A. J. Neukirch and S. Tretiak, *J. Phys. Chem. Lett.*, 2018, **9**, 6915–6920.

113 J. Jeon, Y. Park, S. Choi, J. Lee, S. S. Lim, B. H. Lee, Y. J. Song, J. H. Cho, Y. H. Jang and S. Lee, *ACS Nano*, 2018, **12**, 338–346.

114 H. Lashgari, M. R. Abolhassani, A. Boochani, S. M. Elahi and J. Khodadadi, *Solid State Commun.*, 2014, **195**, 61–69.

115 M. S.-B. D. C. Hutchings, D. J. Hagan and E. W. Van Stryland, *Opt. Quantum Electron.*, 1992, **24**, 1–30.

116 G. Y. Haijun Zhang, X. Zuo, H. Tang, Q. Yang and G. Li, *J. Mater. Chem. A*, 2016, **4**, 12913–12920.

117 E. Satheeshkumar, T. Makaryan, A. Melikyan, H. Minassian, Y. Gogotsi and M. Yoshimura, *Sci. Rep.*, 2016, **6**, 32049.

118 A. Lipatov, H. Lu, M. Alhabeb, B. Anasori, A. Gruverman, Y. Gogotsi and A. Sinitskii, *Sci. Adv.*, 2018, **4**, eaat0491.

119 H. Wang, Y. Wu, X. Yuan, G. Zeng, J. Zhou, X. Wang and J. W. Chew, *Adv. Mater.*, 2018, **30**, e1704561.

120 C. Hu, F. Shen, D. Zhu, H. Zhang, J. Xue and X. Han, *Front. Energy Res.*, 2017, **4**, 41.

121 Z. Ling, C. E. Ren, M. Q. Zhao, J. Yang, J. M. Giammarco, J. Qiu, M. W. Barsoum and Y. Gogotsi, *Proc. Natl. Acad. Sci. U. S. A.*, 2014, **111**, 16676–16681.

122 V. N. Borysiuk, V. N. Mochalin and Y. Gogotsi, *Nanotechnology*, 2015, **26**, 265705.

123 W. Xu, Z. Xu, Y. Liang, L. Liu and W. Weng, *Nanotechnology*, 2021, 32.

124 K. Wang, Y. Zhou, W. Xu, D. Huang, Z. Wang and M. Hong, *Ceram. Int.*, 2016, **42**, 8419–8424.

125 Z. Li, L. Wang, D. Sun, Y. Zhang, B. Liu, Q. Hu and A. Zhou, *Mater. Sci. Eng. B*, 2015, **191**, 33–40.

126 X.-H. Zha, J. Yin, Y. Zhou, Q. Huang, K. Luo, J. Lang, J. S. Francisco, J. He and S. Du, *J. Phys. Chem. C*, 2016, **120**, 15082–15088.

127 F. Kong, X. He, Q. Liu, X. Qi, Y. Zheng, R. Wang and Y. Bai, *Electrochim. Acta*, 2018, **265**, 140–150.

128 J. Yan, C. E. Ren, K. Maleski, C. B. Hatter, B. Anasori, P. Urbankowski, A. Sarycheva and Y. Gogotsi, *Adv. Funct. Mater.*, 2017, **27**, 1701264.

129 X. Liang, A. Garsuch and L. F. Nazar, *Angew. Chem.*, 2015, **127**, 3979–3983.

130 H. Wang, J. Li, K. Li, Y. Lin, J. Chen, L. Gao, V. Nicolosi, X. Xiao and J. M. Lee, *Chem. Soc. Rev.*, 2021, **50**, 1354–1390.

131 C. Liu, F. Li, L. P. Ma and H. M. Cheng, *Adv. Mater.*, 2010, **22**, E28–E62.

132 X. Zhang, L. Hou, A. Ciesielski and P. Samorì, *Adv. Energy Mater.*, 2016, **6**, 1600671.

133 Y. Yang, X. Liu, Z. Zhu, Y. Zhong, Y. Bando, D. Golberg, J. Yao and X. Wang, *Joule*, 2018, **2**, 1075–1094.

134 X. Zheng, P. Li, S. Dou, W. Sun, H. Pan, D. Wang and Y. Li, *Energy Environ. Sci.*, 2021, **14**, 2809–2858.

135 S. Zhang and N. Pan, *Adv. Energy Mater.*, 2015, **5**, 1401401.

136 A. G. Pandolfo and A. F. Hollenkamp, *J. Power Sources*, 2006, **157**, 11–27.

137 A. González, E. Goikolea, J. A. Barrena and R. Mysyk, *Renew. Sustain. Energy Rev.*, 2016, **58**, 1189–1206.

138 S. Xu, G. Wei, J. Li, Y. Ji, N. Klyui, V. Izotov and W. Han, *Chem. Eng. J.*, 2017, **317**, 1026–1036.

139 M. R. Lukatskaya, O. Mashtalir, C. E. Ren, Y. Dall'Agnese, P. Rozier, P. L. Taberna, M. Naguib, P. Simon, M. W. Barsoum and Y. Gogotsi, *Science*, 2013, **341**, 1502–1505.

140 J. Li, X. Yuan, C. Lin, Y. Yang, L. Xu, X. Du, J. Xie, J. Lin and J. Sun, *Adv. Energy Mater.*, 2017, **7**, 1602725.

141 Q. Yang, Z. Xu, B. Fang, T. Huang, S. Cai, H. Chen, Y. Liu, K. Gopalsamy, W. Gao and C. Gao, *J. Mater. Chem. A*, 2017, **5**, 22113–22119.

142 A. VahidMohammadi, M. Mojtabavi, N. M. Caffrey, M. Wanunu and M. Beidaghi, *Adv. Mater.*, 2019, **31**, 1806931.

143 Y. Zhu, K. Rajouâ, S. Le Vot, O. Fontaine, P. Simon and F. Favier, *Nano Energy*, 2020, **73**, 104734.

144 L. Wang, D. Shao, J. Guo, S. Zhang and Y. Lu, *Energy Technol.*, 2020, **8**, 1901003.

145 S. Zhao, C. Chen, X. Zhao, X. Chu, F. Du, G. Chen, Y. Gogotsi, Y. Gao and Y. Dall'Agnese, *Adv. Funct. Mater.*, 2020, 2000815.

146 Z. Fan, Y. Wang, Z. Xie, D. Wang, Y. Yuan, H. Kang, B. Su, Z. Cheng and Y. Liu, *Adv. Sci.*, 2018, **5**, 1800750.

147 H. Li, R. Chen, M. Ali, H. Lee and M. J. Ko, *Adv. Funct. Mater.*, 2020, 2002739.

148 Y. Zhou, K. Maleski, B. Anasori, J. O. Thostenson, Y. Pang, Y. Feng, K. Zeng, C. B. Parker, S. Zauscher and Y. Gogotsi, *ACS Nano*, 2020, **14**, 3576–3586.

149 L. Yu, L. Hu, B. Anasori, Y.-T. Liu, Q. Zhu, P. Zhang, Y. Gogotsi and B. Xu, *ACS Energy Lett.*, 2018, **3**, 1597–1603.

150 M. Carey and M. W. Barsoum, *Mater. Today Adv.*, 2021, **9**, 100120.

151 J. Fu, J. Yun, S. Wu, L. Li, L. Yu and K. H. Kim, *ACS Appl. Mater. Interfaces*, 2018, **10**, 34212–34221.

1144 | *J. Mater. Chem. A*, 2022, **10**, 1105–1149

This journal is © The Royal Society of Chemistry 2022

152 W. Yang, B. Huang, L. Li, K. Zhang, Y. Li, J. Huang, X. Tang, T. Hu, K. Yuan and Y. Chen, *Small Methods*, 2020, 2000434.

153 T. A. Le, N. Q. Tran, Y. Hong and H. Lee, *Chem. - Eur. J.*, 2019, **25**, 1037–1043.

154 M. Zhu, Y. Huang, Q. Deng, J. Zhou, Z. Pei, Q. Xue, Y. Huang, Z. Wang, H. Li and Q. Huang, *Adv. Energy Mater.*, 2016, **6**, 1600969.

155 C. Lu, A. Li, T. Zhai, C. Niu, H. Duan, L. Guo and W. Zhou, *Energy Storage Mater.*, 2020, **26**, 472–482.

156 K. Li, X. Wang, S. Li, P. Urbankowski, J. Li, Y. Xu and Y. Gogotsi, *Small*, 2020, **16**, 1906851.

157 R. B. Rakhi, B. Ahmed, D. Anjum and H. N. Alshareef, *ACS Appl. Mater. Interfaces*, 2016, **8**, 18806–18814.

158 S. B. Ambade, R. B. Ambade, W. Eom, S. H. Noh, S. H. Kim and T. H. Han, *Adv. Mater. Interfaces*, 2018, **5**, 1801361.

159 Z. Zhao and X. Wu, *Adv. Mater. Interfaces*, 2020, **7**, 2000831.

160 Y. Ma, H. Sheng, W. Dou, Q. Su, J. Zhou, E. Xie and W. Lan, *ACS Appl. Mater. Interfaces*, 2020, **12**, 41410–41418.

161 D. Zhang, J. Cao, X. Zhang, N. Insin, R. Liu and J. Qin, *ACS Appl. Energy Mater.*, 2020, **3**, 5949–5964.

162 I. Ayman, A. Rasheed, S. Ajmal, A. Rehman, A. Ali, I. Shakir and M. F. Warsi, *Energy Fuels*, 2020, **34**, 7622–7630.

163 R. Zhao, M. Wang, D. Zhao, H. Li, C. Wang and L. Yin, *ACS Energy Lett.*, 2017, **3**, 132–140.

164 Z. Pan and X. Ji, *J. Power Sources*, 2019, **439**, 227068.

165 C. Lu, L. Yang, B. Yan, L. Sun, P. Zhang, W. Zhang and Z. Sun, *Adv. Funct. Mater.*, 2020, **30**, 2000852.

166 S. Li, Q. Shi, Y. Li, J. Yang, T. H. Chang, J. Jiang and P. Y. Chen, *Adv. Funct. Mater.*, 2020, 2003721.

167 L. Sun, G. Song, Y. Sun, Q. Fu and C. Pan, *ACS Appl. Mater. Interfaces*, 2020, **12**, 44777–44788.

168 L. Li, N. Zhang, M. Zhang, L. Wu, X. Zhang and Z. Zhang, *ACS Sustain. Chem. Eng.*, 2018, **6**, 7442–7450.

169 Y. Tian, C. Yang, Y. Luo, H. Zhao, Y. Du, L. B. Kong and W. Que, *ACS Appl. Energy Mater.*, 2020, **3**, 5006–5014.

170 Q. X. Xia, N. M. Shinde, T. Zhang, J. M. Yun, A. Zhou, R. S. Mane, S. Mathur and K. H. Kim, *Dalton Trans.*, 2018, **47**, 8676–8682.

171 D. Wei, W. Wu, J. Zhu, C. Wang, C. Zhao and L. Wang, *J. Electroanal. Chem.*, 2020, **877**, 114538.

172 R. Ramachandran, Q. Hu, K. Rajavel, P. Zhu, C. Zhao, F. Wang and Z.-X. Xu, *J. Power Sources*, 2020, **471**, 228472.

173 X. Wang, H. Li, H. Li, S. Lin, W. Ding, X. Zhu, Z. Sheng, H. Wang, X. Zhu and Y. Sun, *Adv. Funct. Mater.*, 2020, **30**, 0190302.

174 A. M. Patil, N. R. Chodankar, E. Jung, S. Roy, D. P. Dubal, G. Guan, Y.-K. Han and S. C. Jun, *J. Mater. Chem. A*, 2021, **9**, 26135–26148.

175 A. M. Patil, J. Wang, S. Li, X. Hao, X. Du, Z. Wang, X. Hao, A. Abudula and G. Guan, *Chem. Eng. J.*, 2021, **421**, 127883.

176 K. Li, X. Wang, X. Wang, M. Liang, V. Nicolosi, Y. Xu and Y. Gogotsi, *Nano Energy*, 2020, **75**, 104971.

177 Q. Jiang, N. Kurra, M. Alhabeb, Y. Gogotsi and H. N. Alshareef, *Adv. Energy Mater.*, 2018, **8**, 1703043.

178 M. Hu, C. Cui, C. Shi, Z.-S. Wu, J. Yang, R. Cheng, T. Guang, H. Wang, H. Lu and X. Wang, *ACS Nano*, 2019, **13**, 6899–6905.

179 M. Boota and Y. Gogotsi, *Adv. Energy Mater.*, 2019, **9**, 1802917.

180 H. Liu, R. Hu, J. Qi, Y. Sui, Y. He, Q. Meng, F. Wei, Y. Ren, Y. Zhao and W. Wei, *Adv. Mater. Interfaces*, 2020, **7**, 1901659.

181 R. Liu, A. Zhang, J. Tang, J. Tian, W. Huang, J. Cai, C. Barrow, W. Yang and J. Liu, *Chem. - Eur. J.*, 2019, **25**, 5547–5554.

182 F. Li, Y.-L. Liu, G.-G. Wang, H.-Y. Zhang, B. Zhang, G.-Z. Li, Z.-P. Wu, L.-Y. Dang and J.-C. Han, *J. Mater. Chem. A*, 2019, **7**, 22631–22641.

183 P. Yu, G. Cao, S. Yi, X. Zhang, C. Li, X. Sun, K. Wang and Y. Ma, *Nanoscale*, 2018, **10**, 5906–5913.

184 X. Wang, S. Kajiyama, H. Iinuma, E. Hosono, S. Oro, I. Moriguchi, M. Okubo and A. Yamada, *Nat. Commun.*, 2015, **6**, 1–6.

185 J. Shi, S. Wang, Q. Wang, X. Chen, X. Du, M. Wang, Y. Zhao, C. Dong, L. Ruan and W. Zeng, *J. Power Sources*, 2020, **446**, 227345.

186 Q. Wang, S. Wang, X. Guo, L. Ruan, N. Wei, Y. Ma, J. Li, M. Wang, W. Li and W. Zeng, *Adv. Electron. Mater.*, 2019, **5**, 1900537.

187 C. Couly, M. Alhabeb, K. L. Van Aken, N. Kurra, L. Gomes, A. M. Navarro-Suárez, B. Anasori, H. N. Alshareef and Y. Gogotsi, *Adv. Electron. Mater.*, 2018, **4**, 1700339.

188 Y. Yue, N. Liu, Y. Ma, S. Wang, W. Liu, C. Luo, H. Zhang, F. Cheng, J. Rao and X. Hu, *ACS Nano*, 2018, **12**, 4224–4232.

189 L. Qin, Q. Tao, X. Liu, M. Fahlman, J. Halim, P. O. Persson, J. Rosen and F. Zhang, *Nano Energy*, 2019, **60**, 734–742.

190 C. J. Zhang, L. McKeon, M. P. Kremer, S.-H. Park, O. Ronan, A. Seral-Ascaso, S. Barwich, C. Ó. Coileáin, N. McEvoy and H. C. Nerl, *Nat. Commun.*, 2019, **10**, 1–9.

191 N. Wang, J. Liu, Y. Zhao, M. Hu, R. Qin and G. Shan, *ChemNanoMat*, 2019, **5**, 658–665.

192 C. Zhang, M. P. Kremer, A. Seral-Ascaso, S. H. Park, N. McEvoy, B. Anasori, Y. Gogotsi and V. Nicolosi, *Adv. Funct. Mater.*, 2018, **28**, 1705506.

193 N. Kurra, B. Ahmed, Y. Gogotsi and H. N. Alshareef, *Adv. Energy Mater.*, 2016, **6**, 1601372.

194 X. Huang and P. Wu, *Adv. Funct. Mater.*, 2020, **30**, 1910048.

195 H. Huang, H. Su, H. Zhang, L. Xu, X. Chu, C. Hu, H. Liu, N. Chen, F. Liu and W. Deng, *Adv. Electron. Mater.*, 2018, **4**, 1800179.

196 C. Zhang, B. Anasori, A. Seral-Ascaso, S. H. Park, N. McEvoy, A. Shmeliov, G. S. Duesberg, J. N. Coleman, Y. Gogotsi and V. Nicolosi, *Adv. Mater.*, 2017, **29**, 1702678.

197 M. Hu, Z. Li, G. Li, T. Hu, C. Zhang and X. Wang, *Adv. Mater. Technol.*, 2017, **2**, 1700143.

198 S. Uzun, S. Seyedin, A. L. Stoltzfus, A. S. Levitt, M. Alhabeb, M. Anayee, C. J. Strobel, J. M. Razal, G. Dion and Y. Gogotsi, *Adv. Funct. Mater.*, 2019, **29**, 1905015.

199 S. Seyedin, E. R. S. Yanza and J. M. Razal, *J. Mater. Chem. A*, 2017, **5**, 24076–24082.

200 J. Zhang, S. Seyedin, Z. Gu, W. Yang, X. Wang and J. M. Razal, *Nanoscale*, 2017, **9**, 18604–18608.

This journal is © The Royal Society of Chemistry 2022

J. Mater. Chem. A, 2022, **10**, 1105–1149 | 1145

201 Z. Wang, S. Qin, S. Seyedin, J. Zhang, J. Wang, A. Levitt, N. Li, C. Haines, R. Ovalle-Robles and W. Lei, *Small*, 2018, **14**, 1802225.

202 J. V. Vaghasiya, C. C. Mayorga-Martinez, J. Vyskočil, Z. Sofer and M. Pumera, *Adv. Funct. Mater.*, 2020, **30**, 2003673.

203 J. Tang, T. Mathis, X. Zhong, X. Xiao, H. Wang, M. Anayee, F. Pan, B. Xu and Y. Gogotsi, *Adv. Energy Mater.*, 2021, **11**, 2003025.

204 A. M. Patil, N. Kitiphatpiboon, X. An, X. Hao, S. Li, X. Hao, A. Abudula and G. Guan, *ACS Appl. Mater. Interfaces*, 2020, **12**, 52749–52762.

205 A. Rafieerad, A. Amiri, G. L. Sequiera, W. Yan, Y. Chen, A. A. Polycarpou and S. Dhingra, *Adv. Funct. Mater.*, 2021, 2100015.

206 J. Zhang, D. Jiang, L. Liao, L. Cui, R. Zheng and J. Liu, *Chem. Eng. J.*, 2021, 132232.

207 L. Ma, T. Zhao, F. Xu, T. You and X. Zhang, *Chem. Eng. J.*, 2021, **405**, 126694.

208 Q. Shan, X. Mu, M. Alhabeb, C. E. Shuck, D. Pang, X. Zhao, X.-F. Chu, Y. Wei, F. Du and G. Chen, *Electrochem. Commun.*, 2018, **96**, 103–107.

209 T. Chen, M. Li, S. Song, P. Kim and J. Bae, *Nano Energy*, 2020, **71**, 104549.

210 X. Wang, D. Zhang, H. Zhang, L. Gong, Y. Yang, W. Zhao, S. Yu, Y. Yin and D. Sun, *Nano Energy*, 2021, 106242.

211 J. Halim, S. Kota, M. R. Lukatskaya, M. Naguib, M. Q. Zhao, E. J. Moon, J. Pitock, J. Nanda, S. J. May and Y. Gogotsi, *Adv. Funct. Mater.*, 2016, **26**, 3118–3127.

212 S. De, C. K. Maity, S. Sahoo and G. C. Nayak, *ACS Appl. Energy Mater.*, 2021, **4**, 3712–3723.

213 W. Hou, Y. Sun, Y. Zhang, T. Wang, L. Wu, Y. Du and W. Zhong, *J. Alloys Compd.*, 2021, **859**, 157797.

214 Z. Liu, H. Xiong, Y. Luo, L. Zhang, K. Hu, L. Zhang, Y. Gao and Z.-A. Qiao, *ChemSusChem*, 2021, **14**, 4422–4430.

215 W. Liang and I. Zhitomirsky, *J. Mater. Chem. A*, 2021, **9**, 10335–10344.

216 X. Li, J. Zhu, W. Liang and I. Zhitomirsky, *Mater. Chem. Phys.*, 2021, 124748.

217 W. Zheng, J. Halim, A. S. Etman, A. El Ghazaly, J. Rosen and M. W. Barsoum, *Electrochim. Acta*, 2021, **370**, 137665.

218 G. Ma, Z. Wang, B. Gao, T. Ding, Q. Zhong, X. Peng, J. Su, B. Hu, L. Yuan and P. K. Chu, *J. Mater. Chem. A*, 2015, **3**, 14617–14624.

219 Y.-Z. Cai, Y.-S. Fang, W.-Q. Cao, P. He and M.-S. Cao, *J. Alloys Compd.*, 2021, **868**, 159159.

220 B. Ranjan, G. K. Sharma, G. Malik, A. Kumar and D. Kaur, *Nanotechnology*, 2021, **32**, 455402.

221 F. Qiao, W. Liu, S. Wang, F. Lin, Y. Chen, M. Yuan, Z. Weng, S. Wang, J. Zheng and Y. Zhao, *J. Alloys Compd.*, 2021, **870**, 159393.

222 X. Yang, J. Mao, H. Niu, Q. Wang, K. Zhu, K. Ye, G. Wang, D. Cao and J. Yan, *Chem. Eng. J.*, 2021, **406**, 126713.

223 P. A. Shinde, N. R. Chodankar, M. A. Abdelkareem, Y.-K. Han and A. G. Olabi, *Chem. Eng. J.*, 2021, 131888.

224 B. Pandit, S. S. Karade and B. R. Sankapal, *ACS Appl. Mater. Interfaces*, 2017, **9**, 44880–44891.

225 V. Shrivastav, S. Sundriyal, V. Shrivastav, U. K. Tiwari and A. Deep, *Energy Fuels*, 2021.

226 P. A. Shinde, S. Park, N. R. Chodankar, S. Park, Y.-K. Han, A. G. Olabi and S. C. Jun, *Applied Materials Today*, 2021, **22**, 100951.

227 D. Choi, G. E. Blomgren and P. N. Kumta, *Adv. Mater.*, 2006, **18**, 1178–1182.

228 H. Cui, G. Zhu, X. Liu, F. Liu, Y. Xie, C. Yang, T. Lin, H. Gu and F. Huang, *Adv. Sci.*, 2015, **2**, 1500126.

229 X. Zhou, C. Shang, L. Gu, S. Dong, X. Chen, P. Han, L. Li, J. Yao, Z. Liu and H. Xu, *ACS Appl. Mater. Interfaces*, 2011, **3**, 3058–3063.

230 R. Prakash, A. Kumar, A. Pandey and D. Kaur, *Int. J. Hydrogen Energy*, 2019, **44**, 10823–10832.

231 K. Li, B. Zhao, H. Zhang, H. Lv, J. Bai, H. Ma, P. Wang, W. Li, J. Si and X. Zhu, *Adv. Funct. Mater.*, 2021, 2103073.

232 I. Demiroglu, F. o. M. Peeters, O. u. Gülseren, D. Çakır and C. Sevik, *J. Phys. Chem. Lett.*, 2019, **10**, 727–734.

233 P. Lian, Y. Dong, Z.-S. Wu, S. Zheng, X. Wang, S. Wang, C. Sun, J. Qin, X. Shi and X. Bao, *Nano Energy*, 2017, **40**, 1–8.

234 H. Kim, J. Hong, Y. U. Park, J. Kim, I. Hwang and K. Kang, *Adv. Funct. Mater.*, 2015, **25**, 534–541.

235 M. Naguib, R. A. Adams, Y. Zhao, D. Zemlyanov, A. Varma, J. Nanda and V. G. Pol, *Chem. Commun.*, 2017, **53**, 6883–6886.

236 Y. Tian, Y. An and J. Feng, *ACS Appl. Mater. Interfaces*, 2019, **11**, 10004–10011.

237 J. Pang, R. G. Mendes, A. Bachmatiuk, L. Zhao, H. Q. Ta, T. Gemming, H. Liu, Z. Liu and M. H. Rummeli, *Chem. Soc. Rev.*, 2019, **48**, 72–133.

238 M. Naguib, J. Come, B. Dyatkin, V. Presser, P.-L. Taberna, P. Simon, M. W. Barsoum and Y. Gogotsi, *Electrochem. Commun.*, 2012, **16**, 61–64.

239 Y. D. A. Yu Xie, M. Naguib, Y. Gogotsi, M. W. Barsoum, H. L. Zhuang and P. R. C. Kent, *ACS Nano*, 2014, **8**, 9606–9615.

240 Y. Xie, M. Naguib, V. N. Mochalin, M. W. Barsoum, Y. Gogotsi, X. Yu, K. W. Nam, X. Q. Yang, A. I. Kolesnikov and P. R. Kent, *J. Am. Chem. Soc.*, 2014, **136**, 6385–6394.

241 X. Liang, A. Garsuch and L. F. Nazar, *Angew. Chem., Int. Ed. Engl.*, 2015, **54**, 3907–3911.

242 X. Xie, M. Q. Zhao, B. Anasori, K. Maleski, C. E. Ren, J. Li, B. W. Byles, E. Pomerantseva, G. Wang and Y. Gogotsi, *Nano Energy*, 2016, **26**, 513–523.

243 M. Q. Zhao, X. Xie, C. E. Ren, T. Makaryan, B. Anasori, G. Wang and Y. Gogotsi, *Adv. Mater.*, 2017, **29**, 1702410.

244 X. Liang, Y. Rangom, C. Y. Kwok, Q. Pang and L. F. Nazar, *Adv. Mater.*, 2017, **29**, 1603040.

245 Y. Dong, Z. S. Wu, S. Zheng, X. Wang, J. Qin, S. Wang, X. Shi and X. Bao, *ACS Nano*, 2017, **11**, 4792–4800.

246 W. Bao, L. Liu, C. Wang, S. Choi, D. Wang and G. Wang, *Adv. Energy Mater.*, 2018, **8**, 1702485.

247 Y. Zhang, Z. Mu, C. Yang, Z. Xu, S. Zhang, X. Zhang, Y. Li, J. Lai, Z. Sun, Y. Yang, Y. Chao, C. Li, X. Ge, W. Yang and S. Guo, *Adv. Funct. Mater.*, 2018, **28**, 1707578.

1146 | *J. Mater. Chem. A*, 2022, **10**, 1105–1149

This journal is © The Royal Society of Chemistry 2022

248 Y. T. Liu, P. Zhang, N. Sun, B. Anasori, Q. Z. Zhu, H. Liu, Y. Gogotsi and B. Xu, *Adv. Mater.*, 2018, **30**, e1707334.

249 C. Zeng, F. Xie, X. Yang, M. Jaroniec, L. Zhang and S. Z. Qiao, *Angew. Chem., Int. Ed. Engl.*, 2018, **57**, 8540–8544.

250 X. Wang, C. Yang, X. Xiong, G. Chen, M. Huang, J.-H. Wang, Y. Liu, M. Liu and K. Huang, *Energy Storage Mater.*, 2019, **16**, 344–353.

251 L. Jiao, C. Zhang, C. Geng, S. Wu, H. Li, W. Lv, Y. Tao, Z. Chen, G. Zhou, J. Li, G. Ling, Y. Wan and Q. H. Yang, *Adv. Energy Mater.*, 2019, **9**, 1900219.

252 H. Huang, J. Cui, G. Liu, R. Bi and L. Zhang, *ACS Nano*, 2019, **13**, 3448–3456.

253 C. J. Zhang, S. H. Park, A. Seral-Ascaso, S. Barwich, N. McEvoy, C. S. Boland, J. N. Coleman, Y. Gogotsi and V. Nicolosi, *Nat. Commun.*, 2019, **10**, 849.

254 X. Wang, T. S. Mathis, K. Li, Z. Lin, L. Vlcek, T. Torita, N. C. Osti, C. Hatter, P. Urbankowski, A. Sarycheva, M. Tyagi, E. Mamontov, P. Simon and Y. Gogotsi, *Nat. Energy*, 2019, **4**, 241–248.

255 Y. Zhang, Z. Mu, J. Lai, Y. Chao, Y. Yang, P. Zhou, Y. Li, W. Yang, Z. Xia and S. Guo, *ACS Nano*, 2019, **13**, 2167–2175.

256 X. Li, M. Li, Q. Yang, H. Li, H. Xu, Z. Chai, K. Chen, Z. Liu, Z. Tang, L. Ma, Z. Huang, B. Dong, X. Yin, Q. Huang and C. Zhi, *ACS Nano*, 2020, **14**, 541–551.

257 F. Zhang, Z. Jia, C. Wang, A. Feng, K. Wang, T. Hou, J. Liu, Y. Zhang and G. Wu, *Energy*, 2020, **195**, 117047.

258 R. Zhao, H. Di, X. Hui, D. Zhao, R. Wang, C. Wang and L. Yin, *Energy Environ. Sci.*, 2020, **13**, 246–257.

259 N. Li, Y. Xie, S. Peng, X. Xiong and K. Han, *J. Energy Chem.*, 2020, **42**, 116–125.

260 M. K. Aslam and M. Xu, *Nanoscale*, 2020, **12**, 15993–16007.

261 B.-M. Jun, S. Kim, J. Heo, C. M. Park, N. Her, M. Jang, Y. Huang, J. Han and Y. Yoon, *Nano Res.*, 2019, **12**, 471–487.

262 X. Zhang, Z. Zhang and Z. Zhou, *J. Energy Chem.*, 2018, **27**, 73–85.

263 D. Xiong, X. Li, Z. Bai and S. Lu, *Small*, 2018, **14**, 1703419.

264 Y. Xiao, J.-Y. Hwang and Y.-K. Sun, *J. Mater. Chem. A*, 2016, **4**, 10379–10393.

265 X. Dong, Y. Zhang, B. Ding, X. Hao, H. Dou and X. Zhang, *J. Power Sources*, 2018, **390**, 208–214.

266 T. Jin, Q. Han, Y. Wang and L. Jiao, *Small*, 2018, **14**, 1703086.

267 J. Luo, X. Tao, J. Zhang, Y. Xia, H. Huang, L. Zhang, Y. Gan, C. Liang and W. Zhang, *ACS Nano*, 2016, **10**, 2491–2499.

268 B. Ahmed, D. H. Anjum, M. N. Hedhili, Y. Gogotsi and H. N. Alshareef, *Nanoscale*, 2016, **8**, 7580–7587.

269 P. Zhang, R. A. Soomro, Z. Guan, N. Sun and B. Xu, *Energy Storage Mater.*, 2020, **29**, 163–171.

270 J. Zhu, R. Shi, Y. Liu, Y. Zhu, J. Zhang, X. Hu and L. Li, *Appl. Surf. Sci.*, 2020, **528**, 146985.

271 K. Shen, B. Li and S. Yang, *Energy Storage Mater.*, 2020, **24**, 670–675.

272 N. N. N. Ab Alim, M. S. M. Saheed, N. M. Mohamed and M. S. M. Saheed, *Mater. Today Proc.*, 2019, **7**, 738–743.

273 J. Song, X. Guo, J. Zhang, Y. Chen, C. Zhang, L. Luo, F. Wang and G. Wang, *J. Mater. Chem. A*, 2019, **7**, 6507–6513.

274 Q. Zhao, Q. Zhu, J. Miao, P. Zhang, P. Wan, L. He and B. Xu, *Small*, 2019, **15**, 1904293.

275 D. Adekoya, S. Qian, X. Gu, W. Wen, D. Li, J. Ma and S. Zhang, *Nano-Micro Lett.*, 2021, **13**, 13.

276 M. Naguib, J. Halim, J. Lu, K. M. Cook, L. Hultman, Y. Gogotsi and M. W. Barsoum, *J. Am. Chem. Soc.*, 2013, **135**, 15966–15969.

277 R. Fang, S. Zhao, Z. Sun, D. W. Wang, H. M. Cheng and F. Li, *Adv. Mater.*, 2017, **29**.

278 J. Huang, R. Meng, L. Zu, Z. Wang, N. Feng, Z. Yang, Y. Yu and J. Yang, *Nano Energy*, 2018, **46**, 20–28.

279 M. Shang, X. Chen, B. Li and J. Niu, *ACS Nano*, 2020, **14**, 3678–3686.

280 S. Mukherjee, S. B. Mujib, D. Soares and G. Singh, *Mater*, 2019, **12**.

281 L. Huang, J. Cheng, X. Li and B. Wang, *J. Nanosci. Nanotechnol.*, 2015, **15**, 6295–6307.

282 K. B. Hueso, M. Armand and T. Rojo, *Energy Environ. Sci.*, 2013, **6**, 734–749.

283 Q. Wang, C. Zhao, Y. Lu, Y. Li, Y. Zheng, Y. Qi, X. Rong, L. Jiang, X. Qi, Y. Shao, D. Pan, B. Li, Y. S. Hu and L. Chen, *Small*, 2017, **13**, 1701835.

284 Q. Zhao, Y. Lu and J. Chen, *Adv. Energy Mater.*, 2017, **7**, 1601792.

285 J. L. Kaufman, J. Vinckevičiūtė, S. Krishna Kolli, J. Gabriel Goiri and A. Van Der Ven, *Philos. Trans. R. Soc., A*, 2019, **377**, 20190020.

286 Y. M. Chang, H. W. Lin, L. J. Li and H. Y. Chen, *Mater. Today Adv.*, 2020, **6**, 100054.

287 J. M. Lee, G. Singh, W. Cha, S. Kim, J. Yi, S. J. Hwang and A. Vinu, *ACS Energy Lett.*, 2020, **5**, 1939–1966.

288 M. M. Doeff, J. Cabana and M. Shirpour, *J. Inorg. Organomet. Polym. Mater.*, 2014, **24**, 5–14.

289 A. M. Skundin, T. L. Kulova and A. B. Yaroslavtsev, *Russ. J. Electrochem.*, 2018, **54**, 113–152.

290 Y. Wu and Y. Yu, *Energy Storage Mater.*, 2019, **16**, 323–343.

291 X. Xiang, Y. Lu and J. Chen, *Acta Chim. Sin.*, 2017, **75**, 154–162.

292 S. Yang, S. Li, W. Sun, W. Dong and D. Shen, *Gongneng Cailiao*, 2016, **47**, 08020–08030.

293 M. Chen, Q. Liu, S. W. Wang, E. Wang, X. Guo and S. L. Chou, *Adv. Energy Mater.*, 2019, **9**, 1803609.

294 S. M. Zheng, Y. R. Tian, Y. X. Liu, S. Wang, C. Q. Hu, B. Wang and K. M. Wang, *Rare Met.*, 2020, 272–289, DOI: 10.1007/s12598-020-01605-z.

295 B. Xiao, T. Rojo and X. Li, *ChemSusChem*, 2019, **12**, 133–144.

296 Y. Huang, Y. Zheng, X. Li, F. Adams, W. Luo, Y. Huang and L. Hu, *ACS Energy Lett.*, 2018, **3**, 1604–1612.

297 J. Y. Hwang, S. T. Myung and Y. K. Sun, *Chem. Soc. Rev.*, 2017, **46**, 3529–3614.

298 J. Song, B. Xiao, Y. Lin, K. Xu and X. Li, *Adv. Energy Mater.*, 2018, **8**, 1703082.

299 T. L. Kulova and A. M. Skundin, *Russ. Chem. Bull.*, 2017, **66**, 1329–1335.

300 H. Kim, H. Kim, Z. Ding, M. H. Lee, K. Lim, G. Yoon and K. Kang, *Adv. Energy Mater.*, 2016, **6**, 1600943.

This journal is © The Royal Society of Chemistry 2022

J. Mater. Chem. A, 2022, **10**, 1105–1149 | 1147

301 D. Han, J. Zhang, Z. Weng, D. Kong, Y. Tao, F. Ding, D. Ruan and Q. H. Yang, *Mater. Today Energy*, 2019, **11**, 30–45.

302 C. Nithya and S. Gopukumar, *Wiley Interdiscip. Rev.: Energy Environ.*, 2015, **4**, 253–278.

303 L. Wang, Z. Wei, M. Mao, H. Wang, Y. Li and J. Ma, *Energy Storage Mater.*, 2019, **16**, 434–454.

304 A. Ponrouch, D. Monti, A. Boschin, B. Steen, P. Johansson and M. R. Palacín, *J. Mater. Chem. A*, 2015, **3**, 22–42.

305 Y. Wu, P. Nie, L. Wu, H. Dou and X. Zhang, *Chem. Eng. J.*, 2018, **334**, 932–938.

306 F. Wu, Y. Jiang, Z. Ye, Y. Huang, Z. Wang, S. Li, Y. Mei, M. Xie, L. Li and R. Chen, *J. Mater. Chem. A*, 2019, **7**, 1315–1322.

307 S. Zhang and W. Q. Han, *Phys. Chem. Chem. Phys.*, 2020, **22**, 16482–16526.

308 J. Nan, X. Guo, J. Xiao, X. Li, W. Chen, W. Wu, H. Liu, Y. Wang, M. Wu and G. Wang, *Small*, 2019, 1902085, DOI: 10.1002/smll.201902085.

309 X. Shen, R. Hai, X. Wang, X. Li, Y. Wang, F. Yu and J. Ma, *J. Mater. Chem. A*, 2020, **8**, 19309–19318.

310 Q. Meng, J. Ma, Y. Zhang, Z. Li, C. Zhi, A. Hu and J. Fan, *Nanoscale*, 2018, **10**, 3385–3392.

311 H. Tang, W. Li, L. Pan, C. P. Cullen, Y. Liu, A. Pakdel, D. Long, J. Yang, N. McEvoy, G. S. Duesberg, V. Nicolosi and C. J. Zhang, *Adv. Sci.*, 2018, **5**, 1800502.

312 R. Zhao, Z. Qian, Z. Liu, D. Zhao, X. Hui, G. Jiang, C. Wang and L. Yin, *Nano Energy*, 2019, **65**, 104037.

313 X. Wang, Y. Cai, S. Wu and B. Li, *Appl. Surf. Sci.*, 2020, **525**, 146501.

314 T. Kobayashi, Y. Sun, K. Prenger, D. E. Jiang, M. Naguib and M. Pruski, *J. Phys. Chem. C*, 2020, **124**, 13649–13655.

315 X. Wang, J. Wang, J. Qin, X. Xie, R. Yang and M. Cao, *ACS Appl. Mater. Interfaces*, 2020, **12**, 39181–39194.

316 H. Dai, W. Xu, Y. Chen, M. Li, Z. Chen, B. Yang, S. Mei, W. Zhang, F. Xie, W. Wei, R. Guo and G. Zhang, *Colloids Surf., A*, 2020, **591**, 124561.

317 X. Meng, *J. Mater. Chem. A*, 2017, **5**, 10127–10149.

318 L. F. Que, F. D. Yu, L. Deng, D. M. Gu and Z. B. Wang, *Energy Storage Mater.*, 2020, **25**, 537–546.

319 G. R. Berdiyorov, *Appl. Surf. Sci.*, 2015, **359**, 153–157.

320 Q. Lin, J. Zhang, W. Lv, J. Ma, Y. He, F. Kang and Q. H. Yang, *Small*, 2020, **16**, 1902603.

321 D. Er, J. Li, M. Naguib, Y. Gogotsi and V. B. Shenoy, *ACS Appl. Mater. Interfaces*, 2014, **6**, 11173–11179.

322 Y.-X. Yu, *J. Phys. Chem. C*, 2016, **120**, 5288–5296.

323 J. Zhu, M. Wang, M. Lyu, Y. Jiao, A. Du, B. Luo, I. Gentle and L. Wang, *ACS Appl. Nano Mater.*, 2018, **1**, 6854–6863.

324 M. Tao, G. Du, T. Yang, W. Gao, L. Zhang, W. Du, J. Jiang, S. Bao and M. Xu, *J. Mater. Chem. A*, 2020, **8**, 3018–3026.

325 Y. Fang, R. Lian, H. Li, Y. Zhang, Z. Gong, K. Zhu, K. Ye, J. Yan, G. Wang, Y. Gao, Y. Wei and D. Cao, *ACS Nano*, 2020, **14**, 8744–8753.

326 S. Sun, C. Liao, A. M. Hafez, H. Zhu and S. Wu, *Chem. Eng. J.*, 2018, **338**, 27–45.

327 Q. Meng, A. Hu, C. Zhi and J. Fan, *Phys. Chem. Chem. Phys.*, 2017, **19**, 29106–29113.

328 N. Sun, Q. Zhu, B. Anasori, P. Zhang, H. Liu, Y. Gogotsi and B. Xu, *Adv. Funct. Mater.*, 2019, **29**, 1906282.

329 M. Wahid, D. Puthusseri, Y. Gawli, N. Sharma and S. Ogale, *ChemSusChem*, 2018, **11**, 506–526.

330 J. Tang, X. Huang, T. Lin, T. Qiu, H. Huang, X. Zhu, Q. Gu, B. Luo and L. Wang, *Energy Storage Mater.*, 2020, **26**, 550–559.

331 C. Wang, S. Wei, P. Zhang, K. Zhu, P. Song, S. Chen and L. Song, *Chin. Chem. Lett.*, 2020, **31**, 969–979.

332 C. Eames and M. S. Islam, *J. Am. Chem. Soc.*, 2014, **136**, 16270–16276.

333 J. Li, J. Zhang, B. Rui, L. Lin, L. Chang and P. Nie, *Prog. Chem.*, 2019, **31**, 1283–1292.

334 Y. Z. Fang, R. Hu, K. Zhu, K. Ye, J. Yan, G. Wang and D. Cao, *Adv. Funct. Mater.*, 2020, **30**, 2005663.

335 L. Zhang, L. Yin, R. Zhao, H. Di, C. Wang, X. Hui, D. Zhao and R. Wang, *ACS Nano*, 2020, **14**, 13938–13951.

336 M. Tao, G. Du, Y. Zhang, W. Gao, D. Liu, Y. Luo, J. Jiang, S. Bao and M. Xu, *Chem. Eng. J.*, 2019, **369**, 828–833.

337 J. Wen, Q. Fu, W. Wu, H. Gao, X. Zhang and B. Wang, *ACS Appl. Mater. Interfaces*, 2019, **11**, 7087–7095.

338 J. Li, B. Rui, W. Wei, P. Nie, L. Chang, Z. Le, M. Liu, H. Wang, L. Wang and X. Zhang, *J. Power Sources*, 2020, **449**, 227481.

339 X. Wu, H. Wang, Z. Zhao and B. Huang, *J. Mater. Chem. A*, 2020, **8**, 12705–12715.

340 Z. Xia, X. Chen, H. Ci, Z. Fan, Y. Yi, W. Yin, N. Wei, J. Cai, Y. Zhang and J. Sun, *J. Energy Chem.*, 2020, **53**, 155–162.

341 X. Tang, D. Zhou, P. Li, X. Guo, B. Sun, H. Liu, K. Yan, Y. Gogotsi and G. Wang, *Adv. Mater.*, 2020, **32**, 1906739.

342 Y. Tian, Y. An, S. Xiong, J. Feng and Y. Qian, *J. Mater. Chem. A*, 2019, **7**, 9716–9725.

343 J. Yang, M. Naguib, M. Ghidiu, L. M. Pan, J. Gu, J. Nanda, J. Halim, Y. Gogotsi, M. W. Barsoum and Y. Zhou, *J. Am. Ceram. Soc.*, 2015, **99**, 660–666.

344 J. Wang, X. Yue, Z. Xie, A. M. Patil, S. Peng, X. Hao, A. Abudula and G. Guan, *J. Alloys Compd.*, 2021, 874.

345 X. Yue, J. Wang, A. M. Patil, X. An, Z. Xie, X. Hao, Z. Jiang, A. Abudula and G. Guan, *Chem. Eng. J.*, 2021, 417.

346 X. Yue, J. Wang, Z. Xie, A. M. Patil, T. Yu, X. Du, Z. Wang, X. Hao, A. Abudula and G. Guan, *J. Mater. Sci.*, 2020, **55**, 14389–14400.

347 M. Tao, G. Du, T. Yang, W. Gao, L. Zhang, W. Du, J. Jiang, S. Bao and M. Xu, *J. Mater. Chem. A*, 2020, **8**, 3018–3026.

348 M. Lu, Y. Zhang, J. Chen, W. Han, W. Zhang, H. Li, X. Zhang and B. Zhang, *J. Energy Chem.*, 2020, **49**, 358–364.

349 J. Zhao, J. Wen, J. Xiao, X. Ma, J. Gao, L. Bai, H. Gao, X. Zhang and Z. Zhang, *J. Energy Chem.*, 2021, **53**, 387–395.

350 G. Mu, D. Mu, B. Wu, C. Ma, J. Bi, L. Zhang, H. Yang and F. Wu, *Small*, 2020, **16**, e1905430.

351 J. Li, B. Rui, W. Wei, P. Nie, L. Chang, Z. Le, M. Liu, H. Wang, L. Wang and X. Zhang, *J. Power Sources*, 2020, 449.

352 Q. Yang, W. Gao, W. Zhong, M. Tao, Y. Qi, S.-j. Bao and M. Xu, *New J. Chem.*, 2020, **44**, 3072–3077.

353 Y. Zhang, R. Zhan, Q. Xu, H. Liu, M. Tao, Y. Luo, S. Bao, C. Li and M. Xu, *Chem. Eng. J.*, 2019, **357**, 220–225.

354 S. Zuo, X. Xu, S. Ji, Z. Wang, Z. Liu and J. Liu, *Chem. - Eur. J.*, 2020, 830–860, DOI: 10.1002/chem.202002202.

355 C. Wang, S. Wei, S. Chen, D. Cao and L. Song, *Small Methods*, 2019, **3**, 1900495.

356 K. Zhu, T. Wu, S. Sun, Y. Wen and K. Huang, *ChemElectroChem*, 2020, **7**, 2714–2734.

357 X. Ji and H. Jiang, *Chem. Res. Chin. Univ.*, 2020, **36**, 55–60.

358 L. E. Blanc, D. Kundu and L. F. Nazar, *Joule*, 2020, **4**, 771–799.

359 D. Choi, S. Lim and D. Han, *J. Energy Chem.*, 2021, **53**, 396–406.

360 J. Liu, J. Hu, Q. Deng, J. Mo, H. Xie, Z. Liu, Y. Xiong, X. Wu and Y. Wu, *Isr. J. Chem.*, 2015, **55**, 521–536.

361 D. Pahari and S. Puravankara, *ACS Sustain. Chem. Eng.*, 2020, **8**, 10613–10625.

362 A. R. Mainar, O. Leonet, M. Bengoechea, I. Boyano, I. De Meatza, A. Kvasha, A. Guerfi and J. Alberto Blázquez, *Int. J. Energy Res.*, 2016, **40**, 1032–1049.

363 N. Ma, P. Wu, Y. Wu, D. Jiang and G. Lei, *Funct. Mater. Lett.*, 2019, **12**, 1930003.

364 X. Jia, C. Liu, Z. G. Neale, J. Yang and G. Cao, *Chem. Rev.*, 2020, **120**, 7795–7866.

365 R. Venkatkarthick, N. Rodthongkum, X. Zhang, S. Wang, P. Pattananuwat, Y. Zhao, R. Liu and J. Qin, *ACS Appl. Energy Mater.*, 2020, **3**, 4677–4689.

366 J. Shin, J. Lee, Y. Park and J. W. Choi, *Chem. Sci.*, 2020, **11**, 2028–2044.

367 Z. Fan, W. He, M. Ni, P. Zhang, W. Tian, W. Zhang, L. Pan and Z. Sun, *Energy Technol.*, 2020, 2000829, DOI: 10.1002/ente.202000829.

368 W. Ling, P. Wang, Z. Chen, H. Wang, J. Wang, Z. Ji, J. Fei, Z. Ma, N. He and Y. Huang, *ChemElectroChem*, 2020, **7**, 2957–2978.

369 L. Fan, Y. Ru, H. Xue, H. Pang and Q. Xu, *Adv. Sustainable Syst.*, 2020, **4**, 2000178.

370 S. Luo, L. Xie, F. Han, W. Wei, Y. Huang, H. Zhang, M. Zhu, O. G. Schmidt and L. Wang, *Adv. Funct. Mater.*, 2019, **29**, 1901336.

371 S. Wang, Q. Wang, W. Zeng, M. Wang, L. Ruan and Y. Ma, *Nano-Micro Lett.*, 2019, **11**, 70.

372 X. Li, M. Li, Q. Yang, D. Wang, L. Ma, G. Liang, Z. Huang, B. Dong, Q. Huang and C. Zhi, *Adv. Energy Mater.*, 2020, **10**, 2001394.

373 X. Mu, D. Wang, F. Du, G. Chen, C. Wang, Y. Wei, Y. Gogotsi, Y. Gao and Y. Dall'Agnese, *Adv. Funct. Mater.*, 2019, **29**, 1902953.

374 E. Kayali, A. VahidMohammadi, J. Orangi and M. Beidaghi, *ACS Appl. Mater. Interfaces*, 2018, **10**, 25949–25954.

375 R. Bian, G. He, W. Zhi, S. Xiang, T. Wang and D. Cai, *J. Mater. Chem. C*, 2019, **7**, 474–478.

This journal is © The Royal Society of Chemistry 2022

J. Mater. Chem. A, 2022, **10**, 1105–1149 | **1149**